Fall 11-14-2016

Electrochemical Fabrication of Energetic Thin Films

Jonathan J. Coleman
University of New Mexico - Main Campus

Jonathan Joseph Coleman
Candidate

Chemical and Biological Engineering
Department

This dissertation is approved, and it is acceptable in quality and form for publication:

Approved by the Dissertation Committee:

Plamen Atanassov , Chairperson

Dimiter Petsev

Chris Apblett

David R. Wheeler

Mehran Tehrani

ELECTROCHEMICAL FABRICATION OF ENERGETIC THIN FILMS

by

JONATHAN JOSEPH COLEMAN

B.S., Chemical Engineering, University of New Mexico, 2010

DISSERTATION

Submitted in Partial Fulfillment of the

Requirements for the Degree of

Doctor of Philosophy
Engineering

The University of New Mexico

Albuquerque, New Mexico

December, 2016

Acknowledgements

I would like to acknowledge and thank the immense number of people that have helped me get to where I am today. Notably my Advisor, Dr. Chris Apblett, for teaching me a great deal and for his support on this project, I would be nowhere without him. Dr. Petsev for his encouragement even as an undergraduate. Dr. Atanassov for consistently helping when I needed something fixed (which was often). Dr. David Wheeler for moral and chemistry support. Adam Rowen for believing in me and bringing me into this field, I would not have been the same person without him (so blame him). For all of the help with specific focuses in this project, Dr. Alam with NMR and Gaussian, Dr. Tappan and Dr. Knepper for calorimetry, Dr. Kotula for his work with the TEM and Bonnie McKenzie for her work with on the SEM. Along with everyone else on my team and that I've meet along the way, just to name a few: Christian, Jamin, Brian, Hannah, Arthur, Serena, Chelsea, Kelsey, Chris, Josey, Jaclyn, Kyle, Mani, Harry, Travis, Ed, Drew, Sarah, Sara, Dennis, Graham, Eric and my family.

ELECTROCHEMICAL FABRICATION OF ENERGETIC THIN FILMS

By

Jonathan Coleman

B.S. Chemical Engineering, University of New Mexico

Albuquerque, New Mexico 2010

Ph.D., Engineering, University of New Mexico, 2016

Abstract

Energetic thin films have use in many technologies and are currently fabricated as either pressed pellets that suffer from low packing density, or expensive physical vapor deposition techniques. The stringent material and structuring requirements that make these films effective limit the fabrication and material choices. My aim was to investigate the design of a new fabrication process, using some of the current best commercially available films as a design guide while reducing the process cost. These films are nanostructured aluminum and nickel compounds.

Electrochemical codeposition allows for fabrication of a multi-phase film at low temperatures with high control over the structuring and composition. Because of the ratio of the components that are desired in the film, it is necessary that the matrix phase be aluminum and the particle phase be nickel, where the free floating particles are incorporated into the growing electrodeposited matrix metal. The particles become incorporated based on the number of particles in solution as well as fluid flow in the

reactor and the electrodeposited matrix growth rate. The growth of the matrix is crucial to the process of particle incorporation and must be well understood.

The diffusion rate of the electroactive species and the kinetics of the reduction process are important parameters in an electrocodeposition process. The matrix growth rate must be high enough to incorporate particles, and the flux of the electroactive species to the electrode, a combination of diffusion and convection, must be higher than the rate of consumption. It was found that the diffusion rates of the reducible species can be modified heavily with the addition of dilution agents in the electrolyte. The optimal conditions for dilution correlate to the maximum conductivity of the solution, which exhibits a maximum based on the increasing diffusion rates and decreasing ionic concentration with added dilution, and different dilutions have varied effects. The diffusion also shifts with changing ionic liquid composition, which modifies the open volume of the electrolyte and improves hole mobility. There is a two to four-fold increase in diffusion rates between static and dynamic conditions, and this is thought to be attributed to decreasing electrostatic attractions between the ions, evidenced by the shear thinning properties of the ionic liquid electrolyte.

The kinetics can be modified with both temperature and the overpotential applied and does not change with composition. Increasing temperature also increases the diffusion rates, although to a lesser extent than the kinetics. Control of the diffusion and kinetics of the matrix growth will lead to optimization of particle incorporation.

The codeposition of particles is a complex process and empirical tests as well as theoretical modeling are used to determine improved conditions to reach the desired composition and dispersion. At high agitation the particles experience too much shear

force, leading to too low of residence time on the electrode and no incorporation. Too low of flow leads to a buildup of particles on the electrode surface and a spongy porous film. Initial tests of codeposited films show ~12-20% nickel incorporation, shy of the 30-40% target and ~5 nanometer interfacial mixing properties, matching that of the commercially available films.

Table of Contents

Chapter 1: Introduction

1.1 Thermal Batteries and Heat Sources

Thermal batteries are composed of inorganic salt electrolytes that are solid at room temperature and use elevated temperatures to operate. Prior to activation, the solid electrolytes are relatively nonconductive and inert, leading to very long shelf lives with negligible self-discharge. Thermal batteries can be used up to 25 years after production with very high reliability and negligible degradation [1]. The components of a thermal battery are shown in Figure 1.

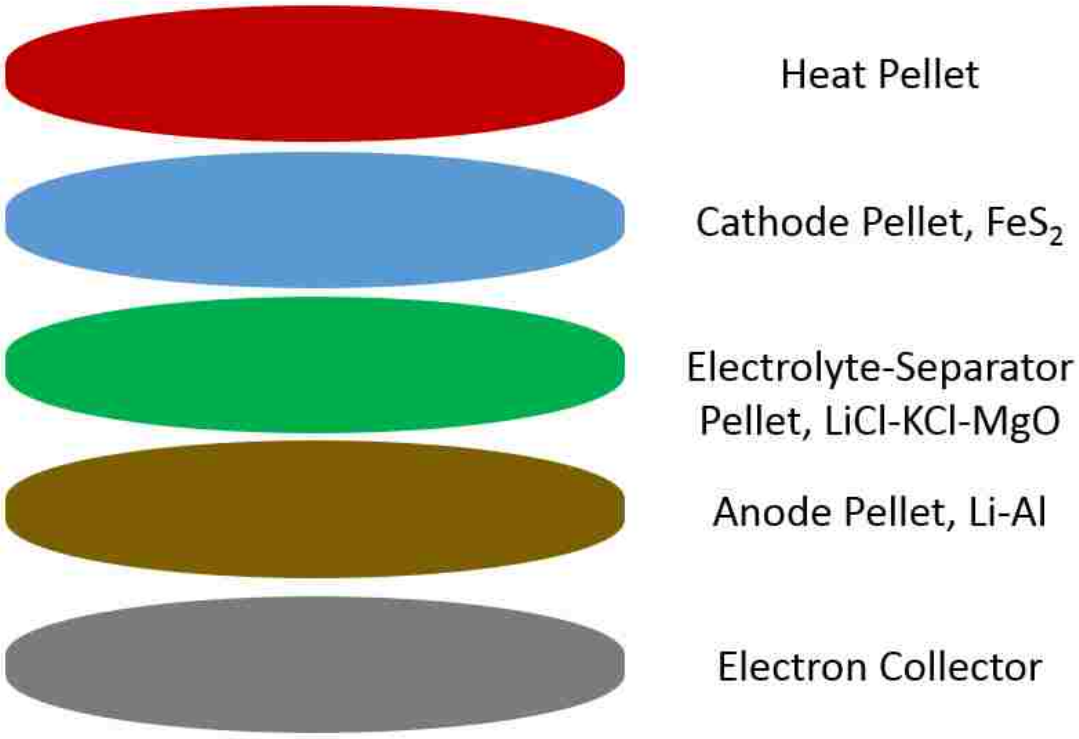

Figure 1: Thermal battery design, temperature is determined by calorific output of heat pellets and insulation design

To activate the battery, a heat source is ignited and the temperature increases to melt the electrolyte. The heat source is an integral component of the thermal battery and the battery activation time is dependent on the ramp up of temperature of the system.

Systems can be activated in milliseconds to hundreds of milliseconds in larger systems. The battery use time is primarily dependent on the ability to keep the electrolyte above the melting point, which is determined by the energy supplied by the heat source and the insulation of the system. Once activated the battery can last anywhere from seconds to a few hours providing high capacity electrical energy in primary, one-time use applications. All thermal batteries are designed for specific power output and application, and improving certain components of the battery will allow for wider use. Many factors are important in the design of thermal batteries including the electrolyte, electrodes, insulation, heat source and stack [1]. The primary focus here will be the heat source.

1.1a Heat Source Requirements

Although there are many factors that dictate the performance and applicability of a heat source, foremost are energetic density and heat output rate. These films are often required to be stable over long periods of time to prevent degradation or misfires but energy release should also be easily and reliably initiated when desired. The reaction must also be gasless due to the battery being in a sealed case, and will be either a conductive or insulating product film, based on specific design needs. Traditional heat sources are based upon deflagrating reaction couples such as oxide exchange processes or fuel and oxidizer mixes[2]. While these are widely applied to thermal batteries, they suffer from slow reaction rates, low conductivity, and significant gas generation. The heat source is a crucial component of the system and improvements will lead to better overall thermal battery performance and improving reliability, capability and reducing costs would allow it to reach larger markets. Improvements that can be made over current heat

source technology are faster ignition times that result in faster activation times for the battery, lower gas generation, and increased energy density. Careful consideration of components is a first step in designing improved energetic thin films.

1.1b Current Heat Source Materials

There are currently two principle types of heat sources in thermal batteries, heat paper and heat pellets. Both of these produce acute high temperatures and the choice between pellet and paper is determined by the need for electrical conductivity. Heat paper is insulating and can be used to transfer heat between cell stacks without shorting, providing a heat source and eliminating electrical conduction between cells and to the cell case. Heat pellets conduct electricity and can be used in between cells in a stack negating the need for additional conducting wires or components. The iron powder heat pellets can't be manufactured with the highest energy stoichiometry, as excess iron is needed to improve the electrical conductivity after combustion, producing 920 J/g (3082 J/cc at 53% packing) at 88% Fe [1]. The fabrication of these heat pellets starts from powder forms which are mixed and then pressed into wafer like discs to be inserted into the thermal batteries. These pellets are formed with approximately 60 tons of forming force and are generally highly porous, with about 50% of the theoretical density which leads to lower volumetric energy output [3]. The unpressed and pressed Fe $KClO_4$ powder are demonstrated below in Figure 2.

Figure 2: Heat pellets formed from powder pressing

1.1c Improving Heat Sources Using Intermetallic Films

Recently, intermetallic reactions between elemental metals have received attention as a thin film template that is fast, high energy, easily initiated and gasless. These energetic reactions have immediate use in thermal battery, microbrazing/soldering and MEMS device applications as well as any other area where point heating is required [4-11].

Intermetallic heat films will be electronically conductive before and after firing and therefore are comparable to the conducting heat pellets that are commonly made of iron powder and potassium perchlorate. These intermetallic films require nanostructuring of the elemental components to minimize the solid state diffusion distances and increase reaction rates. Nickel aluminum composite films release a large amount of energy when mixed at the atomic level and achieve high temperatures (1500 C) in millisecond timescales, having 8451 J/cc heat release at the optimal stoicheometry [1, 8, 9, 12-15].

The heat output of these nickel aluminum flms have been calculated at varying compositions and it is shown that the maximum heat generation is at the one to one stoichiometric ratio, shown in Figure 3. This is the target composition for film fabrication although many films only reach Al_3Ni_2 final composition [5, 14, 16].

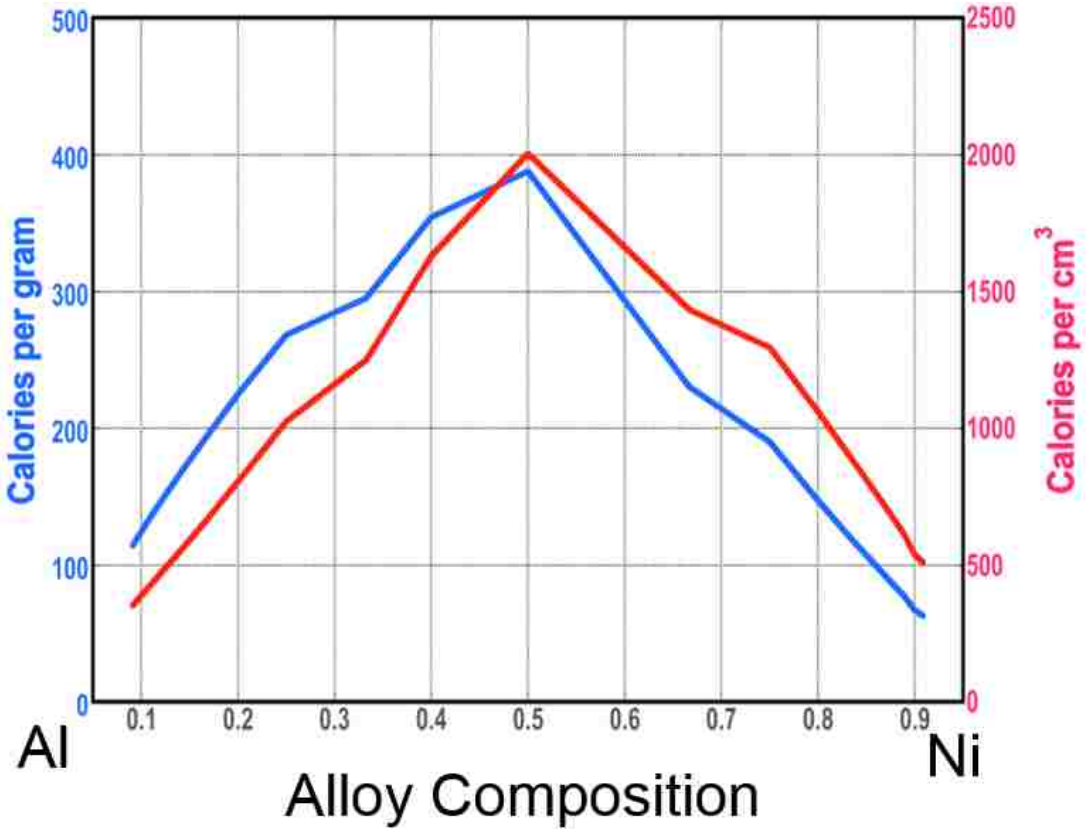

Figure 3: Theoretical energy released during alloying

Total heat release is determined by the overall quantity of heat source material, and the reaction rate can be modified by the geometry of the separate phase volumes. If the phases are large the long diffusion distances may limit the reaction and leave unmixed components in the film, or release heat too slowly to achieve desired temperature ranges. The structuring of the components is therefore critical to the function of these films, necessitating a complex fabrication process. Theoretically, decreasing the diffusion distances should always increase the reaction propagation rate; however, in practice other factors demonstrate an optimum phase size as shown in Figure 4, demonstrating a difference between calculated and experimental results. The theoretical reaction rate increases continually with the progress to smaller phase sizes while the experimental drops to zero at approximately 10 nm. The reaction velocity decreases at very low

thicknesses is attributed to intermixing of the Ni and Al reactants at the phase interface, which becomes more relevant as the volume of interfaces increase [4, 17].

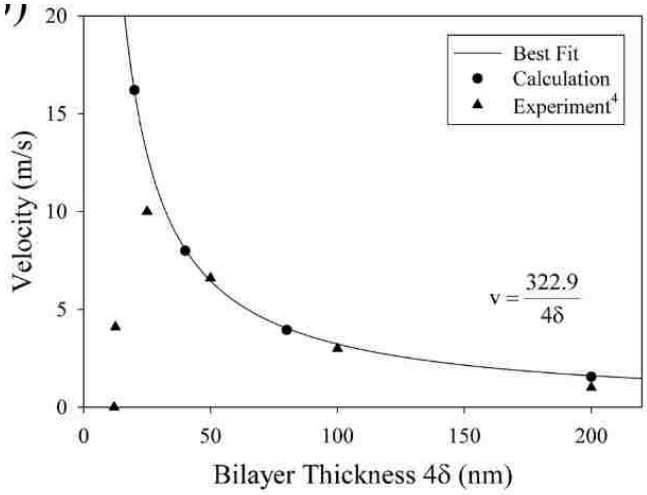

Figure 4: Reaction velocity dependence on bilayer thickness, experimental vs. theoretical [12]

Special consideration must be taken so that the film dissipates energy at a rate that satisfies the fast activation desired in thermal batteries, that the film are reacted efficiently to minimize material waste, and that the reaction rate is controlled such that it reaches temperatures high enough for the cell to operate but not too rapid such that it reaches temperatures high enough to damage components of the cell (e.g. the electrolyte generally has limited stability against the electrode at temperatures 600° C and above) [1].

1.1d Current Fabrication of Intermetallic Film

While the thermodynamics will dictate the total energy released by the reaction, the initiation and self-propagation properties are primarily controlled by diffusive limitations. The components are solid state and therefore demonstrate minimal diffusivities. This makes them useful as heat sources, because they have a long shelf life.

The self-propagating reaction characteristics of these films, once initiated, require the heat generation to greatly exceed the rate of heat dissipation to allow the temperature in the film to rise. The increased temperatures create a regime where diffusion rates are high enough for the components to continue mixing. As the diffusion rates can only be accelerated by temperature to a certain extent, it is necessary that the mixing phases be nanostructured to decrease the diffusion distances. The nanostructuring between reactant phases improves reaction speed and self-propagation reliability [4, 5, 7, 8, 11]. The higher reaction rates can also generate higher reaction temperatures, though the maximum temperatures reached are also dependent on the insulation and heat loss of the system.

There are as many or more methods of processing the various aluminum alloys as there are aluminum alloys, but fabricating these thin films presents challenges as the aluminum and nickel phases must be distinct, relatively pure and have high contact surface area. The necessary nanostructuring in these films is currently fabricated using physical vapor deposition (PVD) methods. This sputtering process deposits layers of nickel and aluminum that are alternatively coated onto a substrate at 20-30 nanometers (nm) each, and this step is repeated until a suitable thickness is achieved (40-150 micrometers). A diagram of these sputtered films and their energetic reaction is shown in Figure 5. The multiple layer process demonstrates relatively poor material and time efficiency. The remedy of this issue is the subject of this dissertation.

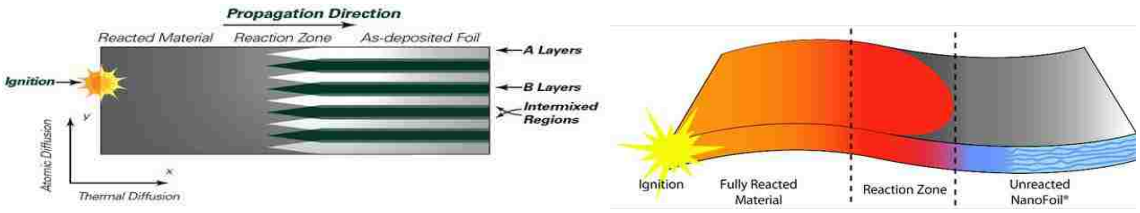

Figure 5: Reaction Initiation in Bilayer Foil Thin Films [12]

The many steps required in this PVD process, as well as operations performed under high vacuum, lend to long processing time requirements and expensive equipment, all of which contribute to a high unit cost (on the order of $\$100/cm^2$ for certain commercial foils). The electrochemical deposition of multiple phase films has been accomplished for decades and is a prime candidate for the fabrication of intermetallic energetics. Electrodeposition is inherently material efficient and the process could produce a composite film faster and cheaper than currently used physical vapor deposition (PVD) methods. The capability to electrochemically deposit aluminum nickel films will prove useful for many fields of industry.

1.1e Electrodeposition Fabrication Methods to Reduce Cost

The technology of electrodeposition has been implemented for centuries in industry for both decorative and functional coatings and more recently in the MEMS and electronics fields [18]. Advantages for the use of electrodeposition over evaporation techniques include the ability to grow films at ambient pressures, inherent material efficiency and the capability to deposit multiple phases in a single step with codeposition methods. Since the films are reactive and intermetallic alloying is accelerated by increased temperature, the fabrication temperature is limited. The alloying reaction is very fast beginning around 130˚ C, so the maximum temperature option for fabrication

techniques was set to 100˚ C. There are several methods to produce an aluminum and nickel composite film; they are detailed below as well as reasons for and against their use.

The immediate counterpart to the physical vapor deposition (PVD) process would be to electrochemically deposit alternating nickel and aluminum layers, each from separate chemistries. In this way we could enhance the material efficiency of the process, but would likely increase the fabrication time. To achieve the desired results it will be required to fabricate the film in a single step.

It is possible to change the deposited phase composition during electrodeposition in an electrolyte without changing the electrolyte composition. This is done by changing the applied parameters (e.g. voltage, temperature, flow characteristics, etc.). In this way it is possible to develop a mixed electrolyte with both nickel and aluminum precursors and change the deposition parameters to produce distinct layers. This will result in a compact and uniform film; but while it would be possible to deposit a pure nickel phase, depositing a pure aluminum phase is likely impossible. The potential for any energy release will be reduced or eliminated if the aluminum phase already has nickel incorporated in it during fabrication.

Another approach is to deposit the phases as already solid composites, and not allow any mixing to happen until the desired ignition time. Although not technically an electrochemical deposition process, electrophoretic deposition, where particles electrophoretically migrate to the electrode and deposit onto the substrate, is a potential candidate in the fabrication of the energetic films. The concept would be to mix nickel and aluminum particles in a specific ratio, suspend them in a liquid with appropriate

conductivity, viscosity and stability, and then drive them to deposit on the substrate with electronic potential. This approach does not require any chemical reactions during fabrication and therfore is simpler than the other methods. This process is very similar to sintering powders and shares some the same problems, such as low packing density and difficulty in controlling particle composition distribution. The low packing density can hinder reaction propagation and will result in a significantly lower energy density in the film.

The best option for producing a composite film in a single step is electrochemical codeposition. This entails the electrochemical reduction of one phase as the matrix, while a second phase exists in the electrolyte as suspended particles and is incorporated in the film through entrapment. This method will produce a compact film that is distinctly two separate and pure phases. The nickel and aluminum binary system can be created through the reduction of nickel species as the matrix and the incorporation of aluminum particles or vice a versa. A codeposited film is shown in Figure 6.

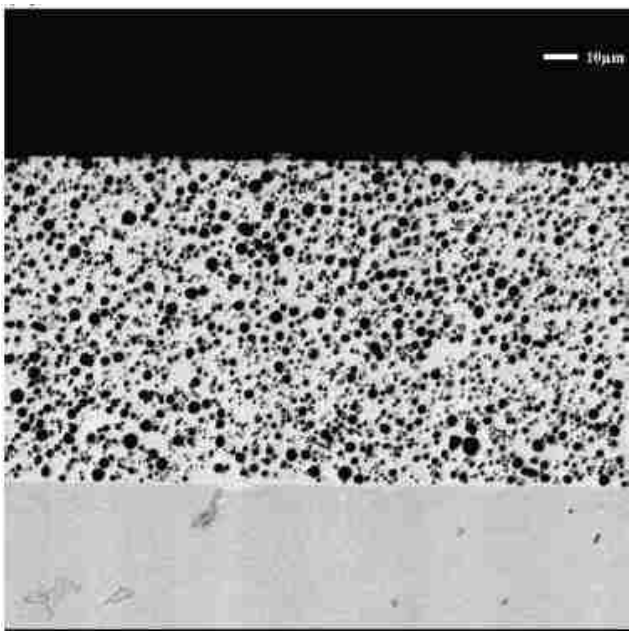

Figure 6: Codeposited film example [16]

1.1 Electrocodeposition

Electrodeposition is a powerful fabrication technique that is inherently efficient and scalable. Electrochemical codeposition is an extension of this process where composite structures can be formed. This process entails incorporating particulates of one constituent into an electrodeposited matrix of another constituent. By adjusting the concentrations of the components, their transport properties, and reaction properties, the stoichiometry can be tailored and controlled[19]. This method leads to phase separated deposits with control over the inclusion phase size and distribution, as well as the ability to electroform molds at thicknesses unachievable in comparable lift-off processes, with significant decreases in time and cost.

While this process has been used to good effect for nonconductive particle inclusions, to date there is less reported work on nano or all metal composites formed in this manner [18-50]. The use and capability of the codeposition process can be traced back to incorporating graphite particles in copper coatings for self-lubricating components in car engines in 1928[19]. The study of these methods steadily increased until the 1990s, where the advantages of composite coatings became apparent in new areas such as electro and photocatalysts and continued with the increasing interest in micro and nanostructured materials[51]. Karbasi et al. worked with incorporating TiC in nickel films to improve wear resistance and claims that “among the processes used to produce nano structured composites, the electrodeposition technique has been shown to have a smoother surface, a better bonding between particles and metal and higher micro hardness”[23]. While the principles of codeposition have been known for decades the

mechanism and optimized conditions are not well understood. This is likely due to the immense number of variables that are inconsistent in each chemistry and application. Some parameters that influence the particle incorporation are the current density, convection in the cell, particle concentration, type, size and shape. The important concepts of a codeposited particles are broken into two sections, the first is the transport of the particle and its adsorption to the substrate surface and the second is the concurrent metal deposition. The forces on the particle are summarized in Figure 7, and are the stagnation forces, shear forces from flow of the electrolyte, friction opposing the direction of shear and the adhesion forces from the particle [50].

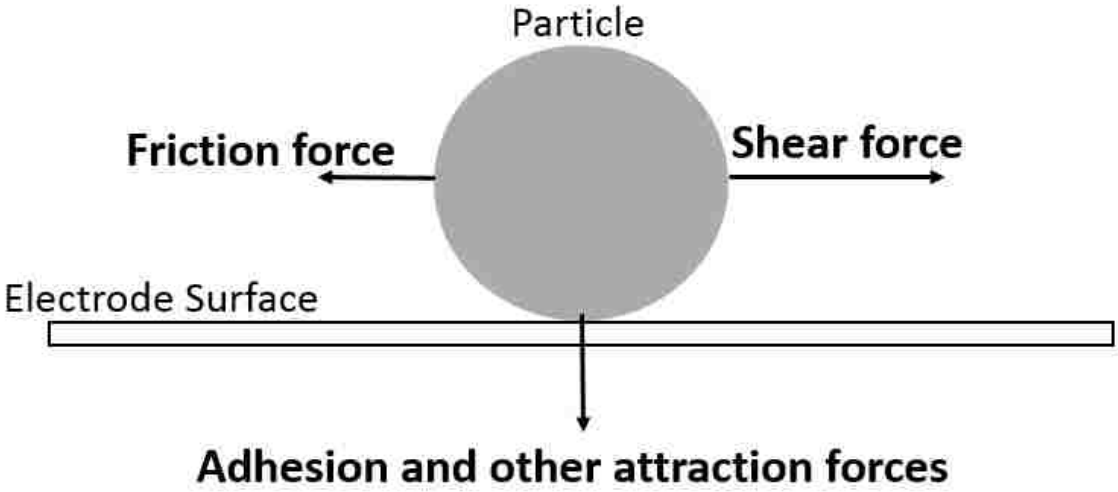

Figure 7: Forces on a particle adsorbed on the substrate [50]

1.2a Fabrication of Intermetallic Films – Nanoscale and Conductive Incorporations

The parameters and forces that are involved in the codepostion process to be developed in this work need to be systematically controlled to acheive the required particle incorporation. The particles must be nanoscale, as the necessary structuring

requires nanoscale diffusion distances. The nanoparticles exhibit low body force to surface force ratios, necessitating high control over many deposition parameters sionce the shear forces will be relatively large compared to the other forces.

The Guglielmi model is a mostly empirical representation of the adsorption and matrix growth process and is a physisorption of the particle from the electrolyte followed by chemisorption and incorporation [52]. This is shown in Figure 8 and is influenced by a Langmuir type adsorption constant, deposition current density and particle loading.

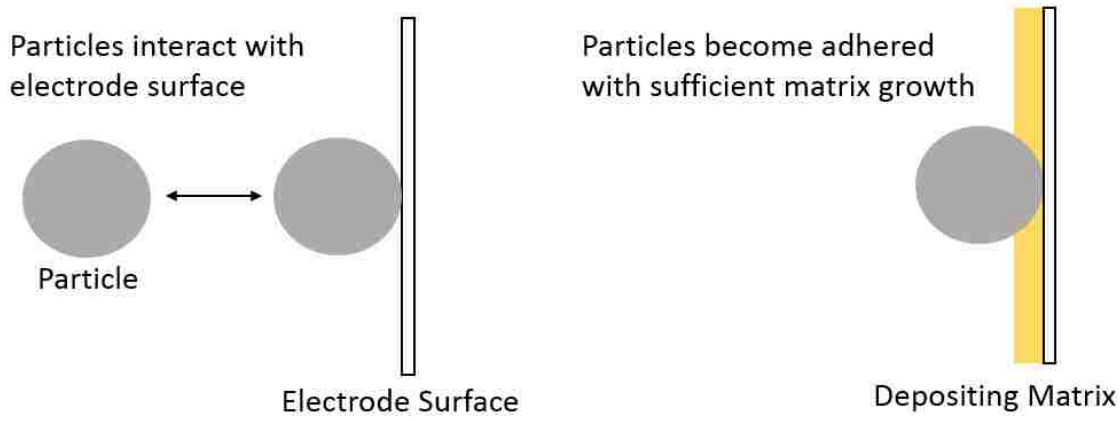

Figure 8: Particle Entrapment

Generally, when incorporating conductive particles, the film is spongy and porous as the particles allow the reducible species to deposit on the surface of the film and matrix growth is not restricted to the substrate. On the other hand, if the particles are not in contact with the surface for enough time (beyond the critical residence time) the particles get preferentially coated with the matrix metal and removed without being incorporated. The rate of particle arrival to the substrate, the residence time of the particle and the growth rate of the metal must be matched and optimized to minimize lost particles and porosity in the deposited film. Examples of circumstances with too high or too low of shear on the substrate with respect to matrix growth rate is shown in Figure 9.

Again, the shear forces due to fluid flow are exceptionally influential as the particles are nanoscale, and the surface forces are exceedingly strong, and balancing particle loading, electrolyte flow and deposition rate will be critical in acheiving the deseired stoichiometric ratios, qualtiy depositions and satisfactory deposition rates.

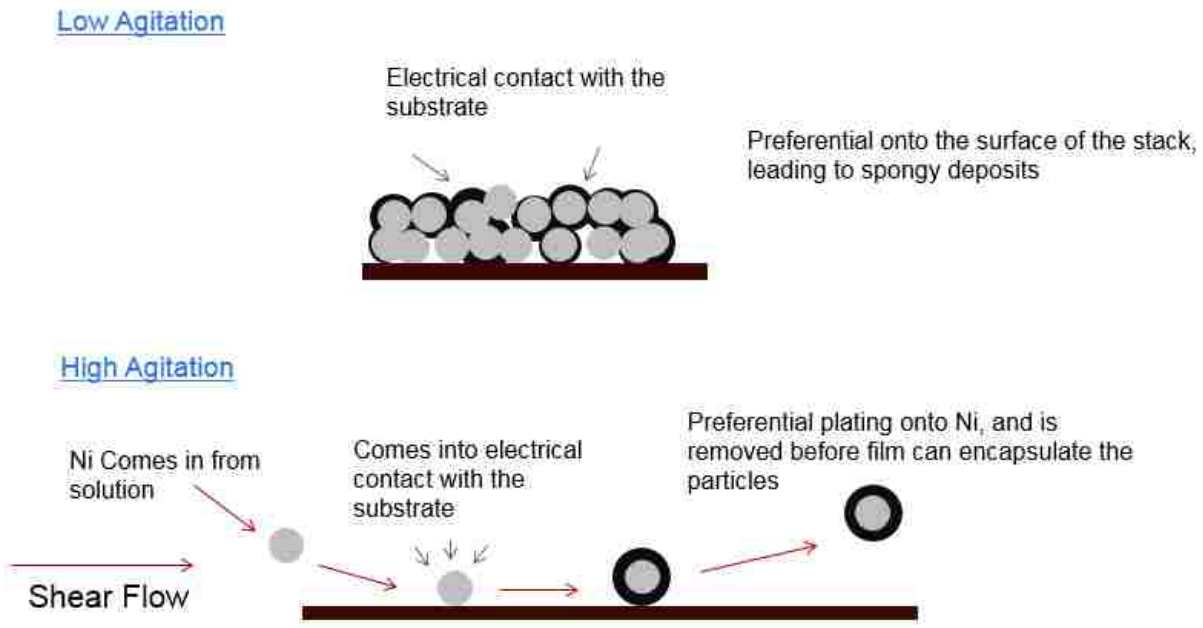

Figure 9: Examples of too Low or High of Shear During Codeposition

1.2b Sedimentary Deposition Techniques to Increase Incorporation

Development of this process would find use in thermal batteries, microbrazing/soldering, joining, cauterization and microelectromechanical systems (MEMS) device applications as well as any other area where point heating is required [5, 8, 10, 17, 53]. The energy output of the codeposited film will depend on the ability to incorporate particles into the matrix at the desired stoichiometry, size and geometry. This process can be optimized by modifying the electrolyte, particle chemistry/dimensions, reaction vessel, temperature, and matrix deposition mechanism [18]. To achieve the high

required particle loadings, sedimentary codepositon may been implemented. Sedimentary codeposition adds the influence of gravity to bring more particles to the substrate and increase their residence time. A schematic of the sedimentary codepostion apparatus is shown in Figure 10.

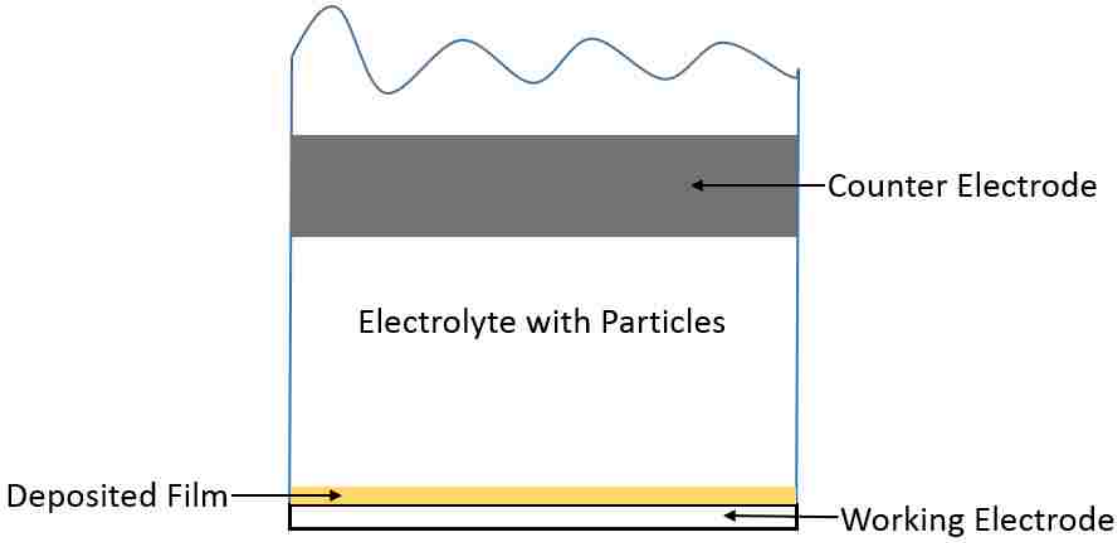

Figure 10: Sedimentary Codeposition Processes

The incorporation of particles needs to be well controlled, as poor dispersion of particles, low particle incorporation or too large a particle size will lead to long diffusion distances and times in the thin film, causing the energetic reaction to quench. The structuring of the components necessitates a fabrication process that controls this distance.

Codeposition for the specific purpose of producing energetic thin films is an applicable process because it has the capacity to produce nanostructured composites at high rates, potentially 100 of um/hour, and temperatures low enough to minimize solid state reactions. Success relies on the depositing matrix phase being smooth and dense and

the particulate suspension homogeneously dispersed in the electrolyte and have adequate transport to the electrode.

The electrochemical codeposition depends on the ability to transport the suspended particles to the electrode. Particle transport is influenced by several fundamental forces including diffusion, convection, electromigration, gravitational, and magnetic depending on particle properties. A higher concentration of particles in the electrolyte leads to a higher incorporation in the film but reaches a maximum and further loading increases the solution viscosity and reduces the conductivity without benefit [30]. Conditions must be optimized considering all factors, as differing particles sizes and systems require different conditions, as shown in Figure 11.

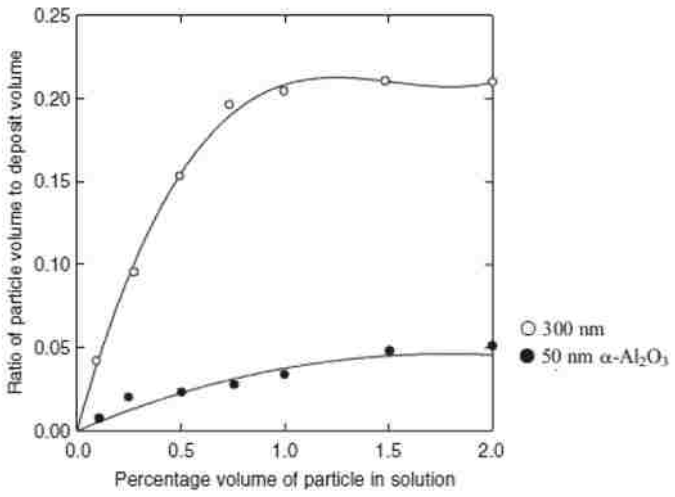

Figure 11: Particle Incorporation Dependence on Particle Size [27]

Physical agitation is the primary method for keeping particles suspended and bringing them into contact with the electrode. This trend exhibits a maximum but then also decreases rapidly [30]. Low agitation near the electrode does not seem to exhibit much influence on particle incorporation in the case of micron sized particles, but increases as the regime shifts towards more turbulence. The trend then begins to decrease

as increased turbulence decreases the residence time. This is likely due to increased particle convection towards the electrode with increasing agitation and then at a critical point, depending on solution viscosity and particle size, the shear forces drive the particles off of the electrode before they can be entrapped. This trend is shown in Figure 12.

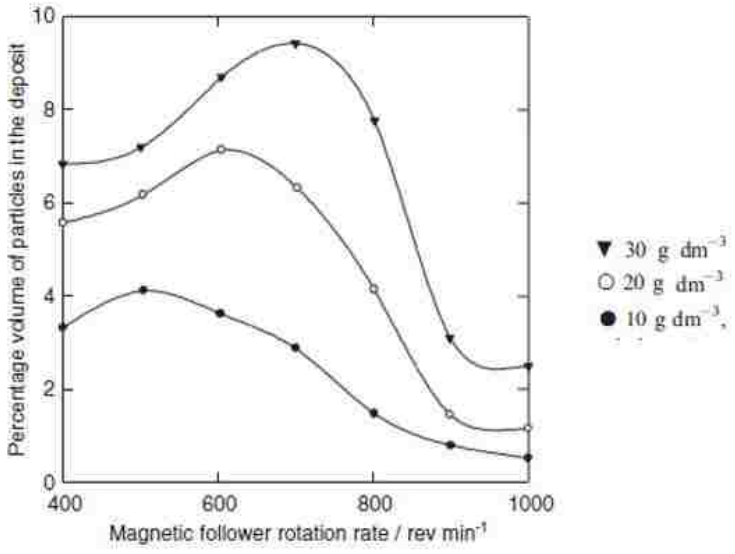

Figure 12: Particle incorporation dependence on particle size and agitation [27]

The Guglielmi model describes the incorporation of particles by first a weak agglomeration on the surface and then a kinetically controlled irreversible adsorption and entrapment by the metal matrix [26]. This model has been shown to be viable in many codeposition systems, including metal particle inclusions although only in aqueous chemistries[54]. Other models have expanded on the Guglielmi model but system responses vary on a case by case basis, the Guglielmi model remains a good measure of important initial parameters.

The reduction of the matrix material to its metallic state is also central to the codeposition process. Higher percentages of the matrix material result in a decrease in

particle incorporation volume, so controlling the relation of particle arrival to matrix deposition rate is essential. It has been shown that increasing the particle loading in the electrolyte will lead to increased particle incorporation in the film, and decreasing the matrix precursor concentration in the electrolyte will also lead to increased particle incorporation at a given reduction potential [41]. To further increase the particle incorporation, it has been observed that decreasing the deposition rate allows more particles to adsorb to the surface during film growth, increasing the particle concentration in the film[30]. Decreasing the rate can be achieved through decreasing the current density applied or moving to a pulsed deposition. The pulsed deposition is preferred as the deposition characteristics of a certain plating regime can be kept, and too low of a current density can result in poor deposit qualities. Optimum micron and submicron particle incorporation is in the realm of lower current densities, while nanoparticle incorporation benefits from slightly higher current densities [28]. These trends are consistent with most experimental and theoretical results, but the correlation values can vary significantly depending on the system under investigation; most of the properties and trends have to be confirmed for a specific system in question [19].

1.2c Mitigating Particle Agglomeration

Physical and chemical methods can be used to improve migration of the particles to the cathode. Surfactants will slow particle agglomeration, improve suspension stability and can control zeta potentials increasing electromigration toward the electrode[28]. Many particles have been incorporated in various metals in aqueous solutions, namely copper composites with particles kept in solution by rapid stirring [54]. The size

distribution shifts if the particles agglomerate. Particle agglomeration can have important consequences for particle transport, as larger particles tend to settle more rapidly under gravity but diffuse more slowly. Stable dispersions result from modifying attractive and repulsive forces. The theoretical background for stable colloidal solutions is derived from DLVO (Derjaguin-Landau-Verwey-Overbek) theory [55]. The attractive Van der Waals forces and repulsive electrostatic forces compete and are modified by controlling the zeta potential. Figure 13 emphasizes the importance of surface modifications to control the electrostatic charge, generally zeta potentials of 30 mV or higher result in stable colloid solutions.

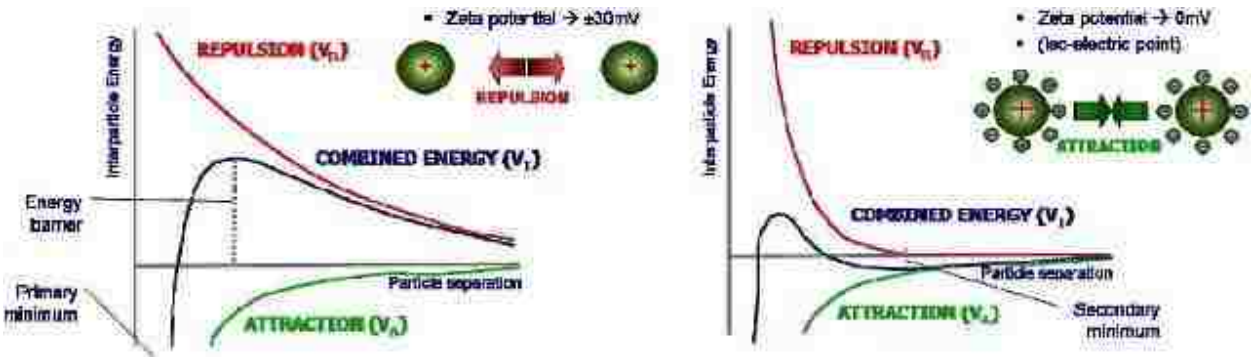

Figure 13: Colloid stability based on zeta potential [55]

Sodium dodecyl sulfate is a common additive in aqueous chemistries and was reported to improve dispersion, uniformity and quantity of SiC particles in a nickel deposit[22], but the additive used will have varying efficacy depending on both the particle and electrolyte properties. Accurate investigation of particle properties in the electrolyte is important for understanding suspension, transport and incorporation. Ionic liquids tend to keep particle suspensions stable over relatively long times, due to both increased viscosity as well as increased charge screening. Surface modifications could be oxide layers, adsorbed ionic species or long chain surfactants. Controlling particle

agglomeration is crucial as agglomerated particles reduce surface area and will decrease component mixing rates if translated into the energetic thin film.

1.2e Matrix Deposition

In a nickel aluminum film it is evident there are 2 choices for configuration, use of Ni as a matrix phase with Al particles, or the use of Al as the matrix phase with Ni particles. Nickel ion reduction occurs at -0.23 V vs. NHE, which is well within the electrochemical limits of water (water will reduce at potentials more negative -0.83 V vs. NHE). Since nickel can be deposited in aqueous chemistries this process was developed in the early 1800s, a nickel deposition process was first patented in 1840, and has been used regularly since [56]. This process would be ideal but there are some limiting factors. The greatest benefit would be the use of an aqueous electrolyte, but aluminum particles readily form an oxide layer in water and it can be a substantial portion of the particle volume. The codeposition process is also limited in ability to incorporate high volumes of particles, as the matrix is almost always a significantly higher volume portion of the film, and stoichiometrically desired mixtures are NiAl or Ni_2Al_3 because of the higher energy density, and these are Al rich by volume. Given the density differences of nickel and aluminum, the film must be 60% or greater aluminum and therefore aluminum is required to be the matrix material to achieve optimal stoichiometric ratios for the maximum heat output. Achieving this ratio with conventional electrocodeposition processes is not possible (limited to <30% volume particles, increases to 40% with sedimentary codeposition processes).

Aluminum is the most abundant metal on the earth's crust, and its low cost makes it a good material candidate in most fabrication processes. It has a variety of properties that make it ideal for use in many applications such as high thermal and electrical conductivity (59% of copper and 30% less weight), a high strength to weight ratio when alloyed with other metals, and good resistance to corrosion [57]. The properties of aluminum and aluminum alloys have value in applications of almost every field from aerospace to micro-electronics. The original production of aluminum from aluminum ore, primarily bauxite, is a complex, long and energy intensive process that involves high temperature melts and electrochemical methods. Recycling of this metal, however, is theoretically capable of 100% material efficiency and can require as little as 5% of the energy of original production [57].

Since aluminum reduction occurs at -1.67 V vs. NHE, aqueous solutions are not applicable as electrolytes (water reduces to hydrogen gas at -0.83 V, nickel reduces at a more noble potential as well, this is why the use of a combined bath for layer by layer growth is limited; a pure aluminum phase can't be deposited with the exclusion of nickel in a mixed chemistry). Aluminum deposition requires an electrolyte with an electrochemical window that is stable during the aluminum reduction, it must facilitate the aluminum reduction process and must have high precursor solubility and suitable ionic conductivity. There are many electrolytes that could fit these criteria, they include high and low temperature molten salts as well as many aprotic solvents. From an engineering standpoint it is important to choose an electrolyte that is low cost, easy to use and has high quality control [18, 52].

1.2 Aluminum Deposition History

Many variables need to be considered when choosing or designing an electrolyte, especially so when objectives such as high quantity conductive nanoparticle codeposition are involved. In general, there are 4 classes of components. The solvent is usually the largest portion of the electrolyte. A precursor is the source of material or ions that lead to the desired reaction (in this case an aluminum salt that will reduce to aluminum metal). Conducting salts are used to increase the ionic conductivity of the chemistry and are stable in the operating regime and do not react with the ions or electrodes. Addition agents can adsorb on the electrode surface and modify deposition morphology characteristics, while complexing agents can shift reduction potentials of components in the electrolyte, making them more or less active [18, 52].

1.3a Aprotic and Hydride Baths

Early aluminum deposition revolved around aprotic solvents that were typically volatile [58]. Many organic solvents have unsuitable electrochemical windows (e.g. acetone, alkyl halides etc.). Some of the first production electrolytes used diethyl ether, and there was significant work done to improve this chemistry. Initially the chemistry was 2-3 mol/L $AlCl_3$ in diethyl ether, with 1 mol/L LiH. $LiAlH_4$ was substituted out for LiH in lower concentrations, which improved the deposition properties, but the bath suffered drawbacks such as high fire hazard, limited lifetime, need of frequent composition control and low current efficiency at the anode, as well as hydrogen generation and subsequent embrittlement [59]. Many replacement solvents were found,

one of the more notable systems based around Tetrahydrofuran (THF) [60-64]. Addition of aromatic solvents to the THF bath improved preparation and operating conditions but reduced the total throwing power of the chemistry, likely due to the increased viscosity and reduced conductivity [65].

1.3b Aromatic and Dimethyl Sulfone Baths

Since the solutions made from early aprotic solvents are typically volatile, hygroscopic and difficult to handle, deposition of aluminum from lower vapor pressure aromatic hydrocarbons became a concurrent/next gen low temperature aluminum deposition process [58, 59, 66, 67]. Since AlF_3 is insoluble in aromatic hydrocarbons and $AlCl_3$ shows very low solubility, $AlBr_3$ was used and these electrolytes are known as bromine baths. Non-complexed bromine baths are simple two component electrolytes but suffered from low conductivity and throwing power. To increase the conductivity various additives were implemented, mainly alkali halides. These baths showed high current efficiency and homogeneous deposits with good adherence but these properties were mostly only seen at very low current densities (~1 mA/cm^2). The dimethylsulfone and $AlCl_3$ bath is a prime candidate for electrodeposition of aluminum and has already demonstrated high deposition rates and thicknesses [68-72]. These $DMSO_2$ solutions have successfully codeposited Si, SiO_2, Al_2O_3, TiB_2, and hexagonal BN particles in an Al matrix, while the only drawbacks are the required operating temperatures of 120-150°C and slight impurity incorporation (sulfur and chlorine) although Al purity is >99% [73, 74].

1.3c Molten Salts and Ionic Liquids

Molten salts (MSs) are unique electrolytes, for example, NaCl and $AlCl_3$ salts at the right ratio is liquid at ~150 C, since it is a liquid additional solvents are not required and this allows for extremely high salts concentrations. The NaCl also complexes with the Al precursor to form a reducible species, and the entirety of the solution is ionic which contributes to its ionic conductivity [75, 76]. There has been an initiative to produce MSs with lower operating temperatures, and salts with melting points below 100° C are commonly referred to as ionic liquids (ILs), in this dissertation IL will refer to salts that are liquid at room temperature [77, 78]. Ionic liquids (ILs) are relatively new electrolytes that have gained growing interest and understanding in the past 2 decades. They are good candidates for electrochemistry because they can be designed to have wide electrochemical windows, high salt solubility and negligible vapor pressures [79, 80]. Problems with molten salts usually include high viscosity, high operating temperature or the room temperature ILs are relatively expensive.

1.3 Ionic Liquids for Aluminum Deposition

Chloroaluminate ILs have chloroaluminate anions and are considered first generation. These chemistries are well designed for aluminum plating. The synthesis of larger cation species has pushed the melting point and glass transition temperatures of these salts below room temperature, although viscosities as still usually high compared to molecular solvents. These viscosities are mostly due to the high electrostatic attraction forces between the ions. When a salts such as butyl-methylimidazolium chloride

(BMImCl) or trimethyl phenyl ammonium chloride (TMPAC) is mixed with aluminum trichloride ($AlCl_3$) the Lewis acidity of $AlCl_3$ forces a reaction that forms aluminum anionic species including $AlCl_4^-$ or $Al_2Cl_7^-$ or higher order species depending on the stoichiometry of the mixture [81, 82]. These cations and anions are bulky and have delocalized charges, which decrease their attraction to each other and lower their ability to orient and form solids. At appropriate ratios these chemistries melt well below room temperature validating their use at ambient conditions. With regards to aluminum deposition, the $Al_2Cl_7^-$ complex has been found to be the species that takes part in the reduction process. For this reason, most aluminum plating in ILs utilize chemistries with around a 2:1 $AlCl_3$ to Cl component, as this promotes generation of the stoichiometric $Al_2Cl_7^-$ species. Considerations such as cost, electrochemical stability, throwing power, conductivity and efficiency need to be considered in determining the best system for aluminum thin film fabrication.

1.4a Cations, Anions and Co-solvents

Ionic liquids were implemented to try and improve upon the organic solvents listed above, the first that saw more widespread use was $AlCl_3$ and ethylpyridinium bromide (EPB) (2:1 molar) and saturated with benzene or toluene [59]. These deposits were suitable for applications at the time, but suffer from photodecomposition, room temperature melting only at the 2:1 ratio, and limited electrochemical window. N-(1-butyl)pyridinium chloride (BPC) $AlCl_3$ was a very popular IL of study about 25 years ago, this solution had a wider electrochemical window than EPB, but it's high viscosity resulted in low ionic conductivity although it was still higher than typical non-aqueous electrolytes. It was confirmed that the electrolyte could be improved with no drawbacks

by dilution up to 50 vol. % benzene [83, 84]. The benzene was shown to have no effect other than decreasing the viscosity and increasing the solution conductivity [85].

Trimethylphenylammonium chloride (TMPAC) received considerable attention due to its relatively low cost but has not seen use recently as the deposition quality was always rough and thick compact coatings are difficult to achieve. $AlCl_3$ TMPAC solutions are liquid at room temperature only around the 2:1 molar ratio, however, at this composition the freezing point is depressed to -70 ˚ C [58, 86]. Alkyl imidazolium chloroaluminates such as 1-methyl-3-ethylimidazolium (EMImCl) and 1-butyl-3-ethylimidazolium (BMImCl) seem to be the most widely investigated and used aluminum deposition electrolytes presently. These solutions have electrochemical windows that allow for significant overpotential with regards to aluminum reduction and much higher conductivities that the previous generations. BMImCl $AlCl_3$ solutions show higher ionic conductivity and better quality deposition than TMPAC, and with 30 vol% dilution with toluene give smooth adherent aluminum coatings [87]. The dilutions with aromatics heavily influence the properties of the electrolyte, decreasing the solution viscosity, breaking up electrostatic interactions and increasing the ionic mobility. Dilution with aromatics such as benzene, toluene or ortho-dichlorobenzene (DCB) result in an increase of ionic mobility and overall conductivity, as well as reduction in overall cost [85]. The effects of these dilution agents vary with type and concentration, for example toluene has very low viscosity but also low permittivity, high vapor pressure and limited miscibility with chloraluminate ILs. DCB has higher viscosity and cost than toluene, but shows full miscibility and higher permittivity. Diffusion of both the reduced species and particles will influence the film composition, morphology and limiting growth rates. It is possible

to modify the viscosity of the electrolyte with temperature adjustments. ILs have been measured to undergo several factors reduction in viscosity in only 60C change, this will have a significant impact on the deposition and is investigated in chapter 6. Co-solvents have a more dramatic and immediate effect as they can be as low as .5 cP and impart their properties instantly when mixed in solution. Co-solvents however, greatly change the electrolyte properties, regardless of how inert they are. The most negative consequence of this is the imparted vapor pressure to the IL, as well as the possibility of side reactions over the life of the chemistry. Optimal deposition parameters may require a mixture of salts and solvents as well as additives and modified temperature of operation. Neat EMImCl and $AlCl_3$ mixtures deposit aluminum readily, these solutions are higher conductivity and lower viscosity than the neat BMImCl solutions [58].

Much investigation has been done on the EMImCl solutions but it is still in the early stages of development as a commercially applicable aluminum deposition electrolyte [88-96]. This is evidenced by the continual publication of new papers attempting to optimize and investigate the deposition process, as well as negligible commercial use [87, 97-102]. Most of these papers investigate the temperature, potential and composition parameters. It has been shown that quality deposits are nearly impossible to achieve in low or no agitation regimes. This is likely due to the low diffusion rates of the reducible species. The diffusion limitations can be overcome by incorporating significant agitation of the solution but studies in this regard have not been carried out thoroughly [96, 101, 103]. As evidenced by the strong influence of intentional ionic species changes and addition of co-solvents, impurities strongly affect the ionic liquid properties [104]. To minimize the impact of impurities in high precision

electrochemical and physical property investigations, cleanliness and purification is required and has been developed quite thoroughly in the literature. As the Aluminum species is extremely reactive and forms stable conformations when mixed with water or oxygen is it very difficult to remove these components once the ionic liquid has already been synthesized. Starting with clean components is the best and only way to ensure consistent chemistries are produced [105, 106].

It has also been shown that ionic liquids do not function like molecular solvents in regards to double layers near the electrode [79, 107-112]. ILs have a multilayer architecture in the vicinity of electrodes and the electrodeposition of aluminum and tantalum are strongly influenced [98]. These layers are affected by reduction potential and shear, which force mixing and property changes in the IL. Development of the understanding of these properties under dynamic conditions used for plating is vital in an electrodeposition system. These properties effect the diffusion and availability of reducing species, and the balance between diffusion and kinetics is fundamental to controlling the growth mode and generating a smooth and compact composite film. The kinetics are predominately controlled by the reduction potential and the temperature of operation, and these variables also need to be investigated on a system by system basis.

1.4b Properties – Viscosity, Conductivity and Mobility

The viscosity is especially important in IL electrolytes as it is one of the weaker points, typically the viscosity in ILs are an order of magnitude or higher than molecular solvents, but most that are considered for use are below 100 cP. The viscosity of ionic liquids is attributed to different inherent aspects. One theory is that ionic liquids are

viscous because the ionic mobility is restricted to hole transport and limited by the open volume in the solution. These holes are typically small compared to the large ionic species [113], and the higher attractive forces from the charged species result in smaller free volumes than most molecular solvents (15-20% in ILs compared to 22-26% in molecular solvents) [114]. The viscosity is also attributed specifically to the high attractive electrostatic forces, although van der waals forces contribute some as well. This has been shown by Tokuda et al in their extensive study of the physiochemical properties of ionic liquids with varying cationic chain lengths, demonstrating that increasing the chain length on imidazolium cations with a consistent anion species results in increasing viscosity [115-119]. Tokuda et al. did a comprehensive study including the diffusivities of the ionic species derived from pulse field gradient spin echo NMR and showed that there is significant alignment with the summation mobility of the anion and cation and viscosity trends, with increasing mobility resulting in decreasing viscosity. They also show that increasing cationic chain lengths in imidazolium cations decreases the mobility of the cations, which decreases the conductivity but disproportionately compared to the decrease in mobility. Increasing chain lengths was also shown to increase viscosity and this is assumed to be from increasing inductive forces between the ions, showing that electrostatic forces are dominant, but there are other intramolecular forces that are relevant under certain circumstances. Anastasia et al used vibrational spectroscopy to demonstrate in certain TFSi ILs with carbon chain lengths from 0-3, the coulombic interactions dominate and with carbon chains >3 van der waals and pi-pi interactions become important [120]. The method of investigation is centered around the PGSE technique, which is described in Chapter 3. It is well accepted this technique gives

accurate measurements of the self-diffusion coefficients. The theoretical conductivity is calculated from the diffusion coefficients and ionic concentrations using the Nernst Einstein equation, Equation 1: Nernst Einstein Ionic Mobility and Conductivity RelationEquation 1.

Equation 1: Nernst Einstein Ionic Mobility and Conductivity Relation

$$\Lambda = \frac{N_A e^2 (D_{Cation} + D_{Cation})}{kT}$$

These calculated conductivities are consistently higher than the experimental values, indicating there may be more contributions toward the conductivity than directly applied mobility, possibly ion pairing that decreases conductivity contributions. They do however show correlation and it is understood that these factors are strongly correlated [121, 122]. The ILs properties can vary significantly by changing anions and cations, and as one would expect, the properties are strongly correlated to the size and charge of each species [123]. Spohr and Patey demonstrate that the properties are influenced by the relation of size of the species, charge location and charge dispersion [124-126]. The interactions of these species may be broken up under shear conditions, possibly generating the significant number of non-Newtonian ILs that are consistently thixotropic [127-129].

The experimental rheology of ionic liquids is very complex [130]. The different ionic components in the various ILs display varying degrees of clustering and at different temperatures. These clusters break up under shear stresses and can be probed by rheological studies. Breaking up these clusters and decreasing the interaction energy of the components should result in changes in mobility either from reduced electrostatic attraction or increasing probability of an ion interacting with an appropriately sized hole

to diffuse through. The deviations that the ionic liquids undergo when experiencing shear are not accounted for in many experiments, where the properties are tested under static conditions (NMR, Cottrell, density, conductivity etc.). Using rheology to probe how the ionic interactions change under shear will allow for investigation into how these properties are shifted in dynamic conditions.

Chapter 2: Aim of This Work

The focus of this reasearch is the fabrication of an exothermic aluminum nickel thin film. The process parameters, the energetic properties of the codeposited film, and the correlation between the fabrication and the film properties are to be investigated. To reduce costs, the film will be fabricated with the codeposition of an aluminum matrix and nickel particles as outlined in Figure 14.

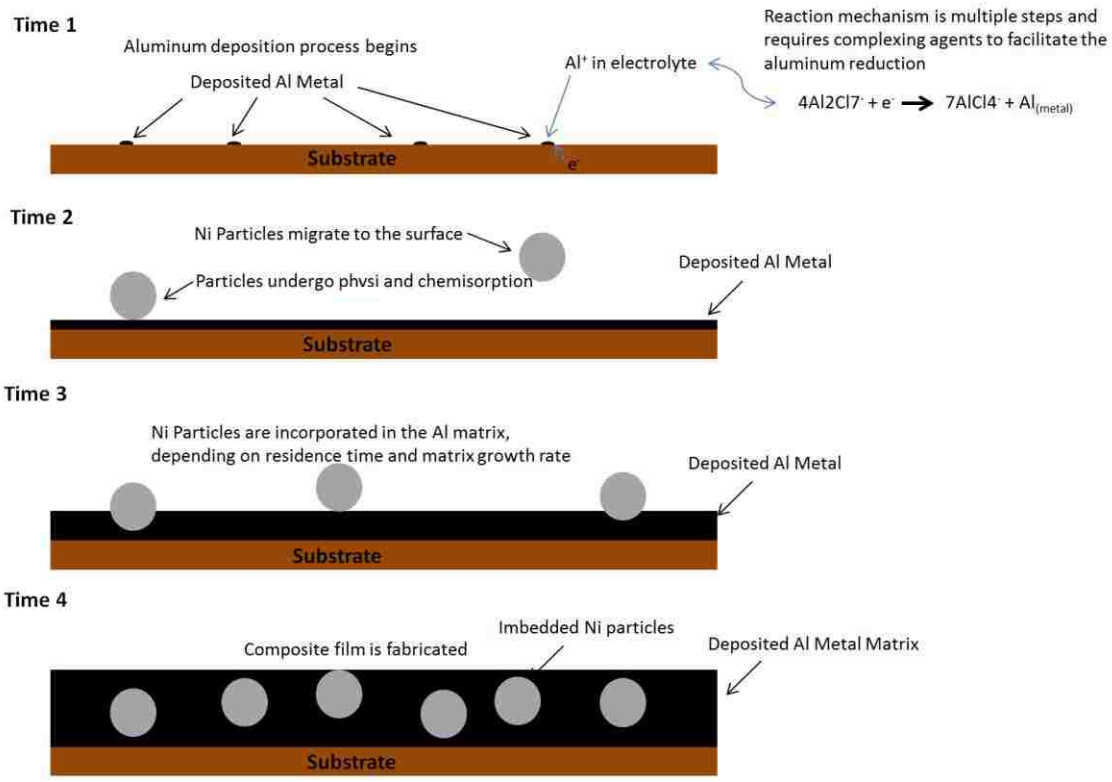

Figure 14: Electrochemical Codeposition Outline

At time 1, the metal (aluminum) deposition begins on the electrode. At time 2, particles make their way to the surface due to convection and gravity. At time 3, the metal matrix grows around particles locking them in place. At time 4 the particles are

imbedded in the film. Composition is determined by metal deposition rate, flux of particles to the electrode surface and residence time.

The self-propagating intermetallic mixing of aluminum and nickel reaction requires intimate and high surface area contact of distinct separate phases. High speed and uniform reaction rates will improve the performance of the energetic film, and this mixing reaction rate is determined by diffusion limitations of the components, as they are initially in the solid state. Faster rates and shorter battery activation times can be achieved by nanostructuring the composite, through the increase in surface area, and therefore the incorporated particle phase must be nanoscale. As detailed in chapter 1, the components are targeted to be 1:1 Al:Ni atomic ratios since this is the most energetic composition, necessitating 60 volume percent aluminum. The particle incorporation volume in the film is the lower volume component, so the particles must be nickel and the deposited matrix material must be aluminum.

Particle incorporation 40 volume percent is still quite high, and requires significant optimization to be reached. Increasing the particle loading in the electrolyte increases incorporation into the deposited film, but has limitations when the particulates are conductive as in this process. If conductive particles are allowed to accumulate on the electrode they will produce a porous spongy deposit, thus the particle loading in the electrolyte is limited. The particle incorporation volume is dependent on particle arrival rates to the electrode and residence times there. The residence times are determined by a balance of forces between attractions to the electrode and shear forces from the electrolyte flow. The particle motion through convection is necessary to bring particles to the electrode surface, but as the shear forces are relatively large since particles are

nanoscale, even low flow rates have a tendency to remove particles before they can be incorporated. Balancing particle arrival rates with the shear forces that remove them, along with developing the matrix growth parameters under these conditions requires extensive knowledge and control of the matrix growth and particle motion in parallel.

The growth of the matrix material is central to the codeposition process and all variables must be investigated and understood. As the requirements for particle incorporation will likely limit electrolyte flow, the electrodeposition will need to be accomplished with minimal agitation. This limits the mass transfer of reducible species and the deposition must be significantly optimized to provide high quality compact deposits in this regime. The nanoparticles will have low residence times, and therefore the matrix growth rate will have to be fast enough to ensure incorporation. While aluminum electrodeposition is not uncommon it is a relatively new and unexplored process, with limited information on surfactants and addition agents that modify and improve the deposition.

Achieving high particle loading in the film while limiting the loading in the electrolyte, along with depositing high rate and compact aluminum with limited electrolyte mixing, necessitates extreme optimization. Theoretical modelling, electrochemical measurements, and study of physical properties of the electrolyte and particles will be used to reach these goals. Understanding and control of the aluminum deposition, particle properties and fluid dynamics is crucial in fabricating a film with the desired energetic properties and developing that process is the subject of this work.

Chapter 3: Experimental

3.1 Chemical Cleaning – Ionic Liquid Preparation

Electrochemistry in general is a high precision technique and impurities have significant impact on results of experiments. The electrolytes and deposited films are highly reactive with oxygen, water and other impurities so significant steps must be taken to ensure tests are repeatable and accurate. To minimize contamination all experiments and purification steps were performed either in a VAC Atmospheres Omni glovebox under argon and less than 1 PPM water and oxygen content or on a Schlenk line under vacuum or with Argon (99.999%, UHP, Matheson).

Ethyl methyl imidazolium chloride (EMImCl) aluminum chloride ($AlCl_3$) electrolytes were purified using chemical and electrochemical techniques. Ethyl-Methyl imidazolium >99% was received from TCI America with a 99.7% assay specifically requested lot. The EMImCl was dried in a Yamato ADP300C vacuum oven, Figure 15, for at least 12 hours at 90˚ C and brought into the glovebox antechamber at elevated temperature. It was allowed to cool under vacuum in the antechamber overnight to further reduce water content.

Figure 15: Yamato ADP300C Vacuum Oven

$AlCl_3$ (Fluka, puriss, anhydrous, crystallized, ≥99.0% (AT)) was cleaned by sublimation at 130˚ C and deposited on a liquid nitrogen cold finger five times to ensure purity. Sublimation was done with 1% NaCl (99.9% Sigma Aldrich) and aluminum wire (Alfa Aesar, annealed, Puratronic®, 99.9995%) in the sublimation vessel in a process given previously by Wessercheid [106]. Initial sublimations were yellow, Figure 16, and became whiter with successive sublimations. The final product was pure white powder and small flakes.

Figure 16: Sublimed Aluminum Trichloride

EMImCl-$AlCl_3$ solutions were made by slow mixing of the purified chemicals and underwent electrochemical purification by running 1 V potential (Solartron Modulab potentiostat) between Aluminum wire or foil (99.999%Alfa Aesar) counter electrode and aluminum wire working electrode (99.999% Alfa Aesar). The cleaned solutions were then filtered over Cellite 550 (Sigma Aldrich) for large volumes or through .45 um GHP lur lock filters (Pall) for volumes under 30 mL, to remove any solids that may have been present or generated. The solutions were then an optically clear very light yellow tint regardless of $AlCl_3$ content. Visible differences can be seen between the electrolyte purified in this manner vs. as received, Figure 17.

Figure 17: Cleaning Results in EMIm Tetrachloroaluminate ILs

BMImCl (95% BASF) and TMPAC (98% Sigma Aldric) were vacuum dried overnight at 90˚ C and brought into the glovebox hot. These solutions were mixed with >99% AlCl3 (sigma Aldrich) that was used without further cleaning. The IL, once prepared, was cleaned via electrochemical methods by applying 1 V (Solartron Analytical potentiostat) between 2 aluminum wire electrodes (Alfa Aesar 99.9995%).

3.2 Karl Fisher Titration

Solutions were tested for water content with a Mettler Toledo model C20 Coulometric Karl Fisher titrator with 99.999% UHP argon carrier gas (Matheson trigas). The mass measurements were done with the Mettler Toledo XS204 scale.

3.3 Density

Density measurements were taken with 2 mL pycnometers for all solutions, shown in Figure 18: 2 mL Pycnometers for Density MeasurementsFigure 18. The temperature was controlled by a Thermo Scientific Thermolyne oven inside of a glovebox atmosphere. The temperature was allowed to equilibrate in the solution and pycnometer for 2 hours at each setting to ensure uniform and complete heating. The mass was then measured with a DHAUS Adventurer Pro scale.

Figure 18: 2 mL Pycnometers for Density Measurements

3.4 Rheology

Viscosity in the shear regime was measured with a Brookfield DV2T viscometer and analyzed using Rheocalc T software. The spindle was a serial number SC4-27, designed for small samples. The sleeve was the matching pair for the spindle, SC4-

13RPY and had an incorporated temperature probe for accurate local temperature measurement and control, shown in Figure 19.

Figure 19: DV2T Programmable Rheometer and y-21 Spindle and Cup Pair with Temperature Probe

The temperature was controlled by a cooling and heating bath sleeve with a Brookfield temperature control unit pumping silicon oil instead of water mixtures to minimize chance of contamination of the glovebox atmosphere with water, shown in Figure 20.

Figure 20: Silicon Oil Jacket in Glovebox

3.5 NMR

3.5a Al27 NMR

Speciation of the chloroaluminum anions was verified with Al 27 NMR, all NMR spectra were obtained on a Bruker Avance-III 500 using standard conditions, and teflon sealed vacuum tubes shown in Figure 21. The probe background signal has been subtracted for some of the expansion figures. Chemical shifts referenced to 1M $Al(H_2O)_6$ $\delta = 0.00$ ppm at RT.

Figure 21: Vacuum Sealed NMR Tube with Ionic Liquid

3.5b Proton Pulse Field Gradient Spin Echo Nuclear Magnetic Resonance Spectroscopy

Diffusion of the cationic species was determined with PGSE NMR with a Bruker Avance-III 500 using standard conditions and sealed vacuum tubes. Self-diffusion coefficients of certain NMR active nuclei (and the molecules or anions they are a part of) can be measured with pulse field gradient spin echo nuclear magnetic resonance spectroscopy (PGSE) [131]. This technique uses gradient pulses to tag the nuclei with respect to their z position. The nuclei are free to diffuse for a short time and are flipped with a 180-degree pulse, then another gradient pulse is used to reorient the atoms. This second gradient pulse is the same as the first, and as the nuclei have been flipped 180 degrees should cancel the previous shifts. The more a nucleus moves with respect to the direction of the gradient, the more disparate the influence of the first and second gradient pulse is. Therefore, the nuclei are not rephased and contributes less to the echo signal. Changing either the time between pulses or the strength of the pulses and measuring the change in signal allows for measurement of the self-diffusion coefficients of the nuclei. Increasing times results in a lower signal, as the atoms have moved farther, or increasing the gradient pulse reduces the signal, as the impact of the distance travelled is stronger. The signal intensity follows the Stejskal-Tanner equation, Equation 2.

Equation 2: Stejskal-Tanner Equation

$$Signal = exp\left(-DG^2\delta^2\gamma^2\left(\Delta - \frac{\delta}{3}\right)\right)$$

Where δ and Δ are Constants of the NMR tool and pulse design (pulse width and separation, respectively), γ is the gyromagnetic ratio, D is the diffusion constant and G is the Gradient strength.

Plotting the gradient strength squared vs. the signal decay gives and exponential decay function, as the remaining components are constants of the instrument the diffusion constant can be determined.

3.6 Electrochemistry

Electrodes were prepared by initial polishing with 15 and 10 um diamond polish, but these were not necessary after the initial polished finish was achieved. The electrodes were then polished with Buehler Alumina micropolish at 1 um and 0.3 um particle sizes to a mirror finish shown in Figure 22.

Figure 22: BASi Electrodes and Alumina Polishing Slurry

The electrodes were always repolished with 0.3 um particles before each experiment set. After polishing, the electrodes were immersed in tap water under ultrasonic agitation (Branson 3510) to remove any particles that may have become imbedded in the surface. The electrodes were then rinsed with deionized water and dried with isopropanol (99.9% Sigma Aldrich) before vacuum drying and transfer into the glovebox. The electrochemical cell was a 100 mL Pyrex glass beaker with 1 mm

99.999% Al foil (Alfa Aesar) as a counter electrode around the circumference to maximize counter electrode area. The reference electrode was Al wire (Alfa Aesar, annealed, Puratronic®, 99.9995%) in 1.5:1 $AlCl_3$ EMImCl solution separated from the chemistry by a glass frit. The working electrode is 0.5 cm diameter polished glassy carbon disk in a Pine adjustable speed rotator (ASR) rotating disk electrode (RDE) configuration. All RDE measurements were done at temperature values of 30, 50 and 80C measured by a PTFE coated thermocouple immersed in solution, the setup is shown in Figure 23.

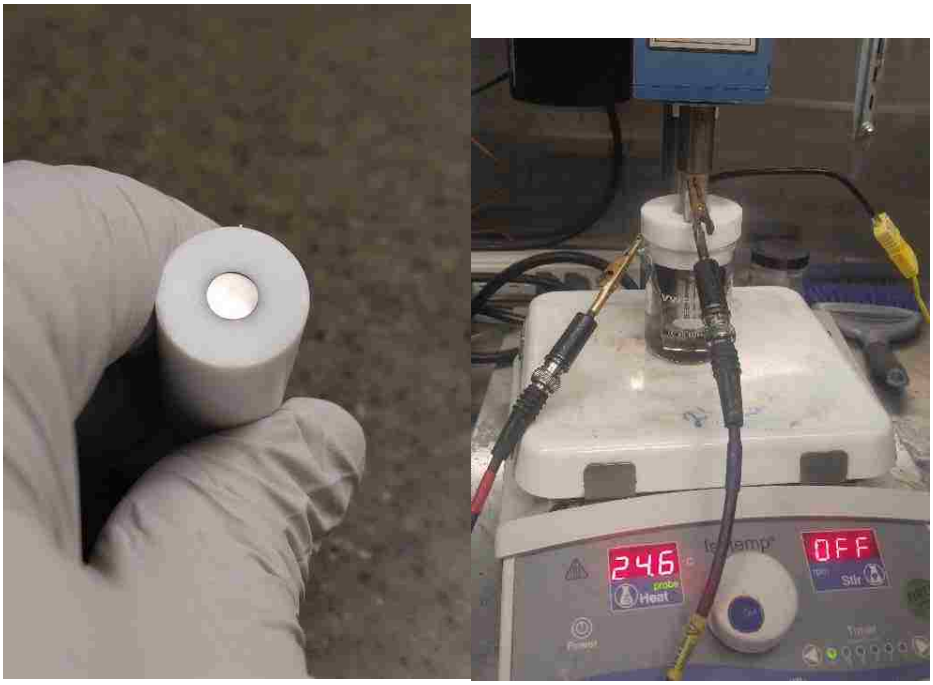

Figure 23: Rotating Disc Electrode and Electrochemical Cell

3.6a Cottrell Model

Cottrell scans were done in quiescent solutions (no rotation) at -400 mV mV overpotential vs. the Al reference (Quasi Reference Electrode (QRE) in BMImCl

solutions, 1.5:1 $AlCl_3$:EMImCl in EMIm Electrolytes). The Cottrell model implements a potential step and monitors the current response. The profile of this response vs. time indicates if the system is diffusion limited or not, and if so should follow the Cottrell equation, Equation 3.

Equation 3: Cottrell Equation

$$i = \frac{nFAc\sqrt{D}}{\sqrt{\pi t}}$$

The factors of this equation are constant except for current and time and plotting current vs. inverse square root time should produce a linear plot. The diffusion can be calculated from this slope.

3.6b Rotating Disc Electrode

The rotating disk electrode is used to determine the kinetic and diffusion limitations in an electrolyte through the control of convective parameters. Linear voltammetry is used in conjunction to measure the regime of the reduction process over changing kinetic rates. The model incorporates Fick's first law, stating that components in a solution move from areas of high concentration to areas of low concentration at a rate proportional to the concentration gradient as well as the velocity profile on the rotating disk, originally solved by Cochran and von Karman in 1921. These parameters are accumulated in the Levich model, following Equation 4.

Equation 4: Levich Equation

$$I_L = (.620)nFAD^{\frac{2}{3}}w^{\frac{1}{2}}v^{\frac{-1}{6}}C$$

Where I_L is the diffusion limited current, n is the number of electrons transferred during the reaction, F is faraday's constant, A is the electrode area, D is the diffusion constant, w is the rotation rate, *v* is the kinematic viscosity and C is the bulk solution concentration. Increasing the overpotential with linear voltammetry should increase the reaction kinetics so the system is diffusion limited, using the and Levich limited current at a rotation rate the diffusion rates can be calculated. RDE experiments were carried out at 50 to 1000 RPM rotation rates.

3.6c Nucleation Mode Tests

The nucleation mode is determined by the current response of the system after an overpotential has been applied. The maximum current is determined and the entire response is normalized (time and current) to this point. The data is then mapped to equations based on the system and the profile is considered instantaneous, where nucleation sites are generated instantly and the continual film growth perpetuates from those locales, or progressive where the nucleation sites continue to spawn.

3.7 Conductivity

Conductivity measurements were taken with a Yellow Scientific Instruments conductivity meter and YSI-3401 conductivity probe. 40 mL of solution was used in a 100 mL graduated cylinder (Figure 24) and the temperature was controlled through the use of heat tape on the exterior and omega PID controller.

Figure 24: Conductivity Meter and Probe

The solution temperature was measured from a thermocouple in the IL outside of the probe volume to ensure accurate measurements. Temperature measurements on the exterior of the glassware were unreliable and inconsistent.

3.8 Falling Ball Viscosity

The spheres were silver coated poly(methyl methacrylate) PMMA 1.44g/cc 63-75um (Cospheric) and chosen for their density and size, shown in Figure 25.

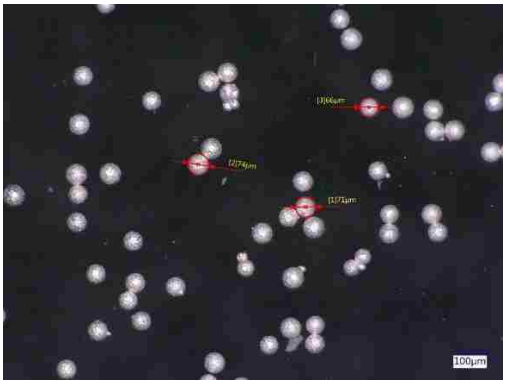

Figure 25:Cospheric Silver Coated PMMA Microspheres

To measure the viscosity in very low (zero) shear regimes requires a balance of drag forces from viscosity and the particle surface and body forces due to gravity so that the terminal velocity falls in the 10^{-6} - 10^{-4} Reynold's number regime.

The rectangular tubes used to hold the particles and electrolyte were fused quartz with openings that were 2x4 mm. The ends were capped with Viton tubing and additional seal was provided by vac seal epoxy. The ends of the tubes incorporated polyethylene swagelock valves to allow solution filling and closing of the vessel to the environment. The terminal velocity was determined by recording video of the falling spheres on a digital light microscope (Keyence VT-1000) with 200x magnification turned 90 degrees to horizontal, as shown in Figure 26.

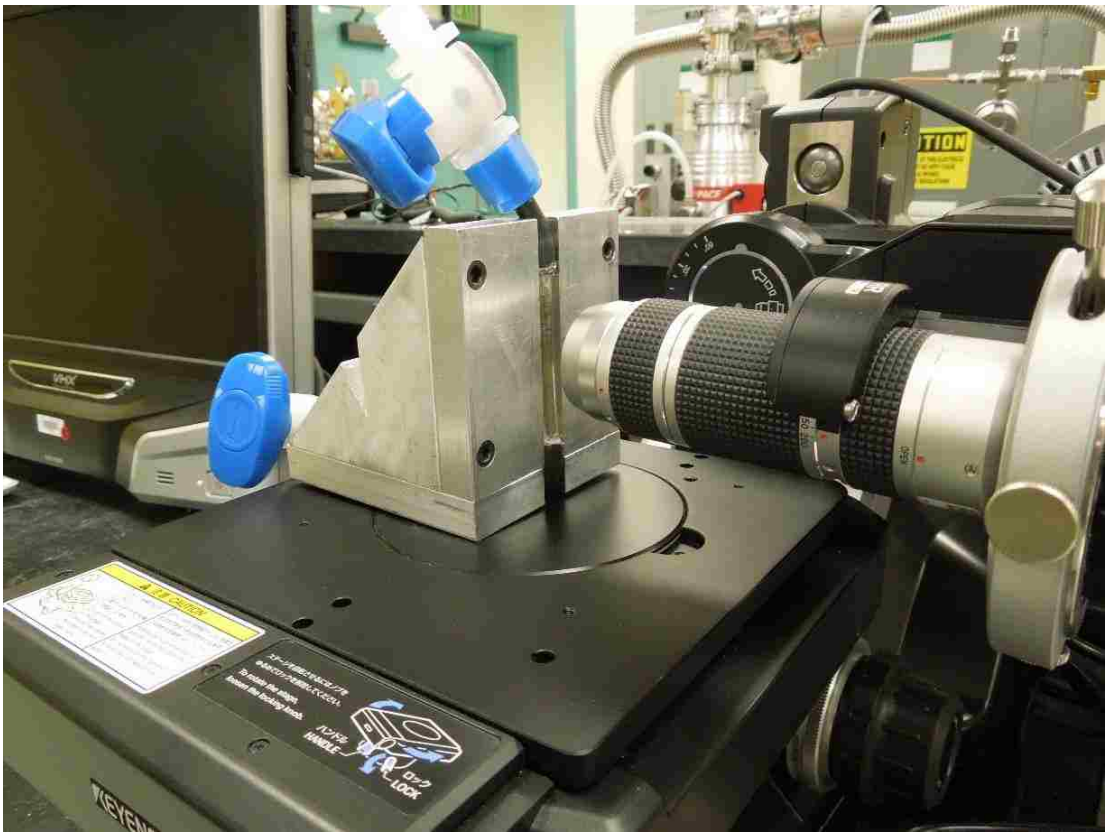

Figure 26: Rectangular Quartz Tube he Held at 90 Degrees for Microscope viewing of Falling Ball Experiments

Correlating the terminal velocity to the viscosity of solution was done with the stokes equation (Equation 5), and temperature was controlled with a Omega Benchtop thermocontroller and heat tape wrapped around the exterior.

Equation 5: Stokes Equation

$$V = \frac{2}{9}\frac{(\rho_p - \rho_f)}{\mu} g R^2$$

3.9 Scanning Electron Microscopy and X-ray Dispersive Spectroscopy

Surface and composition analysis of the deposited films were done with a Zeiss Supra 55VP field emission gun scanning electron microscope. EDS analysis was with a Bruker quad SDD (Silicon Drift Detector) using Bruker Esprit acquisition software.

3.10 Energy Release Differential Scanning Calorimetry

Thermal analysis was performed by Robert Knepper, using a TA Instruments DSC Q2000 differential scanning calorimeter. Between 5 and 8 mg samples were placed in copper pans for analysis. The DSC was operated at 40ºC/min between 50 and 725ºC for two cycles with 50 mL/min argon gas flow.

3.11 Transmission Electron Microscopy

Analysis of the particle and aluminum interactions were performed by Paul Kotula, with an FEI Company Titan G2 80-200 operated at 200kV and equipped with a high-brightness Schottky field emission source, spherical aberration corrector on the probe-forming optics, and four silicon-drift X-ray detectors with a combined solid angle of 0.7 sr.

3.12 Modelling

3.12a COMSOL

Fluid dynamics calculations in the reaction vessel were done with COMSOL Multiphysics software version 5.2. Laminar flow and particle tracing physics were solved for in 2 simulations in series. The Laminar flow in the reactor was calculated based on the power law viscosity profile determined by the rheology experiments in a stationary equilibrium study. The particle tracing physics was solved for in a time dependent study, at time 0, 100 particles were released at the inlet of the reactor and initial velocities determined by the fluid flow expression at the inlet. The simulation times were carried out for 5-20 seconds dependent on the flow rate in the reactor (slower flow rates necessitate longer simulation times).

3.12b Gaussian

Molecular dynamics simulations were performed with Gaussian 09 with the DFT B3PW91 Method and 6-311G basis set along with increased “tight” tolerances for volume calculations. The volume is determined by a 3 dimensional boundary wherein the electron density is greater than .001 electrons/Bohr^3. The given stokes radius is .5 A larger than the radius that corresponds to the calculated volume, as this is assumed to be more representative of radii correlated to diffusion.

Chapter 4: Aluminum Deposition - General

4.1 Aprotic Solvents

The aluminum matrix characteristics are central in controlling the codeposition process, therefore multiple electrolyte options were investigated, as they all have challenges and benefits. Electrolytes were assessed on ease of use, quality of deposit and cost of materials. Initial investigations in aprotic solvents were focused into the THF electrolyte and its aluminum complexing agents since this chemistry has a large presence in the literature [60-64], as well as other well-known battery electrolytes used in other electrochemical systems. Most solvents were very reactive with the aluminum salts and therefore not applicable for use; these include ethylene and propylene carbonates and DMSO, while others had poor solubility for the salts. Addition of salts were done slowly as the exothermic heating during the solvation of the Aluminum could cause breakdown in all the solvents. Complexing agents in these aprotic solvents were LiCl and $LiAlH_4$, where the lithium aluminum hydride was the more effective in improving the amount of reducible aluminum species in solution and increasing deposition rates. Electrodeposition results were smooth and adherent under certain conditions but the high vapor pressure and difficulty of use lead to the ultimate decision against their use. Some solutions are shown in Figure 27, most of the typical battery solvents have poor solubility towards the precursors and complexing agents and these are gray or opaque from undissolved remaining components.

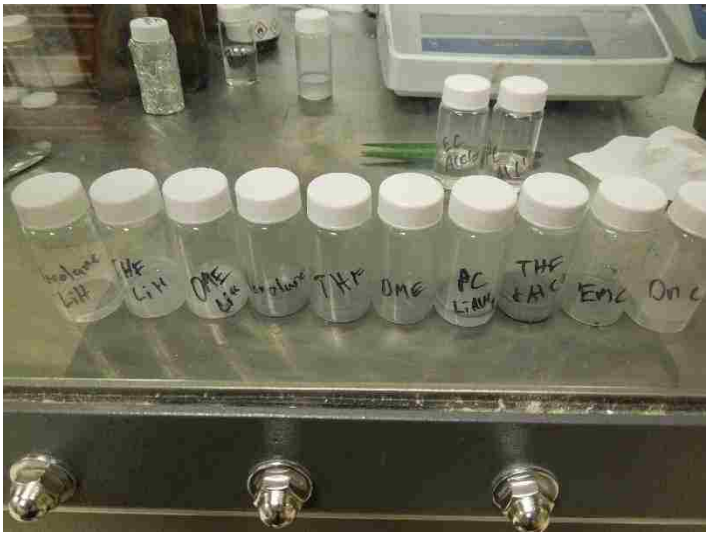

Figure 27: Aprotic Electrolytes with Al Precursors

Ethylene carbonate was initially promising as it showed high aluminum chloride solubility and the reduction of melting point decreased the melting point to well below room temperature while the vapor pressure was still low. The solutions did not show any aluminum reduction on a copper cathode, which is presumed to be because the solution does not produce an electroactive complex. To prove this, cyclic voltammetry was used on the solution. Scans showed a slight peak in current at -1.6 V vs. Ag (scan rate 5 mV/s), Figure 28.

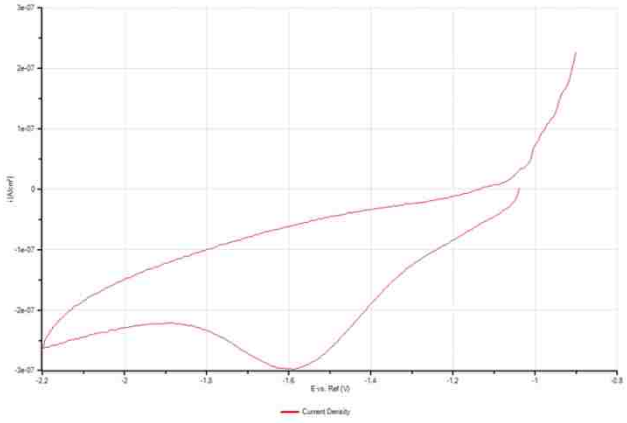

Figure 28: Reduction Peak in EC $AlCl_3$ at -1.6 V vs. Ag (5 mV/s)

Even with $LiAlH_4$ additions to the ethylene carbonate electrolyte, voltammetric testing for extended periods of time at -1.5 V showed very little current and no evidence of aluminum reduction, Figure 29.

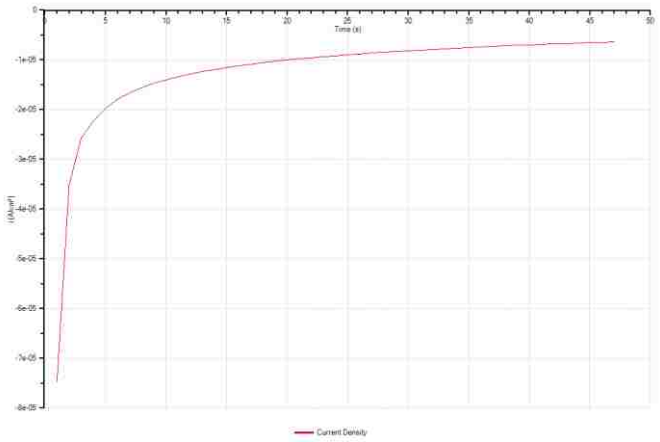

Figure 29: Low Sustained Current In EC $AlCl_3$ at -1.5 V vs. Al

The negligible current and absence of noticeable aluminum deposition lead to the conclusion that EC would not be a good solvent for aluminum plating. It was unclear whether the EC itself hindered the process of if the aluminum precursors were not forming reducible aluminum complexes.

4.2 Aromatic Solvents

The next set of solutions investigated were toluene and benzene aromatics. The aromatics are lower vapor pressure, lower flammability and easier to handle than the ether based aprotic solvents. The aromatic solvents do not have solubility towards chloroaluminum salts so larger anions were used. The bromo aluminum salts had high solubility and went into solution quickly, with no noticeable exothermic reaction. These salts turned the solution yellow and showed no activity until addition agents were again

employed, these solutions are seen in Figure 30. This further reiterates the importance of forming reducible complexes with additions of a secondary component.

Figure 30: Aromatic solvents with $AlBr_3$ in Solution

The addition agents used were other bromide salts which complex with the $AlBr_3$ in solution, namely potassium bromide which also had good solubility in the aromatic solvents. These solutions were much easier to work with because of their lower vapor pressures but the deposit was rough and uneven, and plating rates were low even with salts added to promote electroactive complexes. Dichlorobenzene was a promising aromatic solvent in principle, as it should have increased chemical and electrochemical stability and higher solubility based on its higher polarity and but it resulted in a very poor solvent system, likely arising from the high dielectric constant increasing its interaction with the reducible aluminum salts.

4.3 Ionic Liquids General

The last set of options that were investigated were ionic liquids. There are multiple cation and anion choices that have been used in the literature, and the focus was directed to the chloroaluminates as they promote clean, facile electrodeposition of aluminum. These solutions, like other aluminum electrolytes require inert environments due to the reactive nature of the precursors and the deposited aluminum. Some air and water stable ionic liquids that incorporate highly fluorinated anions were tested, but after aluminum additions they are still strongly and irreversibly affected by air and water contamination. These hydrophobic solutions are also significantly more expensive than the first generation chloroaluminate ILs. The anion was chosen to be the standard chloroaluminum reducible complex the next focus was on cation choices as discussed in chapter 1. TMPACl received interest since its cost is significantly lower than the other ILs but the aluminum deposit was always rough, dark and had poor adhesion. Dialkylimidazolium cations are very chemically and electrochemically stable, and are on the lower end of cost. The BMImCl solution's high viscosity was mostly due to the Van der Waal forces on the alkane chains and this limits the diffusion and mobility of all components in the solution. EMImCl solutions are lower viscosity since they have shorter alkane chains and lower van der Waals attractions. To reduce the viscosity of BMImCl solutions, dilution agents are added, and this is required to achieve smooth electrodeposits. EMImCl $AlCl_3$ solutions deposit aluminum readily in neat solutions, but BMImCl is less expensive and dilutions could also reduce cost, these electrolytes are discussed in detail in sections 6 and 5 respectively. The other ionic liquids that were investigated were ruled out for either cost or incompatibility with aluminum precursors.

They were however useful in testing chemical methods as they are more air and water stable than the ILs containing aluminum species.

4.3a Ionic Liquid Water Content Reduction

Multiple cleaning methods were tested for their ability to reduce water content with Karl Fischer titrations. These were baking, electrochemical cleaning and molecular sieves. EMIm dicyanimide was used for this testing as it does not react with air and water like aluminum ILs. It was investigated as an electrolyte because it has one of the highest conductivities of commercially available ILs but it is highly reactive with aluminum complexes and cannot be used for deposition. Ionic liqudis with TFSA hydrophobic anions show the lowest water content when tested with Karl-Fisher. Standard, as received EMIm DCA was the control sample and has roughly 370 ppm water. The water content is reduced by baking at 90-150C, cyclic voltammetric cleaning and 3A molecular sieves, in order from least to most effective, the resulting data is shown in Figure 31.

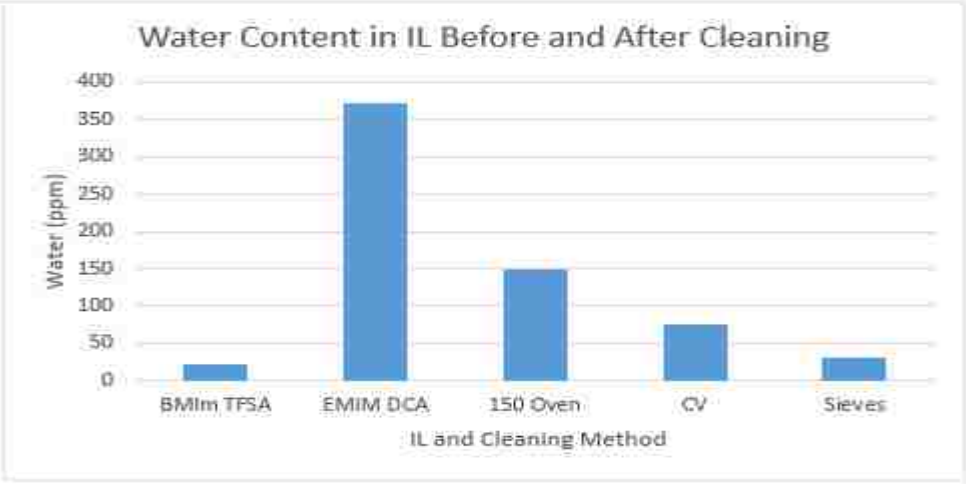

Figure 31: Water Content of ILs and Cleaning Methods

An example of the shift with electrochemical purification is shown in Figure 32. The scans are 100 mV/s and room temperature in a glove box atmosphere.

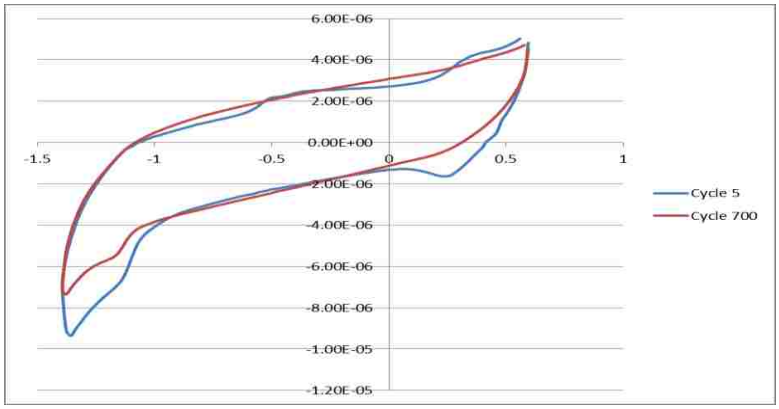

Figure 32: Cyclic Voltammetry on EMIm DCA IL for Impurity Removal (100 mV/s, RT), changes between the two are attributed to removal of impurities.

The softening of peaks indicates decreased impurity content, the peaks negative of -1 V may be due to electrolyte breakdown, but this solution was not used in further testing so these reductions were not investigated at this time. The chloroaluminate imidazolium ILs showed the most promise for aluminum deposition, with high aluminum salt content, activity, and stability and were the focus of further investigation. The first of which is BMImCl $AlCl_3$ mixtures for their low cost and high chemical stability.

Chapter 5: Butyl Methyl Imidazolium $AlCl_3$ Ionic Liquids and Co-Solvents

BMImCl $AlCl_3$ electrolytes deposit aluminum very poorly as neat solutions but improve greatly with additions of co-solvents and dilution agents that reduce the viscosity. The diluents used were toluene and ortho-dichlorobenzene (DCB). The toluene was lower viscosity than the DCB (.7 cp vs 1.3 cp) but the DCB had much lower vapor pressure and was more chemically stable. The slight instability of toluene dilutions is known and the halide substituents deactivate the aromatic ring [85]. Ethylene carbonate was also tested as it has high miscibility and applicable electrochemical windows. It was later determined that the EC is not chemically stable with the aluminum chloride and results in a non-reducible complex. Conductivity and other experiments may not correlate well to deposition results if the assumed speciation is not accurate and the reducible species differ from the expected. Recall that solutions must be Lewis acidic (greater than 1:1 $AlCl_3$ ratio) to generate electroactive species, $Al_2Cl_7^-$. Because of this, understanding the speciation in a given IL is important and was investigated with Al27 NMR.

5.1 NMR Speciation Analysis

The bonding environment of the aluminum is consistently tetrahedral coordination to chlorine and always results in a 103 ppm downshift. The $AlCl_4^-$ species is very symmetric and therefore gives a very sharp NMR spectrum. As the electrolyte is made more Lewis acidic by adding $AlCl_3$, the composition shifts toward more $Al_2Cl_7^-$ species until all of the Al is in this state. The $Al_2Cl_7^-$ is still tetrahedrally coordinated with respect to Al and Cl, but the asymmetry of the chlorine sharing leads to peak broadening.

Speciation can be determined in the neat IL by comparing the FWHM of the Al27 NMR peaks. The equation is straightforward using constants of FWHM signals of prepared 1:1 and 1:2 Cl: $AlCl_3$ (A and C, respectively), shown as Equation 6.

Equation 6: Aluminum Speciation Based on NMR Equation

$$p_A = \frac{\mathrm{FWHM}(sample) - \mathrm{FWHM}(C)}{\mathrm{FWHM}(A) - \mathrm{FWHM}(C)}$$

NMR results match well to expected values and the Al speciation does match the stoichiometric balance consisting of $Al_2Cl_7^-$ and $AlCl_4^-$. NMR peaks of progressively higher $AlCl_3$ concentration solutions are shown in Figure 33.

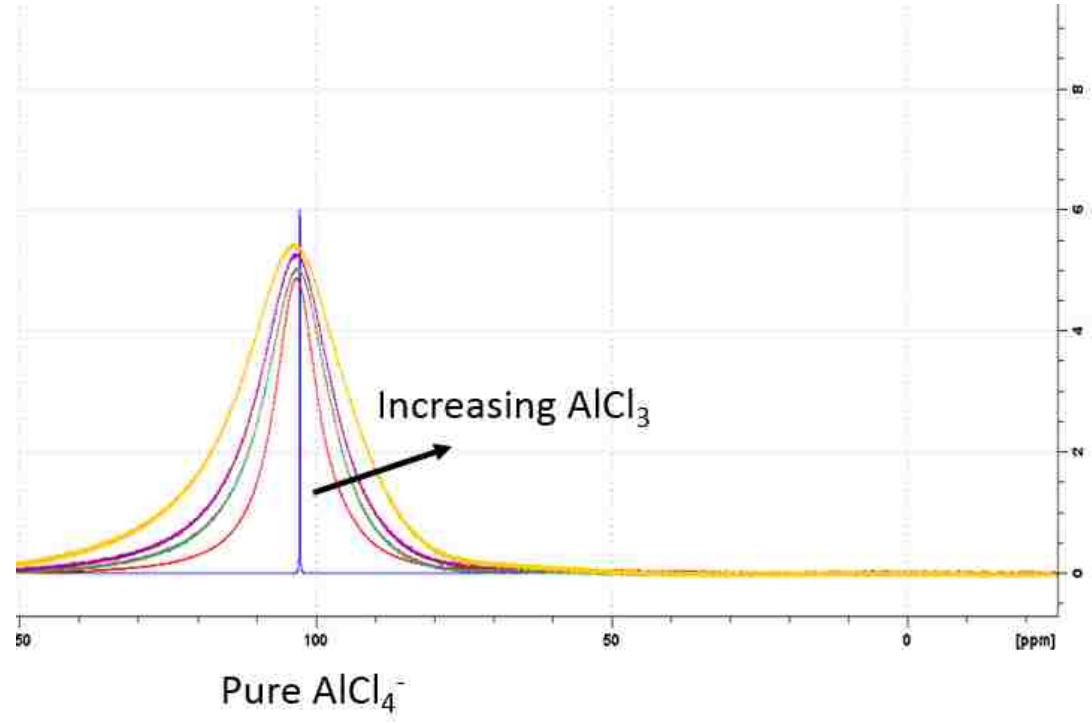

Figure 33: Al27 NMR of the Chloroaluminate IL at varying $AlCl_3$ Concentrations

Temperature variation shows little effect on the speciation, as shown in Figure 34. The FWHM increase with temperature for all solutions, but the end point FWHMs shift

accordingly, so the formula can still be used to determine speciation as long as the end points are corrected for.

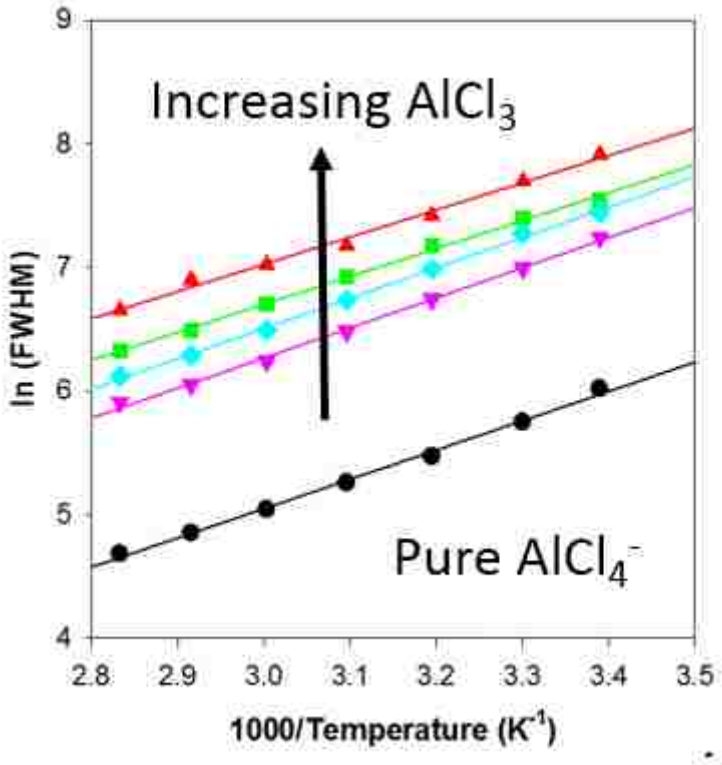

Figure 34: Temperature Variation of FWHM in Al27 NMR at Varying $AlCl_3$ Concentrations

Additions of aromatics may cause changes in the speciation, Abbott et al. show that the heavily acidic ionic liquids are not affected but the intermediate mixes may be [87]. Solutions tested with dilutions were restricted to the most acidic 2:1 $AlCl_3$:BMImCl chemistries, as these had the highest concentrations of electroactive species.

Since there is only one peak in the Al27 NMR, the data indicates that there are only tertrahedrally coordinated aluminum species present, presumably only $Al_2Cl_7^-$ and $AlCl_4^-$ anions and they are in equilibrium at the stoichiometric values of free chlorine. This allows easy control of the concentration of each species by modifying the $AlCl_3$ to

Cl ratio. This control is crucial in determining the amount of electroactive species that are present for electrochemical measurements.

5.2 Electrochemical Testing – Cyclic Voltammetry

BMImCl $AlCl_3$ will deposit smooth coatings with additions of dilutions and cyclic voltammetry was tested with neat and co-solvent diluted solutions to get a general idea of interactions. Three scans are shown in Figure 35.

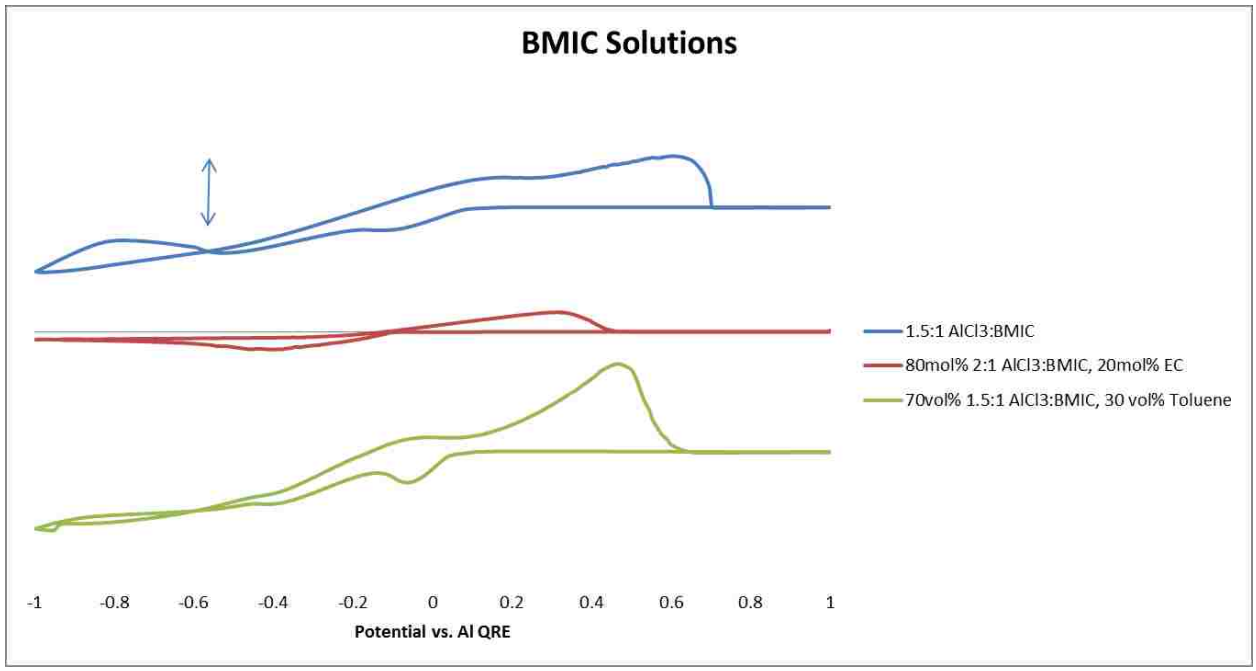

Figure 35: Cyclic Voltammetry in BMImCl $AlCl_3$ ILs with Co-solvent Additions (5 mV/s, RT)

Additions of toluene to the IL showed similar trends to the neat IL, with EC additions suppressed the electrochemical response significantly. The solvents change the ionic interactions of the IL and modify the diffusion properties.

5.3 Deposition Testing and Results

The best depositions from the initial testing were seen to be reduction potentials between -200 and -600 mV vs. Al quasi reference electrode and with dilutions. The toluene solutions were tested from 20% - 60% and DCB was used for higher dilutions because it had higher miscibility with the IL. Some deposits on copper with their respective conditions are shown in Figure 36, and more detailed SEM and EDS data is shown in Appendix C.

Figure 36: Electrodeposition of Aluminum on Copper from Various Electrolyte baths

It is very common in electrodeposition that edges and corners are exposed to higher current densities than the average over the electrode. This leads to dendritic or poor growth characteristics in these areas. It is beneficial to mask these areas and ensure that the whole of the cathode experiences similar polarization. These effects are apparent

when using the ILs to plate Al [11], but are suppressed when using dichlorobenzene as a co-solvent over toluene as shown Figure 37 for comparison. This may be due to the higher dielectric properties of the dichlorobenzene.

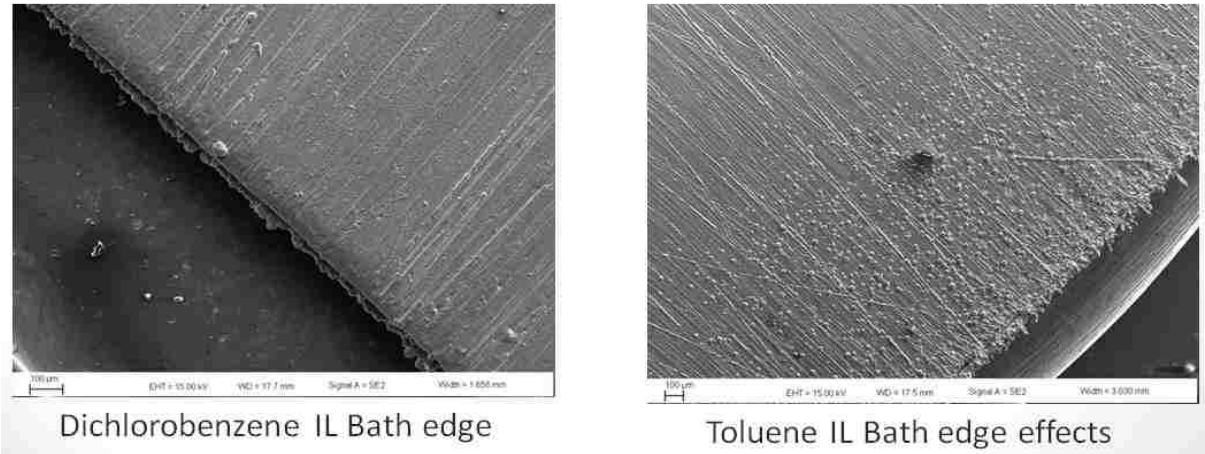

Figure 37: Edge Effects in Diluted Ionic Liquid Electrolytes (-600 mV vs. Al QRE)

A comparison of the properties such as cost and deposition quality are shown in Table 1. Of the solutions tested 3:1:2 Tol:BMImCl:$AlCl_3$ solutions and 11:1:2 DCB:BMImCl:$AlCl_3$ solutions and -600 mV overpotential were the highest quality deposits. Increasing dilution percentages decreases plating rates while also decreasing electrolyte cost, as the IL is the more expensive component.

$AlCl_3$	BMImCl	Toluene	DCB	mV (-) vs. Al QRE	Appearance	Purity	Cost ($/L)
2	1			600	Acceptable	Acceptable	1468
2	1	1		600	Good	Medium	1120
2	1	3		600	Best	High	768
2	1	6.8		500	Good	Medium	492
2	1	6.8		1000	Poor	Low	492
2	1	6.8		1500	Black powdery	Low	492
2	1		11	600	Best	High	384
2	1		16	600	Not Complete	High	312

Table 1: Comparison of BMImCl and Co-Solvent Electrolytes Deposition Quality

In an $Al_2Cl_7^-$ rich electrolyte the anode is significantly affected by polarization and mass transfer limitations. It's well known that when designing an electrolyte plating bath, the anode must have sufficient area and reactants to undergo oxidation equivalent to the rate desired at the cathode. Shifting the composition of the electrolyte to contain more $AlCl_4^-$ species may be useful to improve the anodic reaction efficiency. However, in these studies the 2:1 electrolyte was still used and the anode size was the only correction implemented. The dilution and overpotential options were determined in this preliminary study and investigating trends that determine these qualities allows for optimization of deposition quality and rate.

5.4 Optimization of Deposition with Dilutions

The viable electrolyte systems were down selected and investigated with electrochemical testing to determine optimal conditions, improving aluminum deposition rate and morphology. Dendritic growth is very common in the neat IL, indicating diffusion limitations. Investigating the mobility of the reducible species and improving its net diffusion rates will improve the deposition quality.

5.4a Diffusion vs. Dilution – Cottrell

The diffusion rate of the reducible species was determined using chronoamperommetry, with and without dilutions of aromatic co-solvents. The diffusion rate model (Cottrell) is based on reduction of an electroactive species, its depletion and the development of the diffusion layer. A representative plot of the data derived from

room temperature chronoamperommetry of 50% toluene diluted 2:1 $AlCl_3$:BMImCl solution is shown in Figure 38. The current response is plotted vs. the inverse of the square root of time.

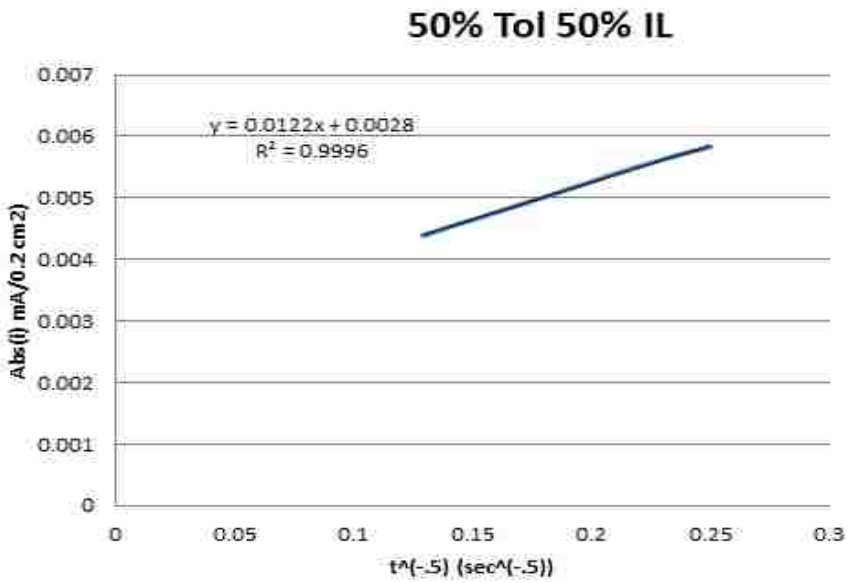

Figure 38: Cottrell Plot from chronoamperommetry, room temperature 2:1 AlCl3:BMImCl IL and 50% toluene dilution

The linear response of data plotted this way indicates a diffusion layer growth and diffusion limitations. The diffusion constants are calculated from the slope of the line. The diffusion rates in neat solutions and dilutions of toluene and DCB are shown in Figure 39. As expected, the diffusivity increases consistently with increasing co-solvent addition.

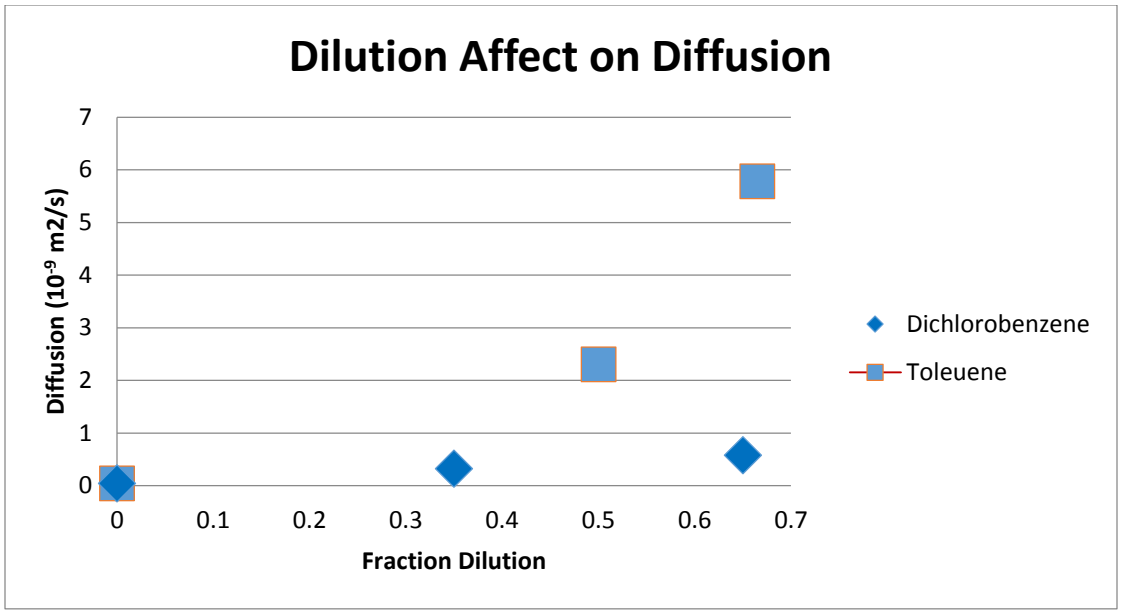

Figure 39: Diffusion of Al2Cl7- in 2:1 AlCl3:BMImCl IL and Dilutions with Aromatic Co-Solvents

Reddy et al. reported 2 x 10 -11 m2/s in similar IL at 90°C [132]. The dichlorobenzene dilutions show significant increases in diffusivity with dilution but the toluene increases are much larger. This is likely due to the toluene having lower viscosity as well as significantly lower dielectric constant, where the higher interaction between the salts and DCB solvent retard the transport capabilities.

5.4b: Conductivity vs. Dilution, Optimal Conditions

The ionic conductivity is representative of both the trends of the salt species concentration its mobility, and mobility is heavily influenced by viscosity. The conductivity was tabulated over the dilution range and measurements are shown in Figure 40, comparing the increased conductivity seen over neat solutions and the increase in conductivity seen in toluene dilutions over DCB dilutions.

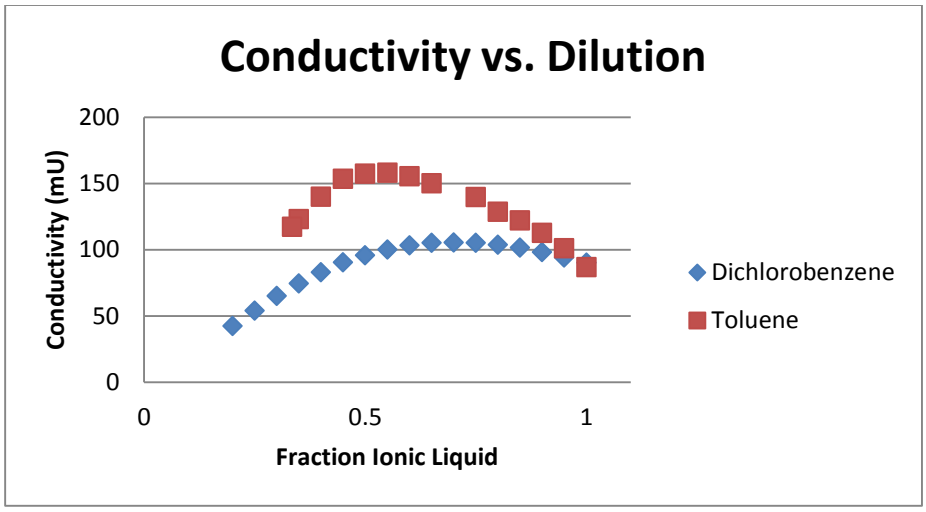

Figure 40: Plot of Conductivity vs. DCB and Toluene Dilutions in BMImCl ILs

The dilution specific properties are shown in Figure 41 and Figure 42. Comparing the ionic concentration along with diffusivity measurements obtained from Cottrell measurements with their influence on the solution conductivity shows expected trends. There is a significant increase in the diffusion rate but the concentration is reduced, leading to a maximum in the conductivity curve.

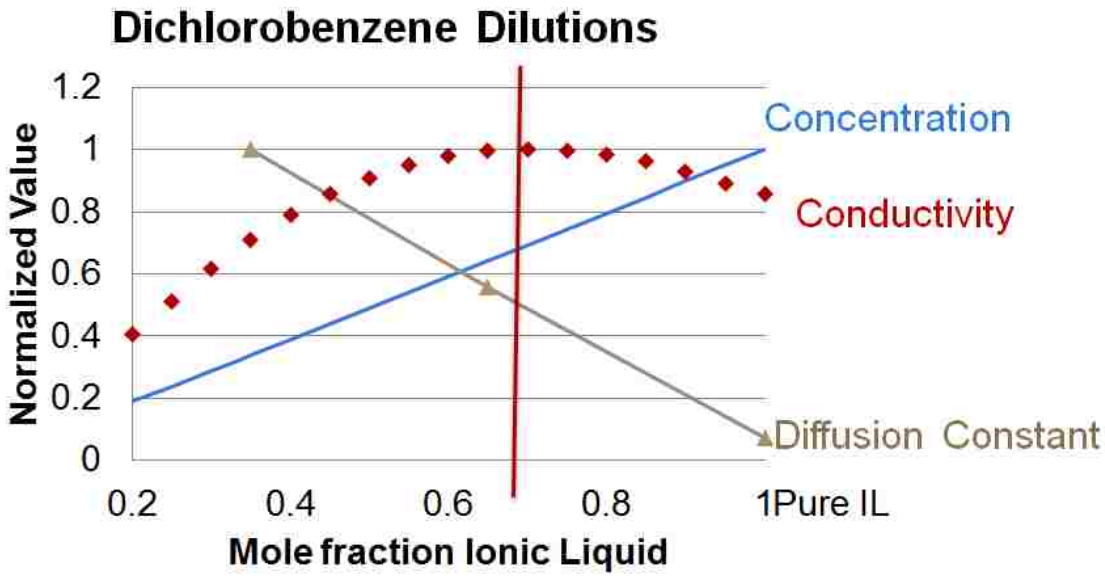

Figure 41: Dichlorobenzene Dilution, Conductivity and Diffusion Constants

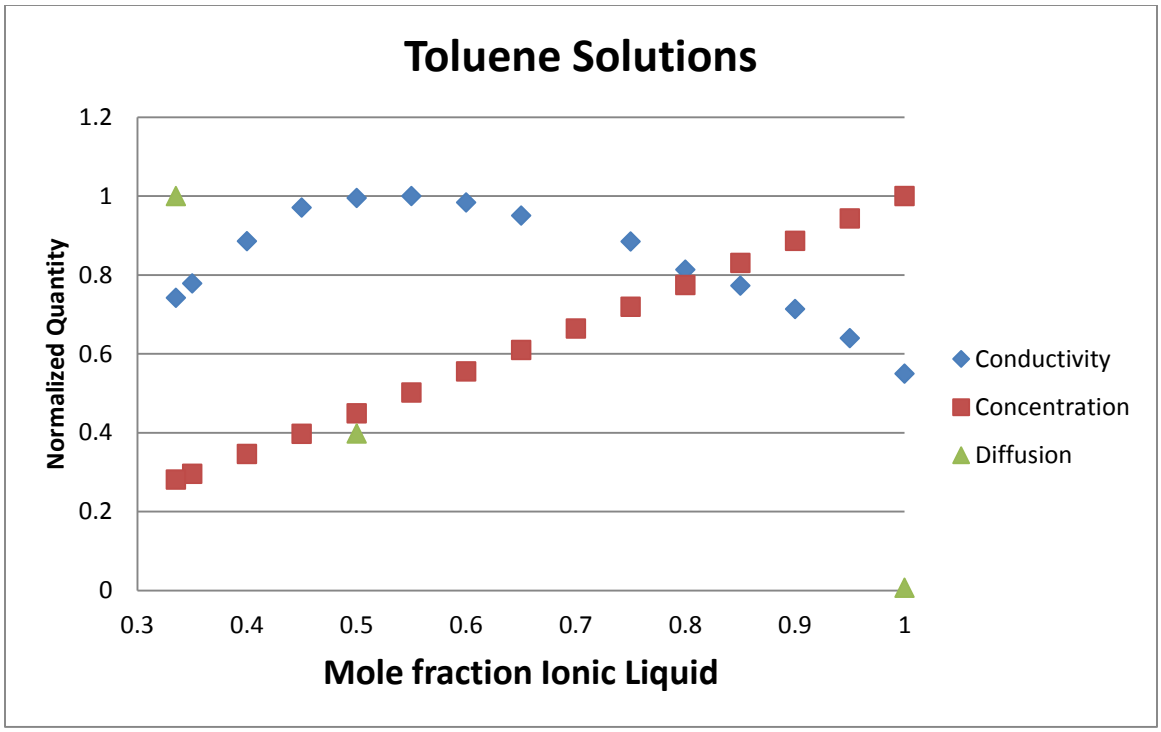

Figure 42: Toluene Dilution, Conductivity and Diffusion Constants

The ionic concentrations change linearly with decreases of mole fraction of the IL, and the larger increase in mobility seen in toluene dilutions shifts the maximum conductivity to lower concentrations than the DCB dilutions. The maximum conductivity seen at 50% dilution in the toluene chemistry aligns with the best observed deposition characteristics that were seen in previous testing, verifying the conductivity is a good indicator of deposition quality and reiterating the 3:2:1 Toluene: $AlCl_3$:BMImCl chemistry is a top choice for high rate and low diffusion limitation regimes.

5.5 Room Temperature Kinetics – Rotating Disk Electrode

A Pine model AFR fitted with a removable glassy carbon electrode tip allowed deposits to be studied by SEM/EDS without having to remove them from the substrate.

The glassy carbon is polished as described previously ensuring consistent and clean analysis. The rate of the reaction is controlled by the diffusion of reactants to the electrode surface and the reaction overpotential. The diffusion constants and reaction kinetics can be determined by controlling the diffusion distances with the flow parameters at the electrode surface and the reaction kinetics with potential. Since the polarization of the anode and cathode are so significant a step pulse was implemented. This allows time for equilibrium polarization to be achieved in between each measurement and removes the polarization factor. The IL double and diffusion layers take much longer to develop and have a greater impact on measurements than in other electrolyte systems, and slow scan rates lead to significant deposition on the electrode that changes the surface area and measured current. The step pulse, including a stripping and rest period between each measurement was used as a precautionary measure. Results of the linear voltammertic scans at various rotation rates on the rotating disc electrode are shown in Figure 43.

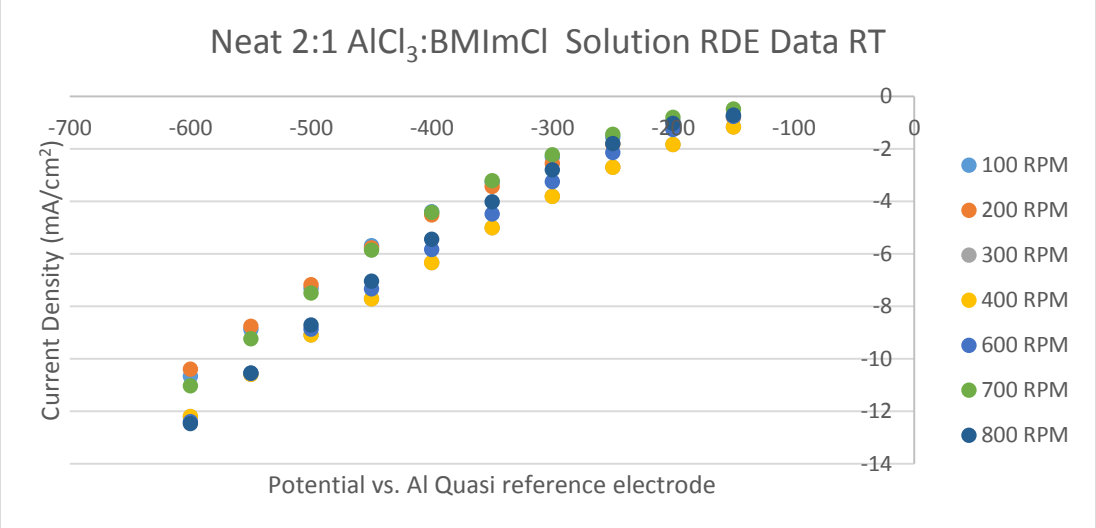

Figure 43: Linear Voltammetry on RDE in Neat BMImCl ILs

The rotation rate had little effect on the deposition rate, and no conditions tested reached the Levich diffusion limited regime in the range of the tests. It was clear these systems are predominately kinetically limited. Recall, previous work on the chronoamperometry indicated that these systems were diffusion limited, not kinetically limited. Clearly, different tests were giving inconsistent results. The kinetic limitation of this reaction at room temperature were lower than desired and were investigated specifically

5.6 Tafel Model and Low Charge Transfer Kinetics at Room Temperature

To investigate the kinetics specifically, the butler-volmer and tafel equations can be used and the exchange current density will be another indication of limiting deposition rates. The Tafel equation is shown in Equation 7.

Equation 7: Tafel Equation

$$\eta = A * \ln\left(\frac{i}{i_0}\right)$$

The Tafel model investigates charge transfer rate by extrapolating overpotential vs. Log(current) plot to zero overpotential. The electrochemical scan used for this measurement is shown in Figure 44 and the plot used to calculate the exchange current density is shown with it Figure 45.

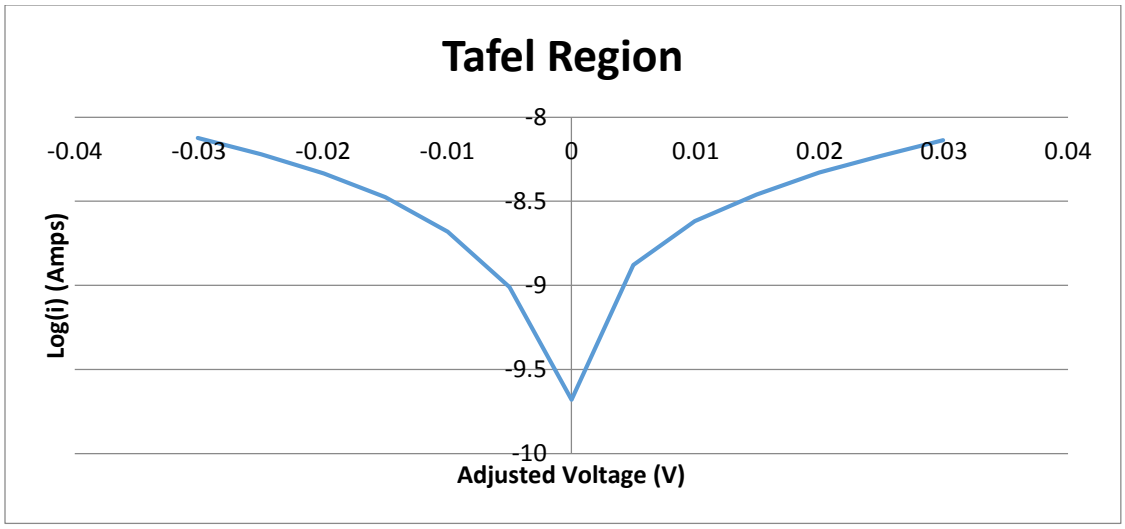

Figure 44: Tafel Linear Voltammetric Scan 2:1 $AlCl_3$:BMImCl, Room Temp, 2 mV/s

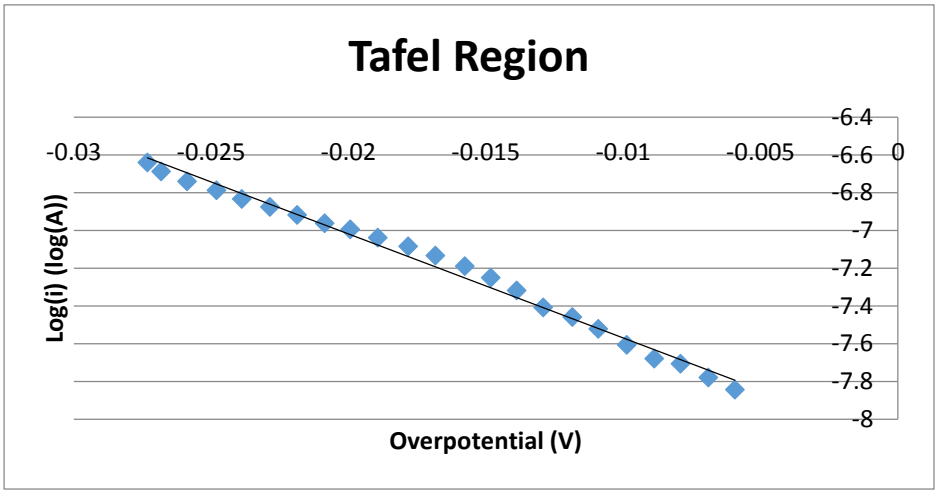

Figure 45: Log Current vs. Overpotential

The Al Red/Ox reaction is symmetric and reversible and the charge transfer was indeed slow, with exchange current density on the order of $8x10^{-9}$ A/cm^2. This indication of slow kinetics demonstrates why, even though the diffusion is considered slow and concentrations were high, the solution was still influenced by kinetic limitations. The relationship of reaction kinetics and reactant diffusion is a strong determination of the nucleation and growth modes of the electrodeposition mode and the interaction was

investigated specifically and detail can be seen in Appendix A. It has been reported that the nucleation model in ILs is instantaneous[86, 93], likely due to the low diffusion rates and possible effects of the aluminum precursor being negatively charged. The literature tests are generally at several hundred mV of overpotential so testing lower values was performed, as the decreased kinetic rate may have shifted the regime toward more progressive modes. This was not the case and all conditions tested were showed instantaneous growth modes.

5.7 BMImCl and Dilutions Conclusion

The data fit certain trends well but shows discrepancies when comparing between the kinetic, dynamic and different dilution conditions, as diffusion or kinetic limitations dominate separately depending on the concentration and agitation. There are many other factors that come into play when using ionic liquids, such as high viscosity and the precursors being strongly interacting with other components in the solvent. Rotating disk electrodes showed the $Al_2Cl_7^-$ reduction at room temperature has a kinetic current limit of ~10 mA/cm^2, although the reaction is commonly diffusion limited when under quiescent conditions.

The neat BMImCl chemistry and dilutions were either difficult to plate with or reached kinetic limitations easily. Adding dilution agents greatly increased the plating quality but the vapor pressure and possible chemical reactions argue against their use in increased temperature conditions. Competing aluminum deposition baths are consistently run at much higher temperatures to reach higher deposition rates, and $DMSO_2$

chemistries reach 200 mA/cm^2 at 130˚ C [133]. Controlling the matrix growth rate is crucial in the codeposition process, and options to increase the rates are necessary. It was evident there are kinetic limitations at room temperature operation and investigating increased operating temperatures would lead to more options for optimization. The diluted BMImCl bath is ideal for low temperatures but according to literature, the pure EMImCl chemistry runs better at increased temperatures and without dilutions [134]. The increased temperatures that are needed to increase kinetics were investigated directly without the added variable of dilutions. Understanding the neat solution properties will improve its direct use and the transition to a diluted system if needed.

Chapter 6: Increasing Kinetics with Elevated Temperature – Ethyl Methyl Imidazolium Cations

The focus for this chapter is on the kinetics and diffusion of EMImCl electrolytes at varying composition, temperature, overpotential and electrolyte flow. There are many optimizations that are required to accomplish a compact nanostructured electrodeposited film. As will be shown temperature has significant effects on both the deposition kinetics and mass transport properties, with differing shifts in each. The electrolyte composition changes the concentration of reducible species, modifying the reaction properties on the anode and cathode. The viscosity and solution flow is critical in both the particle transport and mass transport. Balancing particle arrival rate with aluminum matrix growth to achieve the needed solid ratio requires knowledge of the reduction kinetics and diffusion as well as the flow properties of the solution around the electrode.

6.1 Density

The basic physical properties are required for solving equations in more complex experiments. The density was measured and the plot of density vs composition and temperature is shown in Figure 46.

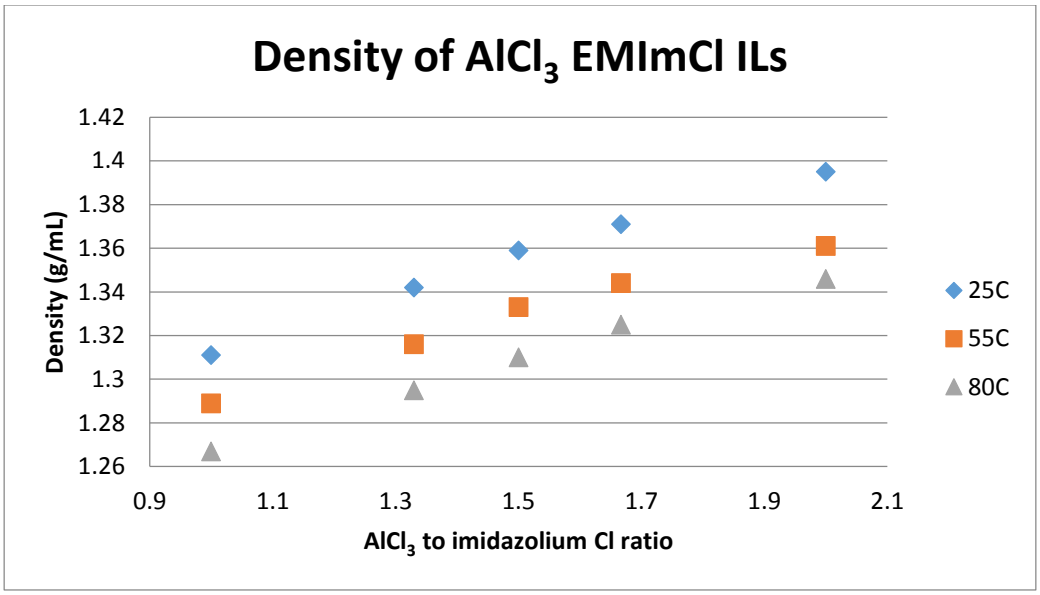

Figure 46: EMImCl $AlCl_3$ Ionic Liquid Densities

The density of ionic liquids increases linearly with additions of the $AlCl_3$ and decreases with temperature. The composition of this ionic liquid is very closely based on the stoichiometric ratio of the salt solution as was the case for the BMIC solutions, and was validated again with Al27 NMR in the same method as the BMImCl solutions, to confirm there was not a change when the cations are switched.

Combining the speciation and density gives the ionic density, and the molecular weights of the components are used to determine the ionic concentration. The mass density increases as the amount of $AlCl_3$ in solution increases but the ionic density is reduced, since the lower mass $AlCl_4^-$ is being converted to the larger $Al_2Cl_7^-$ species. The decrease in concentration is linear with composition, and the density decreases with increasing temperature consistently in all electrolyte compositions as shown in Figure 47.

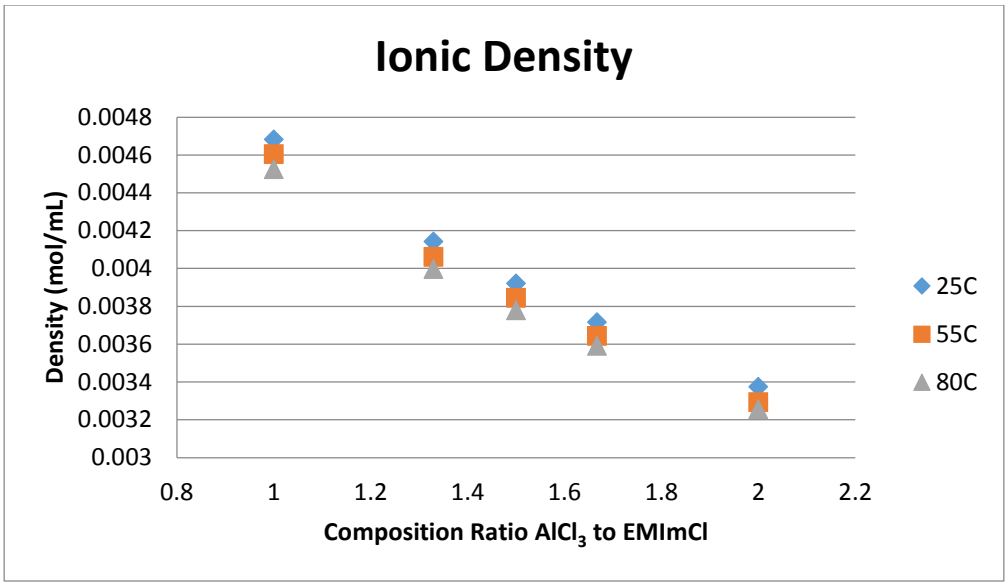

Figure 47: EMImCl $AlCl_3$ Ionic Liquid Ionic Densities

6.2 Diffusion – Cottrell

With the concentrations known, the diffusion of the reducible species was investigated with the Cottrell method. The Cottrell data for the 5 to 3 electrolyte at 50˚ C is shown below, and all other compositions and temperatures were measured using the same method. The analysis is the same as run previously in chapter 5.3 but is shown again here with the different electrolyte. The study analysis begins with the current response to a step to -400 mV vs. Al (1.5:1 $AlCl_3$:EMImCl) reference electrode to initiate the development of the diffusion layer, shown in Figure 48.

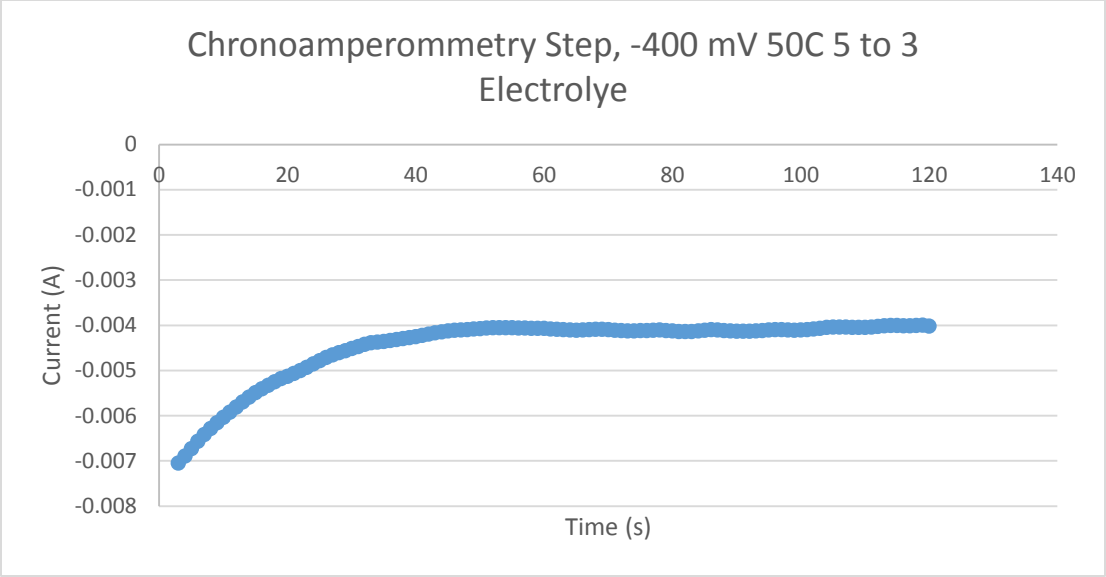

Figure 48: Experimental data for Cottrell diffusion measurements

The current response of the system is then plotted vs. the inverse of the square root of time, and the linear region is extracted, Figure 49. The slope of this line is used to determine the diffusion rate constant.

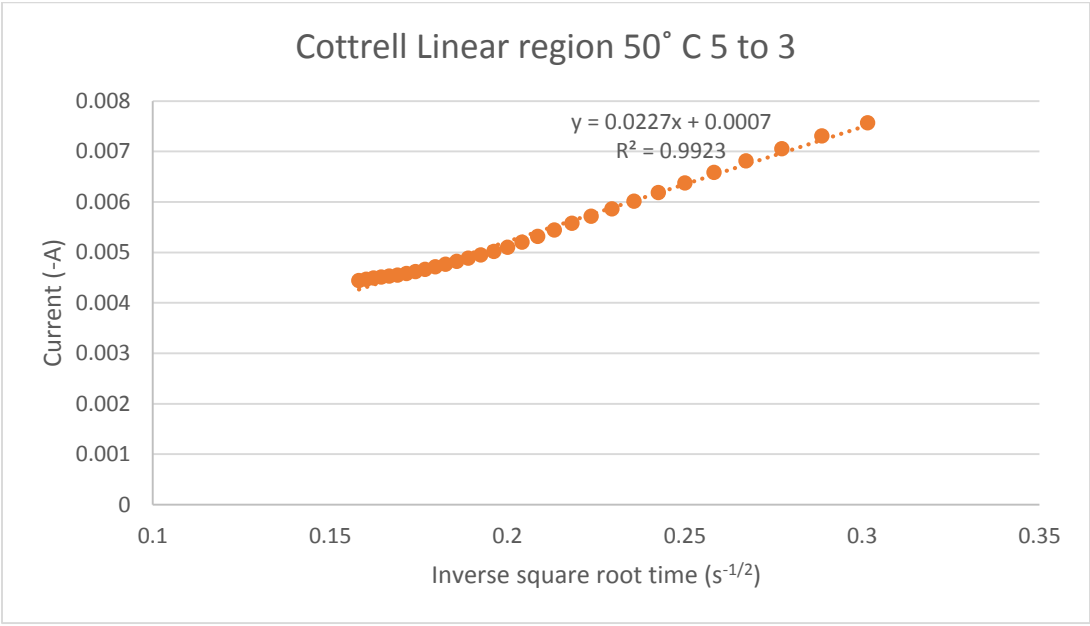

Figure 49: Cottrell plot for diffusion measurement

The mobility of the reducible species shown by the Cottrell equation demonstrates an increasing trend in mobility with increasing $AlCl_3$ concentration. There is also a significant increase in mobility with temperature as expected. The data is shown in Figure 50.

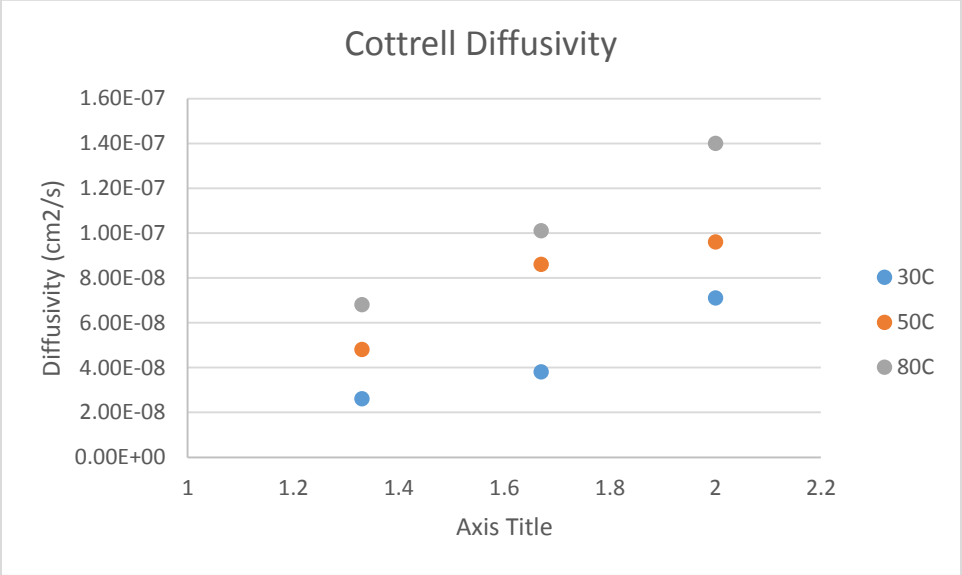

Figure 50: All Cottrell Data EMImCl:$AlCl_3$ Ionic Liquid Electrolyte

All of the electrolyte compositions at all temperatures tested show Cottrell dependent diffusion layer growth

6.3 Aluminum Reduction in Dynamic Conditions

The Levich equation requires information on the electrolyte viscosity and this was measured at varying temperature, composition and shear rate. The viscosity in ILs dependence on temperature is determined by the cation and anion interactions. It is expected that this IL system could see 4 times reduction in viscosity when heated from room temperature to 80˚ C (BMIM BF4 4.66 x reduction from 20C (112 cP) to 70C (24

cP)) [135]. It will be shown that the ionic liquids are shear thinning under all conditions. This makes it difficult to apply the Koutecky-Levich analysis directly, as the there is significant increase in shear rate over the changing RPMs, from 50 to 1000, and this has significant impact on the viscosity, diffusion layer size and also the diffusion itself. Initially this was thought to be a small contribution as the viscosity is only a $1/6^{th}$ power contribution to the Koutecky-Levich and Levich equation.

The implications of this were more thoroughly investigated in section 6.4 but the Levich analysis is shown here. As an approximation of the viscosity for application in calculating diffusion rates the experimentally determined viscosity was fit with exponential decay equations and the best fit parameters were used in calculations of viscosity in each rotation rate regime. The viscosity was integrated over the r=0 (center of the electrode) to r=2.5 mm (edge of the electrode area) with regards to increasing shear for each of the rotation rates and this approximation of the average viscosity was used directly in the Levich equation for each solution and temperature. The response of the electrolyte with varying potential was tested with linear voltammetry, sweeping the current from 0 mV to -700 mV vs. Al (1.5:1 $AlCl_3$:EMImCl) at 2 mV/s, and the multiple rotation rates are shown on a single graph. Each linear scan is an average of 3 repeated scans after stripping and rest steps to ensure clean electrodes and equilibrium initial conditions. The density and concentration measured at each condition (temperature and composition) were used in conjunction and the current value was measured at -500 mV vs. the reference electrode to calculate and compare diffusion rates.

6.3a Rheology - Composition, Temperature and Shear Dependence

The 1 to 1 ionic liquid is the extreme condition where the solution is Lewis neutral and therefore is only composed of the $AlCl_4^-$ anion and $EMIm^+$ cations and does not deposit aluminum in the potential window of the electrolyte. This chemistry was used as a control and end condition. The physical properties such as viscosity and the electrochemical window of this solution were used as the viable window for the higher concentration electrolytes that deposit aluminum. The viscosity is shown in Figure 51 and is representative of the viscosity trends seen in all solutions regardless of composition, these solutions are shear thinning and reach near Newtonian characteristics around 50 RPM. The other compositions viscosity and parameters were calculated in the same fashion and results are shown in Appendix D.

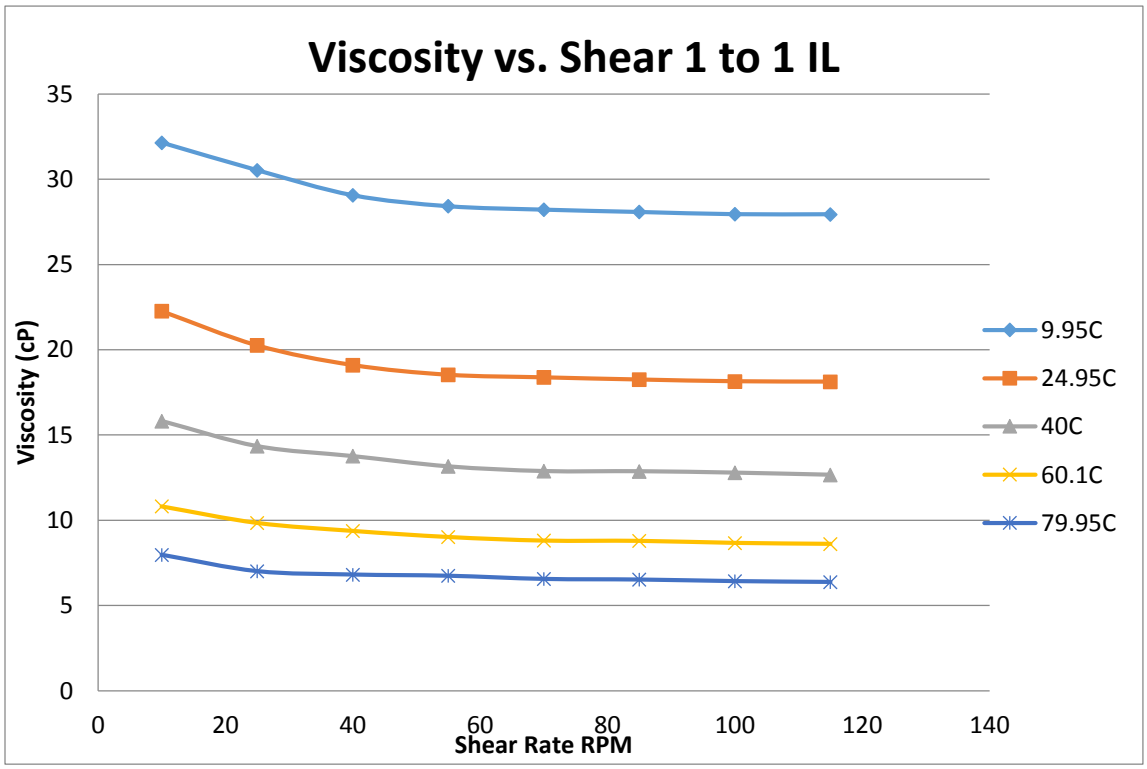

Figure 51: Rheology 1 to 1 Ionic Liquid

The shear thinning follows the power law (Equation 8),

Equation 8: Shear Thinning Power Law

$$\eta = K\gamma^{n-1}$$

Where η is the viscosity, γ is the shear rate, and the K and n constants are derived from a best fit to the experimental data. The viscosity decreases significantly with temperature increase, this is a logarithmic relation to temperature and is demonstrated with a plot of the shear equation constants, Figure 52.

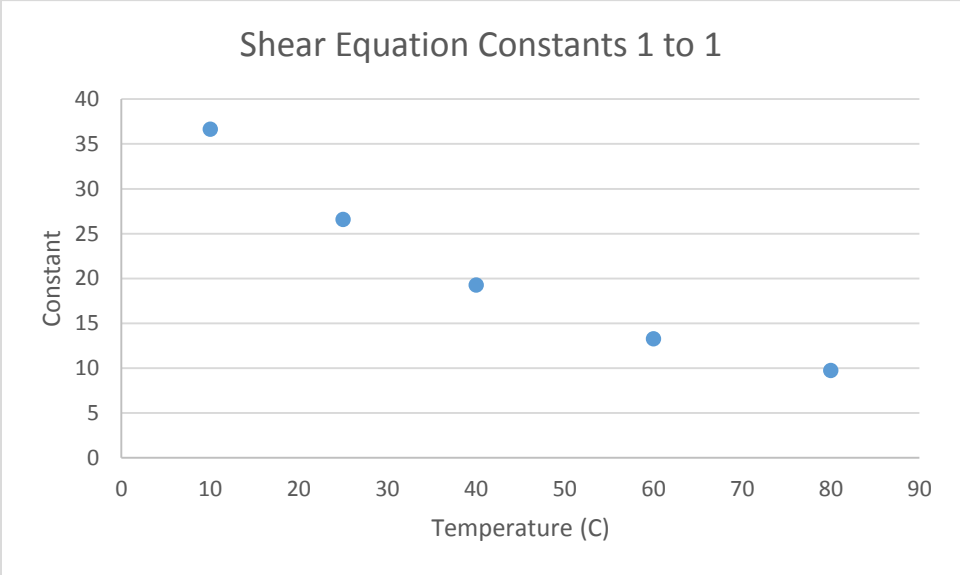

Figure 52: Shear Equation Viscosity Constants 1 to 1 EMImCl:$AlCl_3$ Ionic Liquid

The shear thinning properties increase as the temperature increases, but the variance is small, shown in Figure 53.

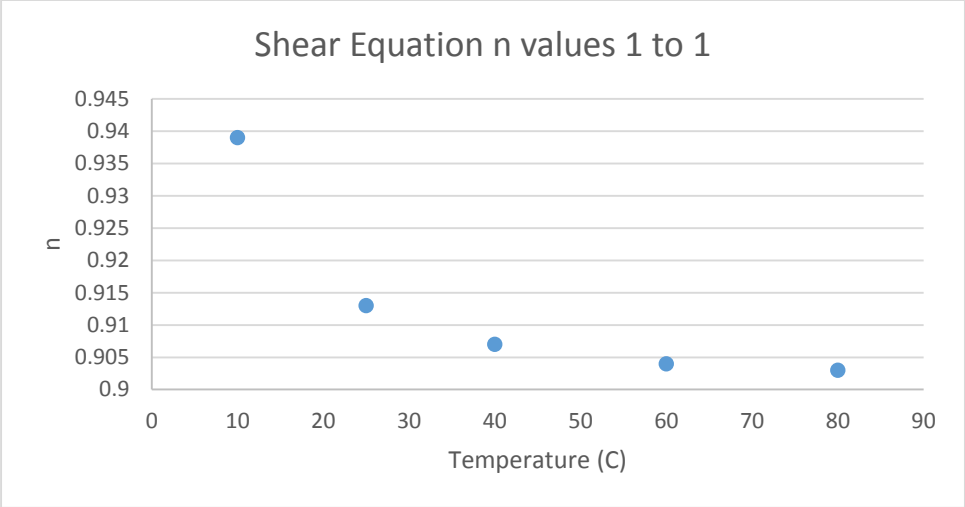

Figure 53: Shear Equation Exponential Constants 1 to 1 EMImCl:AlCl3 Ionic Liquid

In the 1 to 1 electrolyte conditions the shear thinning property increases at higher temperatures. This is a minor change, and is less evident as the viscosity is much less in higher temperatures, and the shear thinning decrease in viscosity is much lower quantity than in the lower temperature regimes.

6.3b Reaction Kinetics and Temperature – RDE Levich

The electrochemical plot, Figure 54, shows the comparison between the Lewis neutral solution and a Lewis acidic solution, demonstrating the negligible electrochemical activity and the reduction of aluminum in higher concentration electrolytes.

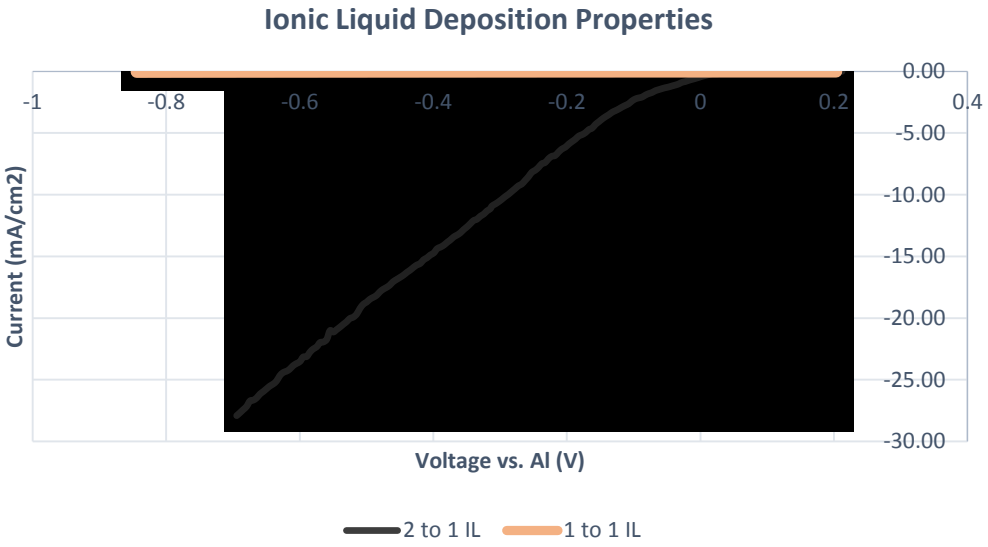

Figure 54: Lewis Neutral vs. Lewis Acidic Electrolyte Reduction Characteristics

This negligible reduction of any component in the electrolyte is due to the absence of the reducible $Al_2Cl_7^-$ anion species. The viscosity gives insight to the physical properties to the $EMIm^+$ $AlCl_4^-$ ionic liquid, which will be used in comparison.

The 4 to 3 ionic liquid is the lowest concentration of $Al_2Cl_7^-$ speciation solution that was tested. This solution is critical for testing because the relatively low concentration of the reducible species is the only way to investigate the diffusion of said species. The higher ratio solutions show almost no pure diffusion limitation conditions, and applying information about the diffusion derived from this system is crucial in determining other influences and constants. This solution has limited use as an aluminum depositing chemistry, as the low concentration of reducible species is unnecessary and causes issues in deposition quality. The 30˚ C scans are shown in Figure 55.

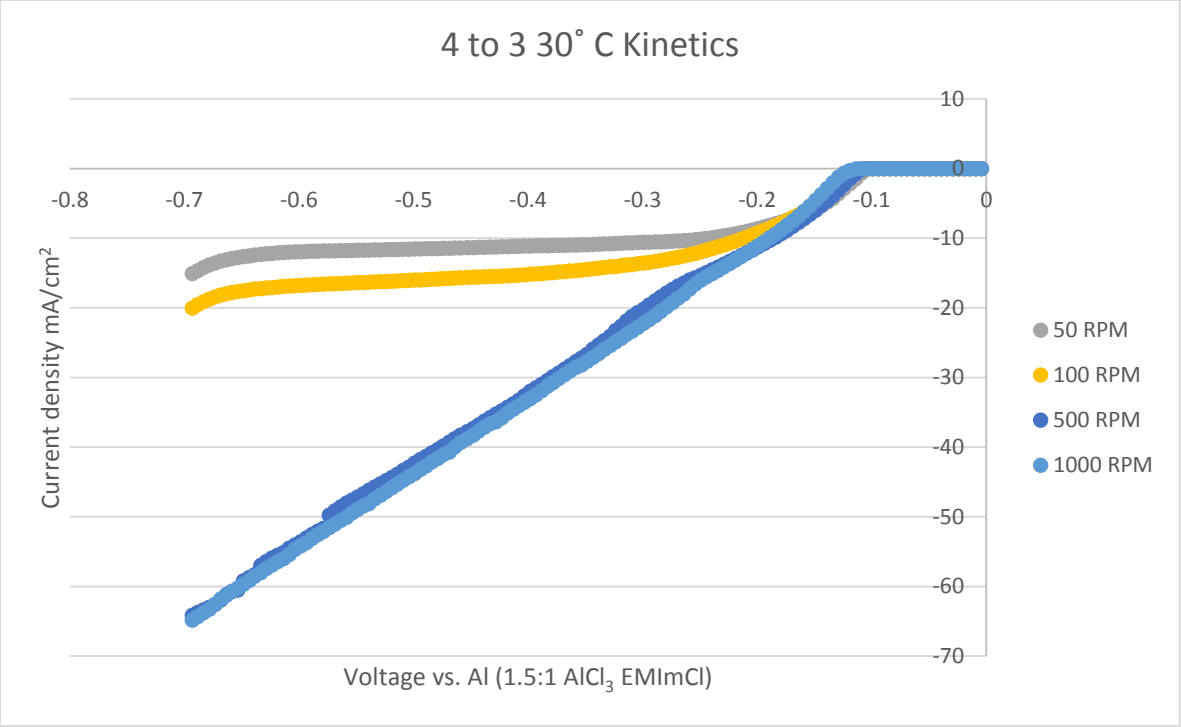

Figure 55: 4:3 EMImCl:$AlCl_3$ Linear Voltammetry Scans, 30˚ C

In the 30C bath, the 50 and 100 RPM rotation rate show typical Levich limiting current at -300mV and stay consistent to around -680 mV, where there is a slight indication of a new reduction reaction beginning at the tail end. Since the 500 and 1000 RPM rotation rate scans are both linear and overlap they are kinetically limited, because if there were diffusion influences there would be discrepancies between the different rotation rates.

The higher RPMs do not show a Levich diffusion limited current and the current in the 500 RPM scan is much higher than the 50 or 100 RPM scans, the shift to dynamic conditions also show an increase in diffusion rate over the diffusion rates measured in static conditions from the Cottrell model. The Levich calculated diffusion rate is roughly 20% higher than the lower rotation rates. Additionally, this is the completely kinetically limited rate, so the actual diffusion is likely much higher, as the reaction rate continues to

increase as the potential becomes more negative, still following the kinetically limited current. The reasoning behind the discrepancy between the diffusion rates calculated by the Cottrell method and the Levich equation, as well as the increased rate at higher RPMs, along with the Levich kinetic and diffusion data compiled, is presented and discussed in chapter 6.3c.

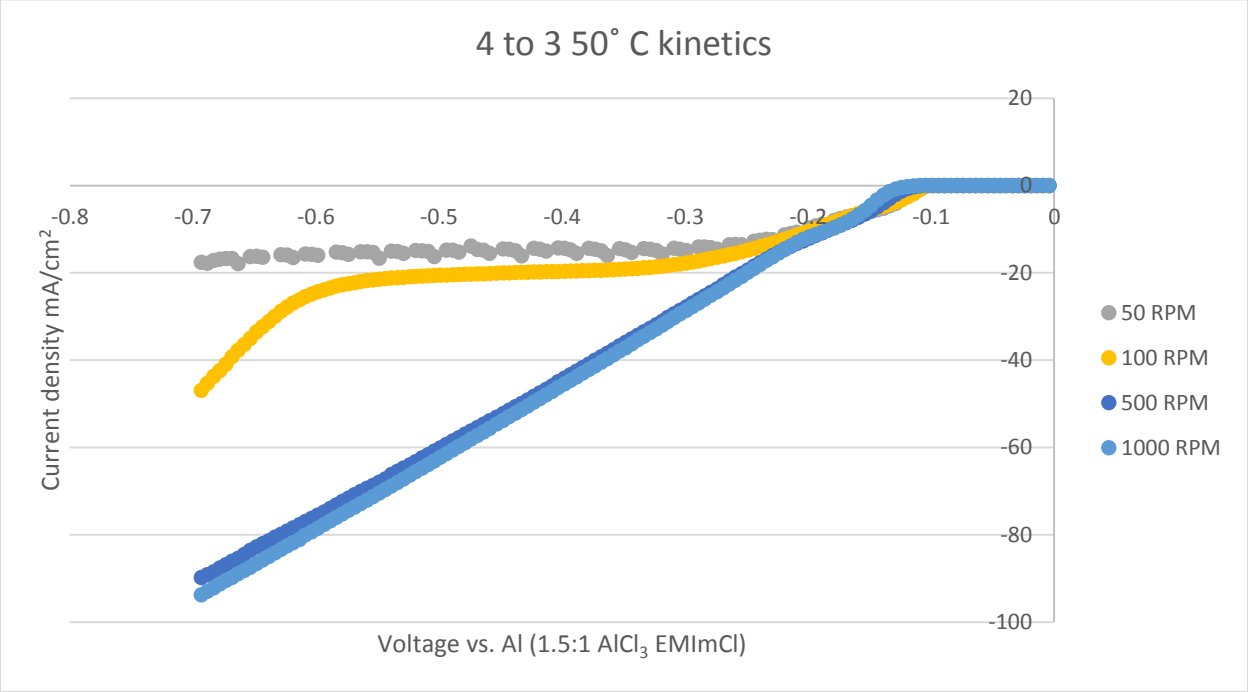

Figure 56: 4:3 EMImCl:$AlCl_3$ Linear Voltammetry Scans, 50˚ C

The linear scans at 50˚ C are very similar to those at 30˚ C, with increased kinetic rates leading to higher reduction currents in all cases. The 500 and 1000 RPM scans are again linear and again overlapping, indicating the solution surpasses diffusion limitations at an RPM of lower than 500.

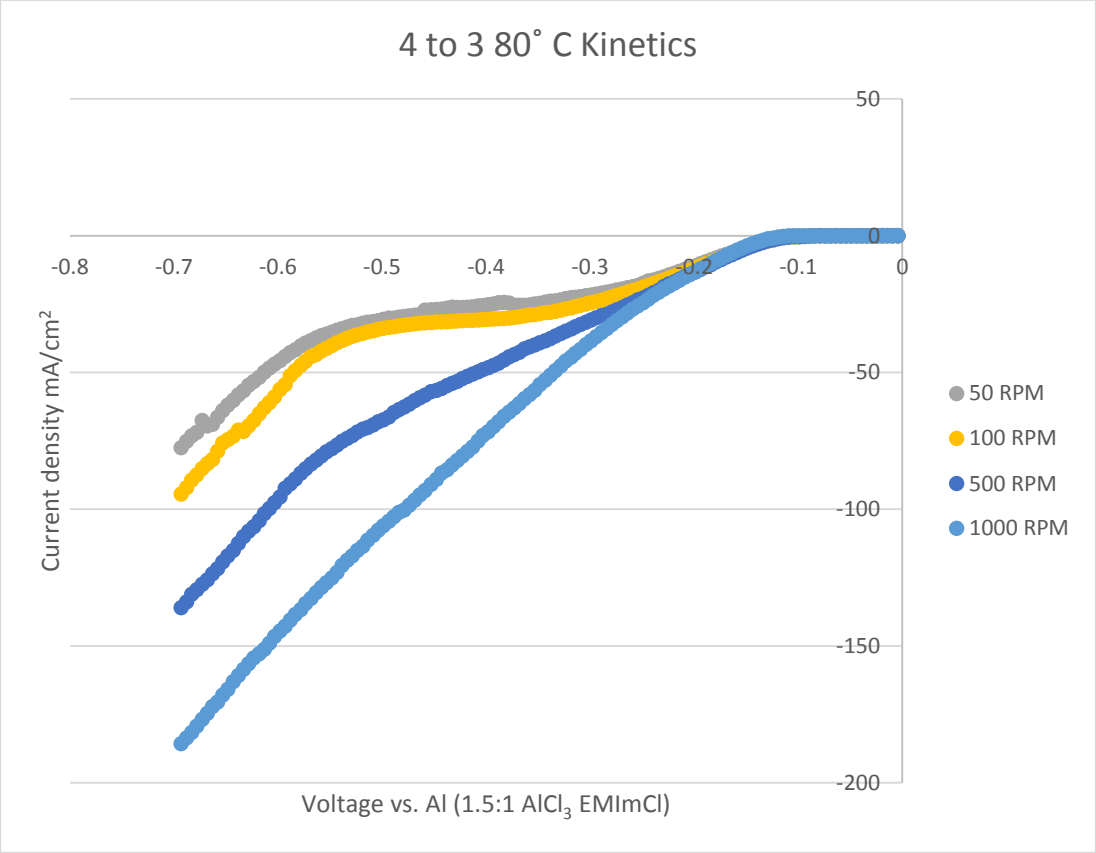

Figure 57: 4:3 EMImCl:$AlCl_3$ Linear Voltammetry Scans, 80˚ C

As the temperature increases the deposition current in the 500 and 1000 RPM scans separate, showing that the diffusion implications are having more effect, as the 500 RPM conditions in lower temperatures are only kinetically limited. This shows that the increase in kinetic rate due to temperature increases faster than the diffusion implications in this composition.

The kinetic limitations become less influential in the higher temperature scans and the diffusion becomes a stronger contributing factor in the electrochemical reduction. The 500 RPM condition is mixed kinetic and without more information it is not possible to determine the true kinetic limitations, as the 1000 RPM may still have diffusion limitations and there were not conditions to compare it to.

The 5 to 3 solution at 30˚ C shows the 500 and 1000 RPM rates very consistently overlaid so they are kinetically limited (not diffusion limited or mixed, because the different rotation rates do not change reduction rates), somewhat similar, low temperatures show diffusion limitations on the 50 RPM, mixed on the 100 RPM and only kinetic limitations on the 500 and 1000 RPM conditions. Diffusion limitations are observed at higher temps and once again the kinetic rate increases faster than the increased contribution due to diffusion, as was seen in the 4:3 case.

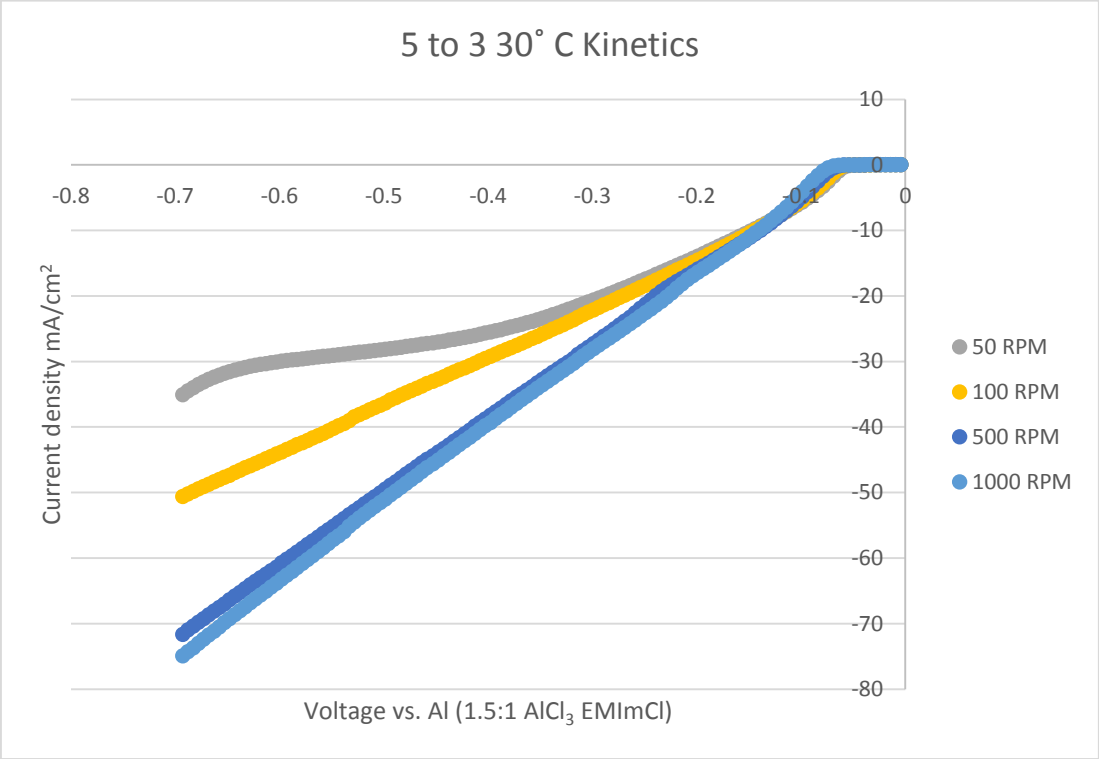

Figure 58: 5:3 EMImCl:$AlCl_3$ Linear Voltammetry Scans, 30C

There is evidence of diffusion limitations in the 50 RPM scans while the higher rotation rates (100, 500 and 1000 RPMs) are linear, indicating kinetic or mixed diffusion and kinetic limitations. There is a slight increase in the tail end of the of the 50 RPM chemistry that is not shown in the kinetically limited scans. The reducing current does

increase with increasing rotation rate demonstrating at least mixed diffusion and kinetic influences. As the 100 RPM scan does not show a Levich diffusion limited current plateau, it is influenced by kinetic limitations. As it is much lower current than the 500 and higher RPM scans it must also be influenced by diffusion limitations, putting it in the mixed limitation regime.

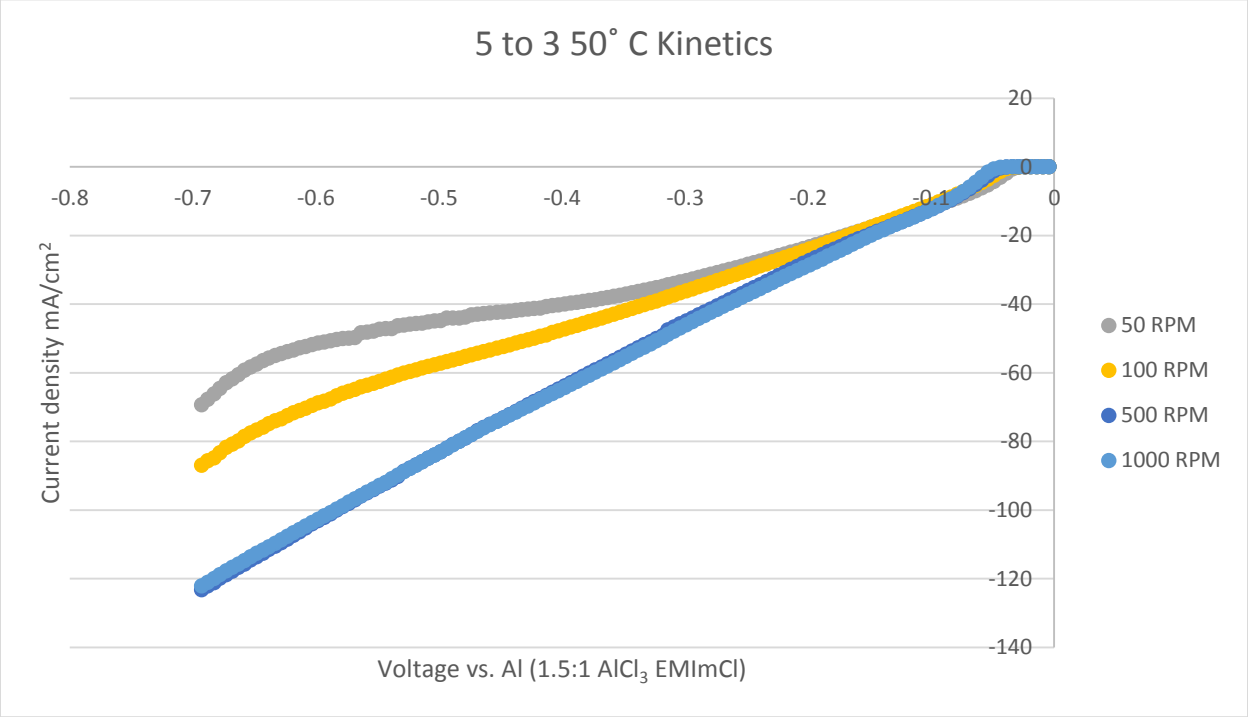

Figure 59: 5:3 EMImCl:$AlCl_3$ Linear Voltammetry Scans, 50˚ C

The 50˚ C conditions shift the curves slightly, the 100 RPM scans now show slight diffusion limitations and Levich profiles are present but still show increasing rate overpotential shifts and are therefore not completely diffusion limited. The 500 RPM and 1000 RPM align showing pure kinetic limitations in both. This indicates more diffusion limitations at lower RPM (100 and below) and reaches purely kinetic limitations at an RPM value that is below 500 RPM.

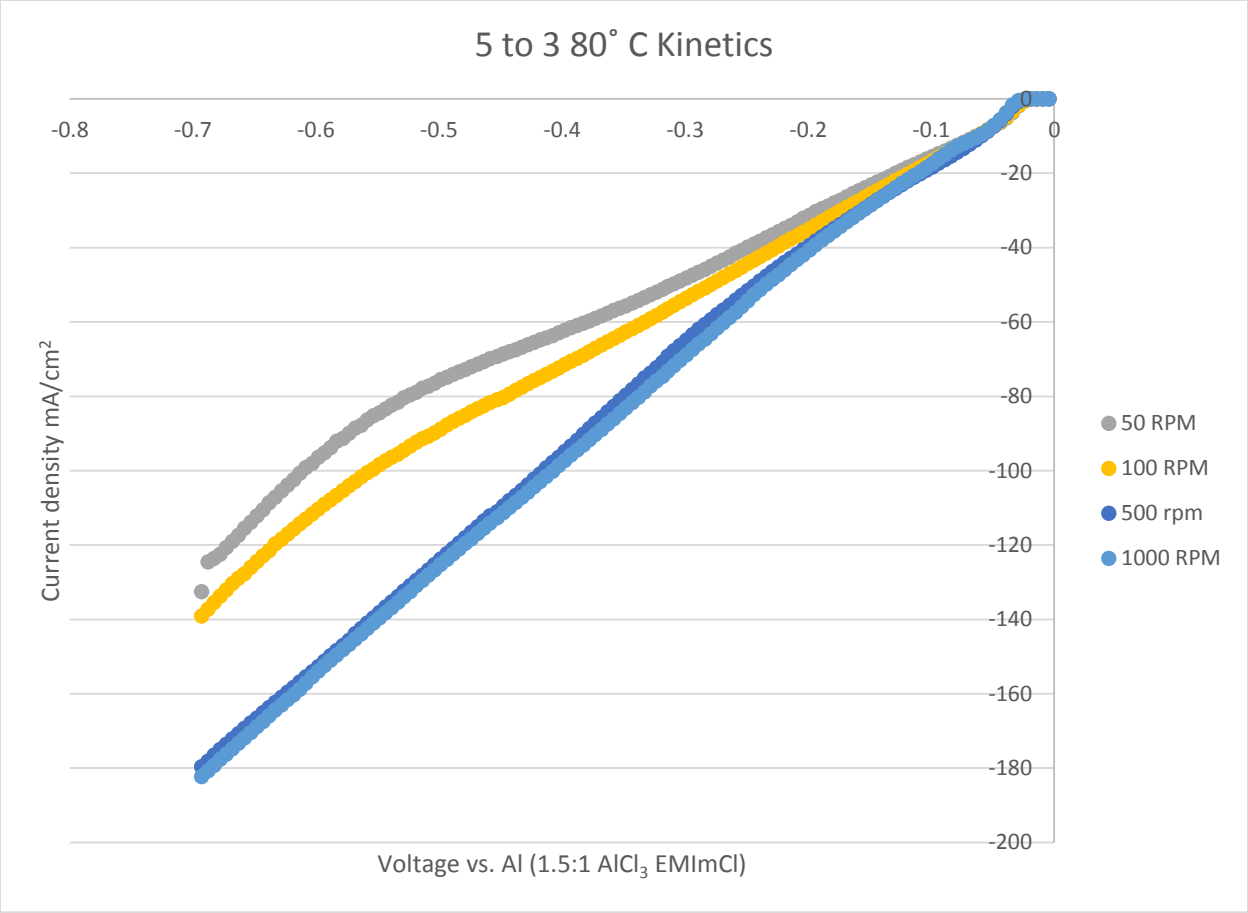

Figure 60: 5:3 EMImCl:$AlCl_3$ Linear Voltammetry Scans, 80˚ C

The 5 to 3 bath at 80˚ C shows the same overlap of the 500 and 1000 RPM scans. This again indicates only kinetic limitations. The 50 and 100 RPM scans show slight Levich profiles but never plateau and never purely diffusion limited. although the currents do not match up as well at this higher temperature. Using the Levich relations the predicted diffusion limitation currents for 500RPM are 210 to 250 mA/cm2, well above the observed currents which explains why the 500 and 1000 RPM overlap so closely, they are truly kinetically limited. All of the scans in the 5 to 3 bath at 80˚ C show significant kinetic influence.

The 2 to 1 electrolyte scans weren't purely diffusion limited under any dynamic conditions measured here. All scans were linearly increasing with overpotential, but do increase in current with the rotation rate as well, indicating strong kinetic and diffusion influence and limitations.

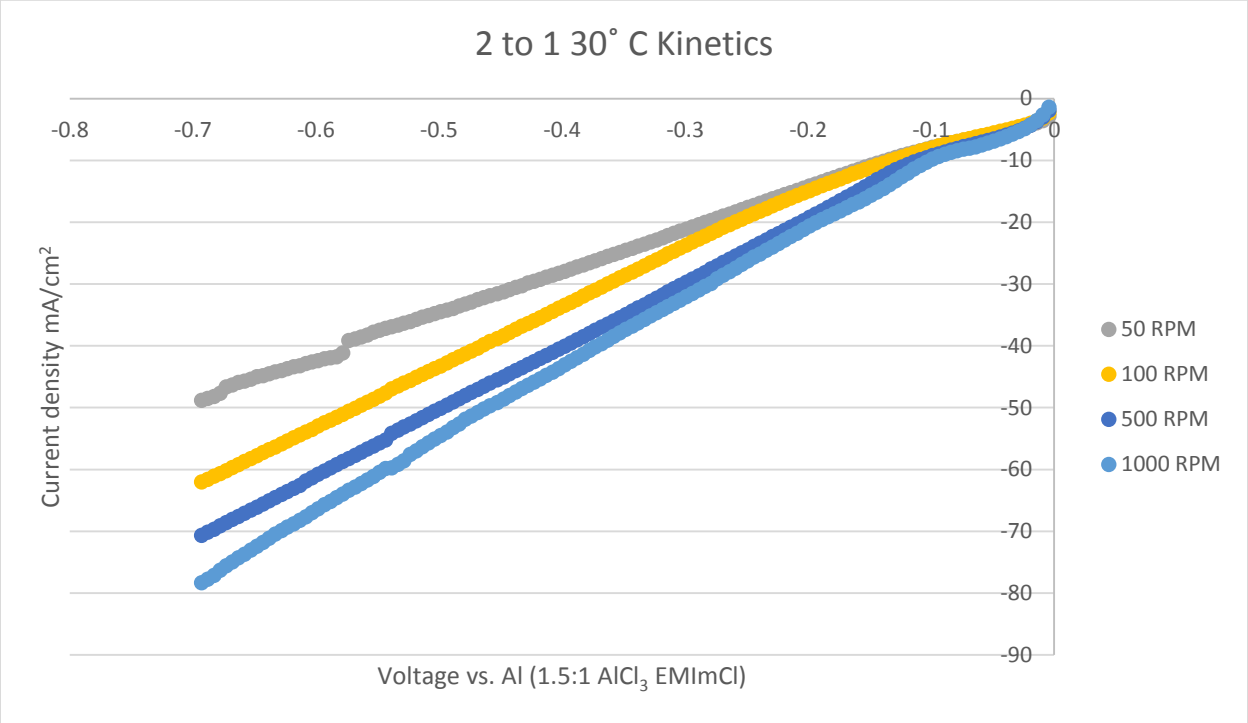

Figure 61: 2:1 EMImCl:$AlCl_3$ Linear Voltammetry Scans, 30˚ C

The 2 to 1 30˚ C bath shows all scan rates as both kinetically and diffusion limited. The simple explanation is that the concentration in this chemistry is too high to fully reach a diffusion limited regime, while the diffusion still influences the reduction rates. All of these scans are linear with potential but all of them also change with rotation rate. Since the 1000 RPM does not align with the 500 RPM condition, it is apparent that there are still mixed diffusion and kintetic limitations at 500 RPM. However we cannot determine that the 1000 RPM condition still has any diffusion implications without further analysis. Compared to the 4 to 3 electrolyte at 30˚ C and accounting for the 120

mV concentration polarization shows the kinetic limit senen here in the 1000 RPM scan matches the kinetic limits in the other electrolyte. It is unclear at this point why the mixed diffusion limitations reduce the current at the 500 RPM scan rate.

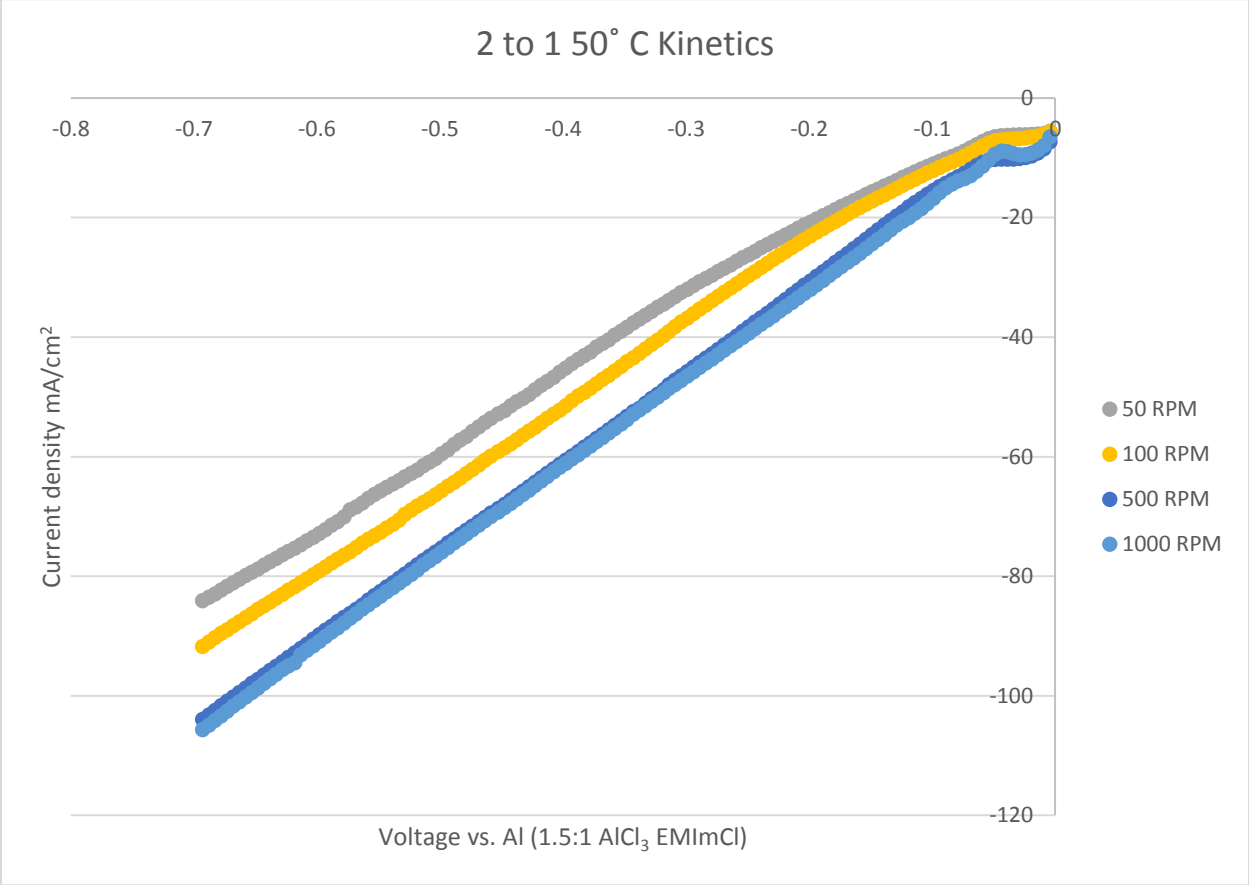

Figure 62: 2:1 EMImCl:$AlCl_3$ Linear Voltammetry Scans, 50˚ C

In the 2 to 1 chemistry at 50˚ C all scans are purely linear with potential, indicating either complete kinetic or mixed kinetic and diffusion limitations. The 500 RPM and 1000 RPM scans overlap at this temperature, indicating they are both purely kinetically limited.

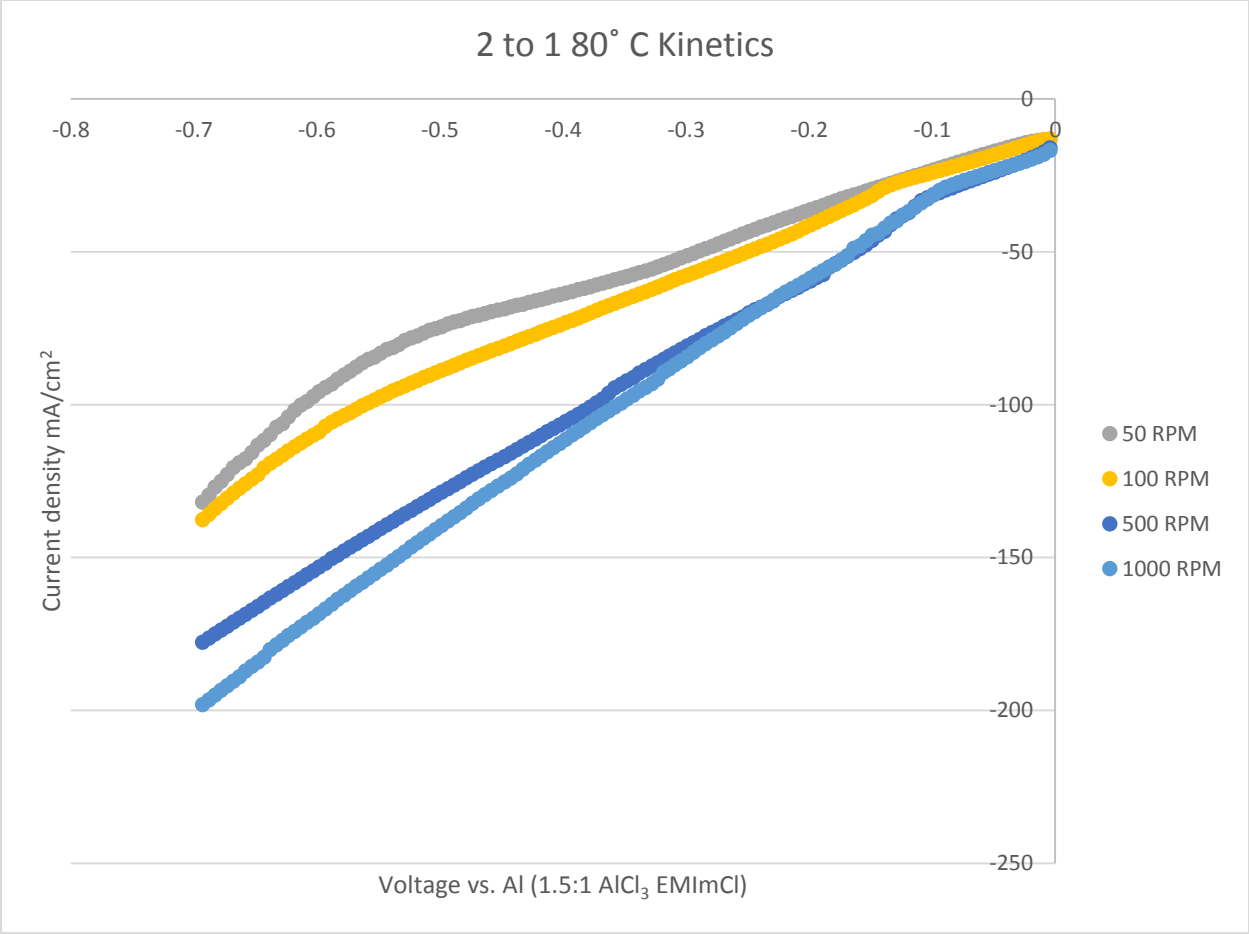

Figure 63: 2:1 EMImCl:$AlCl_3$ Linear Voltammetry Scans, 80˚ C

In the 2 to 1 chemistry at 80˚ C there was continual increase in reaction rate. The 50 and 100 RPM rotation rate scans are mixed kinetic and diffusion limitations, as they show heavy diffusion limited profiles but continually increase in current with increasing overpotential. This electrolyte exhibits the same trend as the 4 to 3 bath, the kinetics seem to increase faster than the diffusion, at 80 C, there is a slightly more diffusion limited characteristics in the lowest rotation rate condition. No conditions measured here led to Levich limited current regimes, and therefore the diffusion constants determined by applying the Levich equation are all underestimated.

6.3c Profiling Diffusion and Kinetic Limitations

The complete dataset is represented below, with emphasis on the profile of the linear voltammetry scan. The diffusion rates for the diffusion and mixed limitation regimes are given, and the current density at -500 mV vs. reference are also displayed. The blue areas are pure diffusion limited, the green areas are mixed limitations and the orange regions are kinetically limited. Most solutions at high rotation rates reach the kinetic limitations and they are consistent between electrolyte compositions, the difference in values shown on the graphs is the result of shifted concentration polarization vs. a consistent concentration reference electrode.

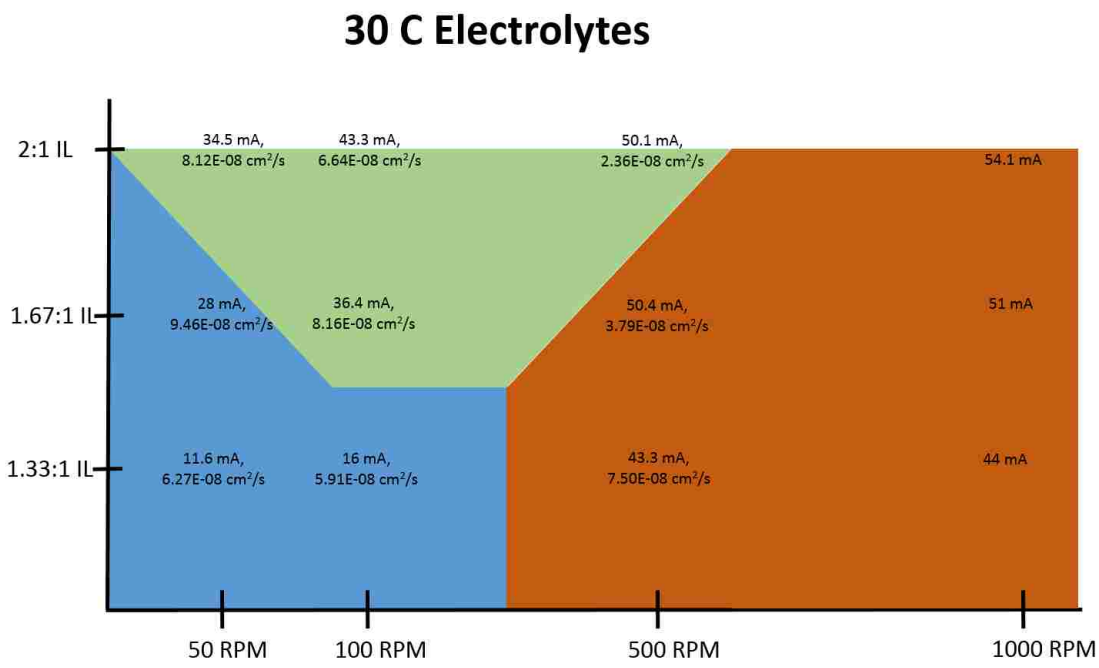

Figure 64: EMImCl Electrolyte Rotating Disc Linear Scan Profiles, 30˚ C

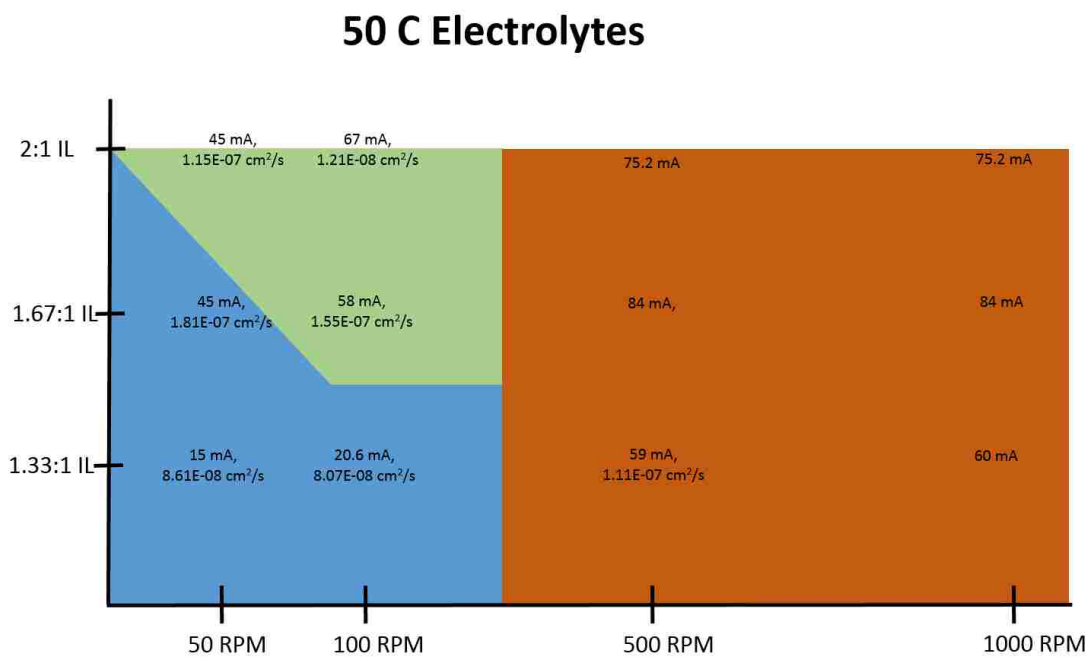

Figure 65: EMImCl Electrolyte Rotating Disc Linear Scan Profiles, 50˚ C

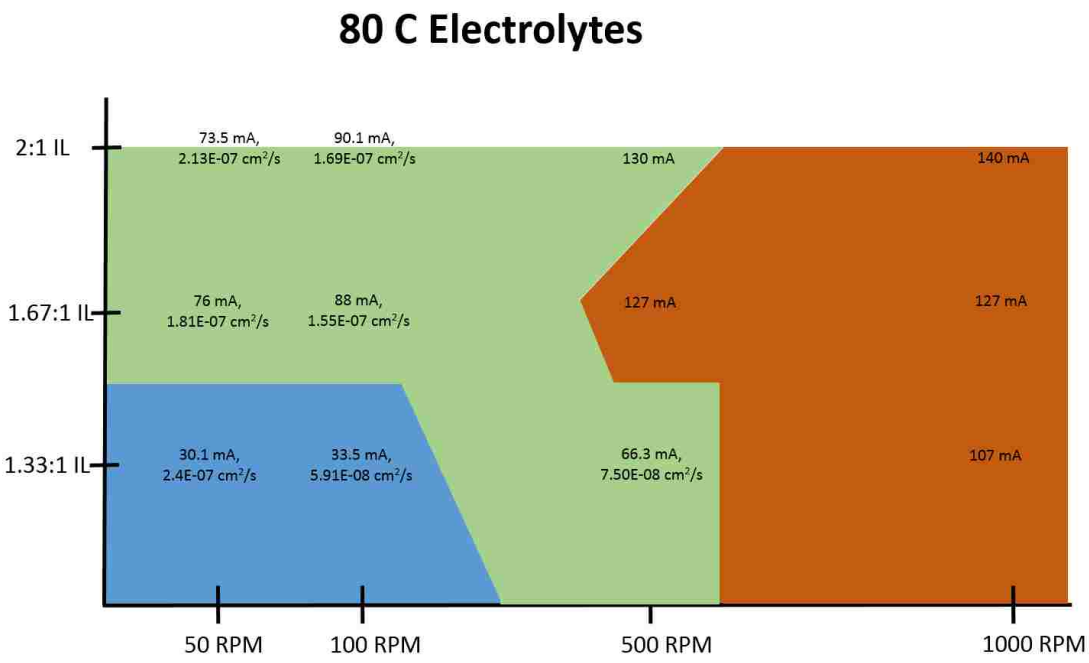

Figure 66: EMImCl Electrolyte Rotating Disc Linear Scan Profiles, 80˚ C

Since the solutions shift to diffusion limitations at higher temperatures it shows that the kinetic rates are increasing with temperature faster than the diffusion rate. This is amplified since at increased temperatures the viscosities are drastically reduced, decreasing diffusion layers' thicknesses and reducing the diffusion distances and the reactions still become more diffusion limited. This must be taken account when trying to increase deposition kinetics rates with temperature, as it could transition to diffusion limited regimes and cause poor film quality.

6.4 Analysis of Anionic Mobility

The viscosity measurements gave unexpected trends when compared across the composition range. Comparing the rheology data with the Cottrell diffusivity data for the $Al_2Cl_7^-$ anionic species (the Levich data had many kinetically limited influences so Cottrell was used) showed inverse correlations as expected. The viscosity is highest in the 4 to 3 solution and decreases consistently to the 2 to 1 chemistry (the 1:1 chemistry has low viscosity as well, on par with the 2:1 solution, but does not have any $Al_2Cl_7^-$ speciation so it is not shown here). The $Al_2Cl_7^-$- mobility increases over this range as shown in Figure 67, and the viscosity measurements are taken from the values of the rheology measurements at 25 RPM and 25˚ C.

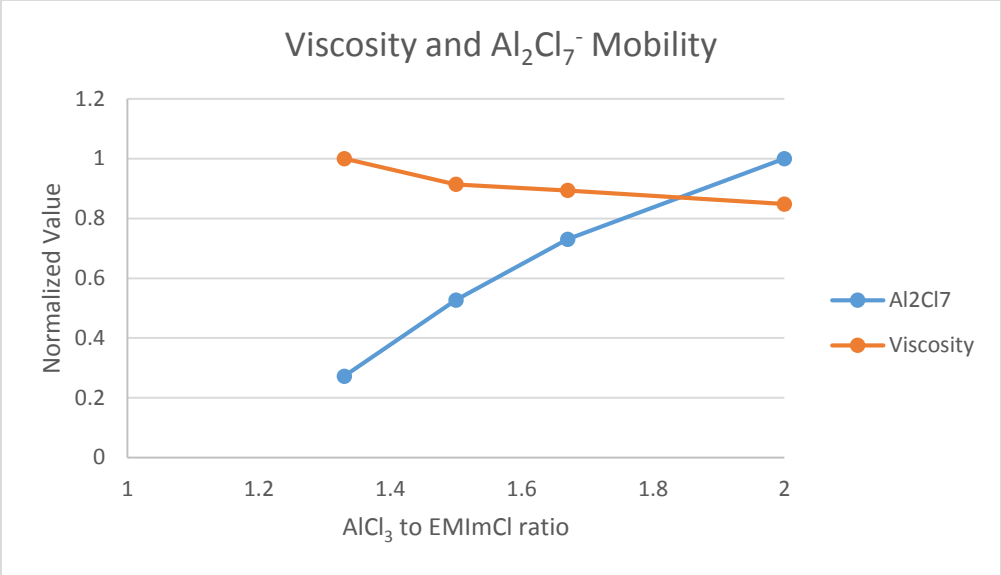

Figure 67: Viscosity vs. $Al_2Cl_7^-$ Diffusivity, Normalized

The diffusion of the of the reducible species increases with composition, and it also increases with shear. This is evident from the increased mobility measured from the Cottrell method under static conditions and those measured from the Levich method under dynamic conditions, the comparison is shown in Figure 68, where the Levich calculated rates is divided by the Cottrell rate. The 2 to 1 solution has underestimated diffusion rates as all of the measurements are kinetically limited, and therefore actual diffusion is at least this high but cannot be determined exactly.

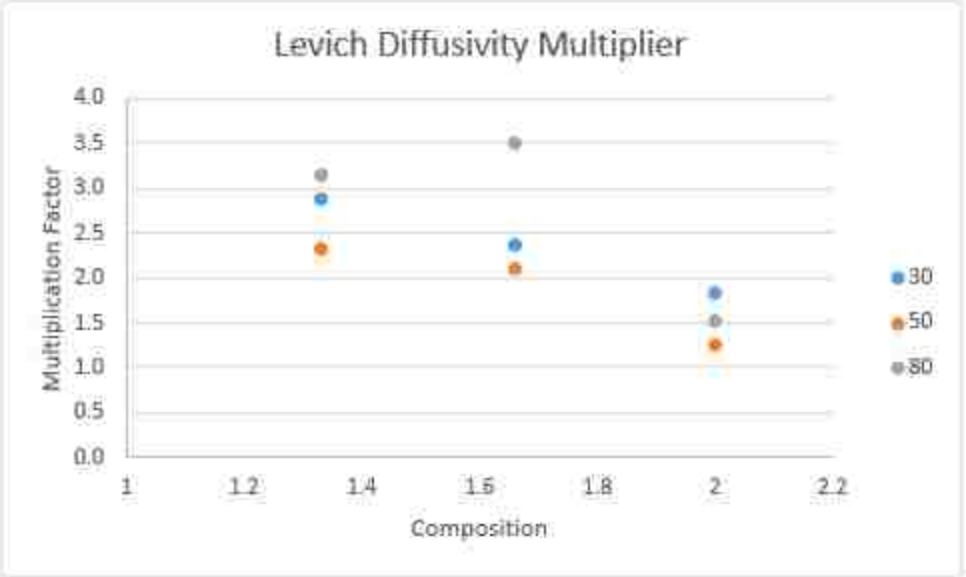

Figure 68: Increase in Diffusion From Static to Dynamic Measurements

Viscosity decreases with both increasing composition and shows significant decrease with shear, as seen in the shear thinning property. The correlated increase in diffusion of the reducible species is likely influenced from this by decreased interactions between ions that are disrupted under shear. Since the viscosity is lowest at the 1 to 1 and 2 to one compositions, the anionic interactions, either $AlCl_4^-$ or $Al_2Cl_7^-$, with the cation is likely not associated with the increased viscosity trends. This indicates that the increased viscosity is possibly due to the $AlCl_4^-$ or $Al_2Cl_7^-$ interaction with each other. The suppressed mobility in the mixed $AlCl_4^-$, $Al_2Cl_7^-$ compositions was thought to be attributed to fluctuance, attractive interactions between the anionic species, much like van der Waals attraction commonly seen in cations with long side chains. Gaussian simulations of the intermediate species in the fluctuance, an $Al_3Cl_{10}^{2-}$ component indicates that it would be stable, even though it is comprised of 2 anionic species. This indicates that anionic attraction is feasible in this case, even with the electrostatic repulsion. The predicted stable configuration is shown in Figure 69.

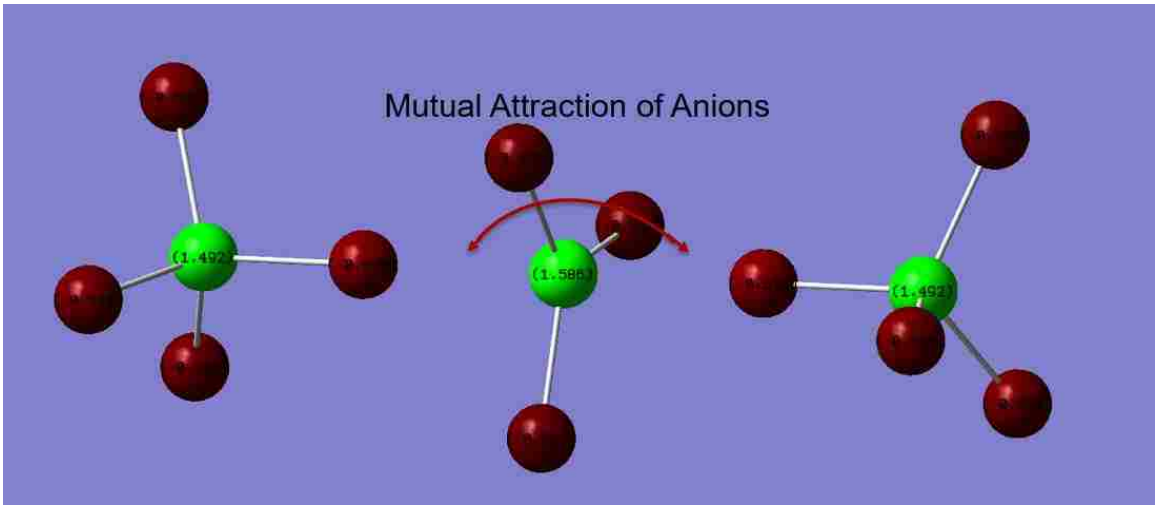

Figure 69: DFT of Anionic Species Mutual Attraction

To check if this anionic interaction was indeed happening requires information on the $AlCl_4^-$ mobility, if it is interacting with the reducible species it will follow the same mobility trend with viscosity. This is difficult to measure directly and will be calculated from a combination of mobilities and conductivity in the next sections. Getting information on the $Al_2Cl_7^-$ interactions and how these interactions are effected by shear will elucidate the observed change in mobility and viscosity.

6.5 Mobility in Static Regimes

Expanding the data collected in static measurements to dynamic conditions might be done through a relationship to viscosity, which can be measured at zero shear and through the entire dynamic regime. As shown by the Al27 NMR, the electrolyte only contains the imidazolium cation and 2 anionic species. Two of the mobilities can be measured directly, using the Cottrell equation to measure the reducible $Al_2Cl_7^-$ species and pulse field gradient NMR to measure the mobility of the cationic imidazolium

species. The third specie's, the anionic $AlCl_4^-$, mobility cannot be measured directly but should be accounted for in the total conductivity of the solution. Measuring the conductivity and accounting for the contribution of the two known ionic components should allow for extraction of information about the $AlCl_4^-$ mobility.

6.5a Conductivity

The conductivity is a strong indicator of ionic liquid optimized concentration and diffusion parameters, and measuring the conductivity at varying compositions and temperatures will give information on the mobility of the ionic components and the optimal conditions for electrodeposition. The conductivity was measured from room temperature to 80˚ C in the range of ionic liquid compositions and the data is shown in Figure 70.

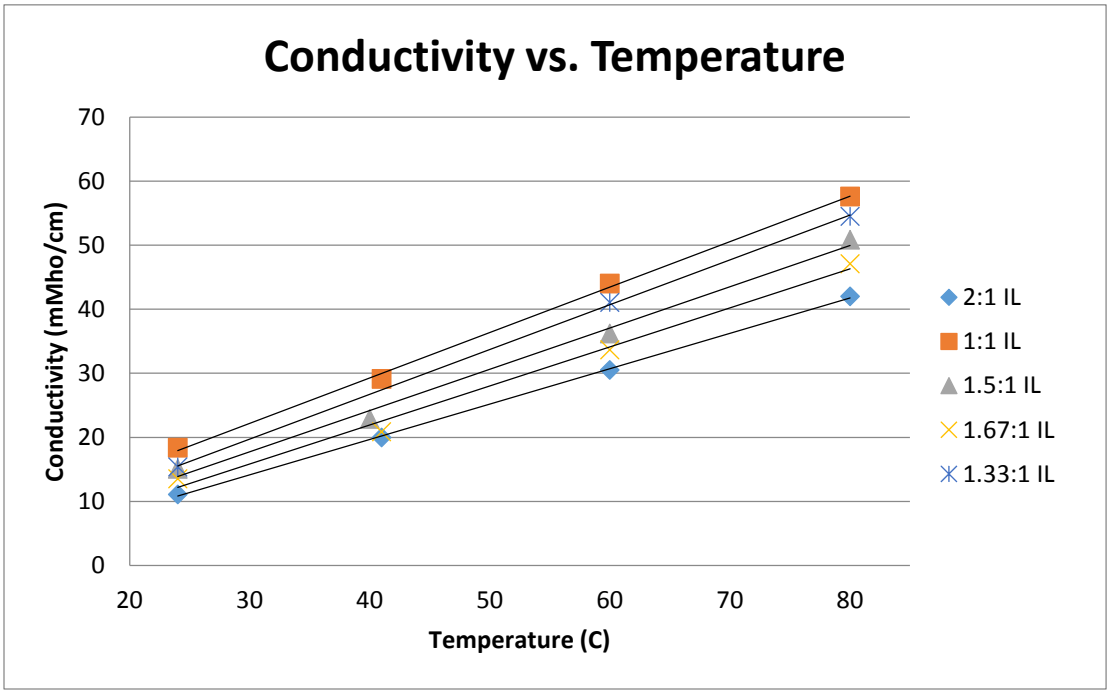

Figure 70: Conductivity of EMImCl:$AlCl_3$ Electrolytes

The conductivity increases linearly in each composition over the temperature range and increases linearly with decreasing $AlCl_3$ composition at all temperatures.

At 25˚ C, the conductivity decreases linearly with increasing $AlCl_3$ composition. This indicates that the $AlCl_3$ additions that shift the concentration away from the $AlCl_4^-$ species are promoting a less mobile $Al_2Cl_7^-$ speciation, but this shift also incorporates a decrease in total ionic concentrations, as shown by the measurements in Chapter 4. The summation of this data is shown in Figure 71, comparing the ionic concentrations of each components to the change in conductivity over the composition range.

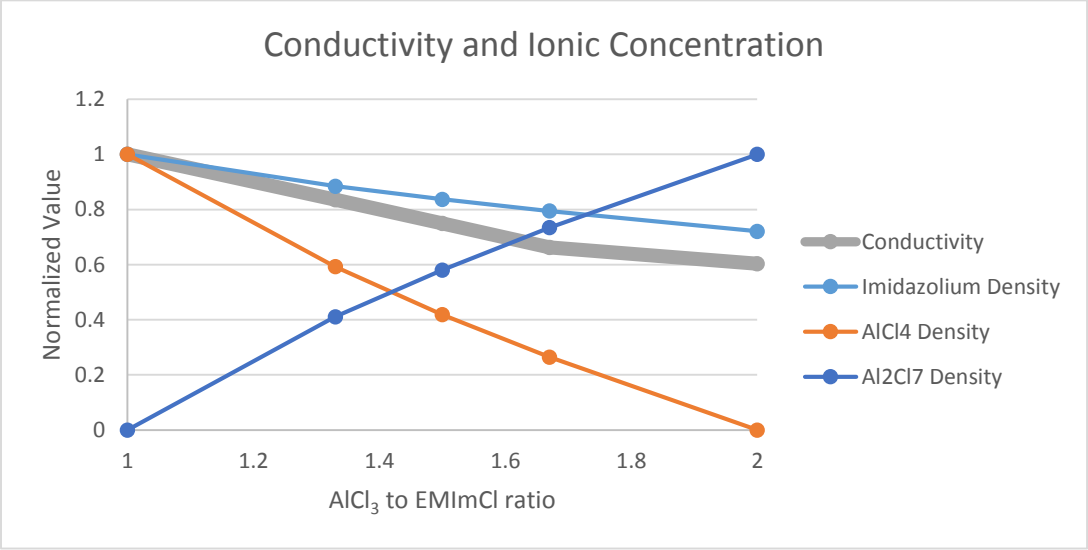

Figure 71: Conductivity Trends vs. Ionic Concentrations

The decreasing ionic concentration and shift towards $Al_2Cl_7^-$ both contribute to the conductivity decrease.

6.5b PGSE – Imidazolium Diffusivity

Pulse field gradient spin echo NMR was used, as described in chapter 2, to determine the diffusion rates of the cationic imidazolium species. Data from a scan of the IL is shown in Figure 72. The profile of this curve along with constants based on pulse length, time between pulses and instrument specific constants are used to calculate diffusion constants.

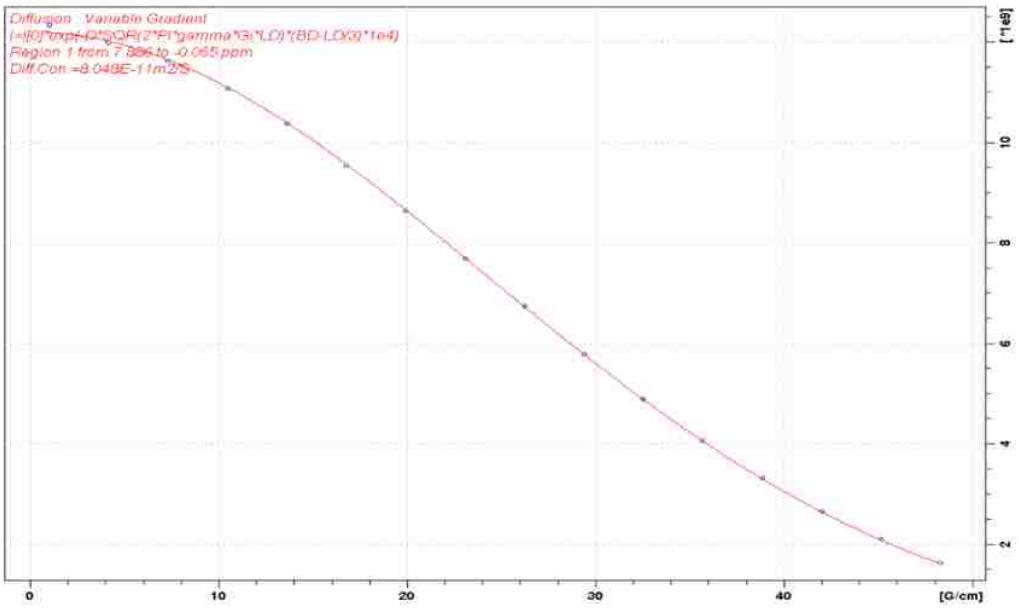

Figure 72: PGSE Data Signal Decay and Diffusion Constant

The PGSE NMR was run for different composition solutions through a temperature range from 25˚ to 80˚ C, and the results are shown in Figure 73.

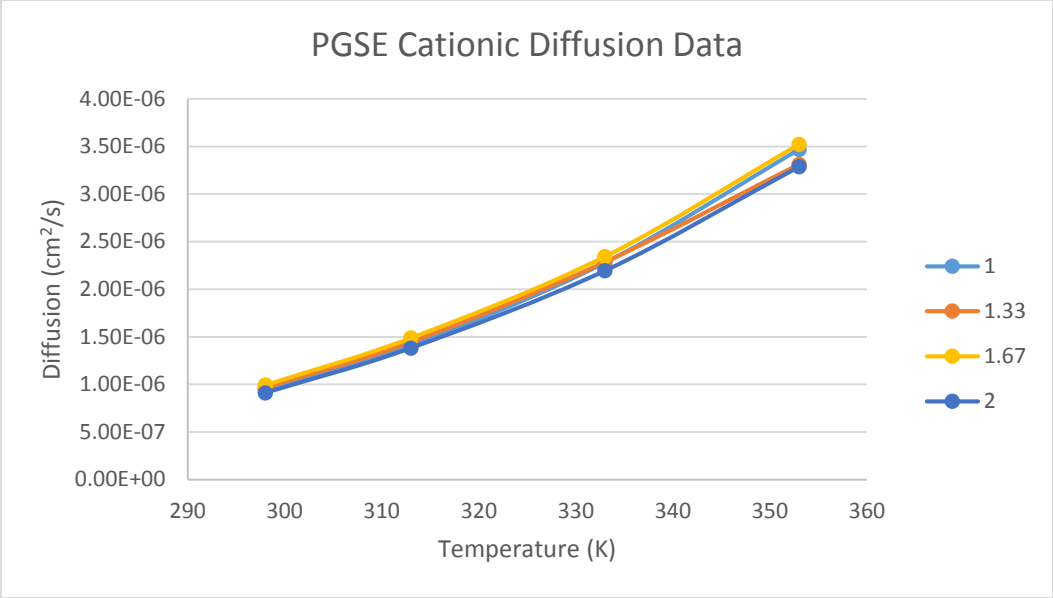

Figure 73: Cationic Diffusion Data

The proton NMR diffusion data showed increasing rates with increasing temperature as expected, however there is no significant change in diffusion rate with varying composition, indicating there is no significant structure change or coordination with the larger or smaller anionic species that affects the cationic mobility. This is contrary to the viscosity data and the opposite of the $Al_2Cl_7^-$ trends.

6.5c $AlCl_4^-$ Diffusivity from Conductivity

While the conductivity decreases as the composition shifts from $AlCl_4^-$ to $Al_2Cl_7^-$, the ionic concentration also decreases. The conductivity follows the same trend as the imidazolium concentration and there is likely some contribution of from the anionic species, with higher contribution from the smaller $AlCl_4^-$ anion. This ion is smaller and should have more contribution to the conductivity and the effect is reduced as its concentration is depleted. The relationship between ionic concentration and mobility to

the electrolyte conductivity are given by the Nernst Einstein equation. Applying the Nernst Einstein equation to only the cationic charge carrier shows it can account for nearly all of the conductivity in all conditions, as seen in Figure 74 and Figure 75. The cationic mobility is much higher than the $Al_2Cl_7^-$ species, as was shown previously. The anionic and cationic diffusivities predict a higher conductivity than is experimentally measured in some cases and this makes it difficult to determine the anionic species actual contribution to the conductivity, as. This is very common and has been used as a method to attempt to determine the "iconicity" of ionic liquids [119].

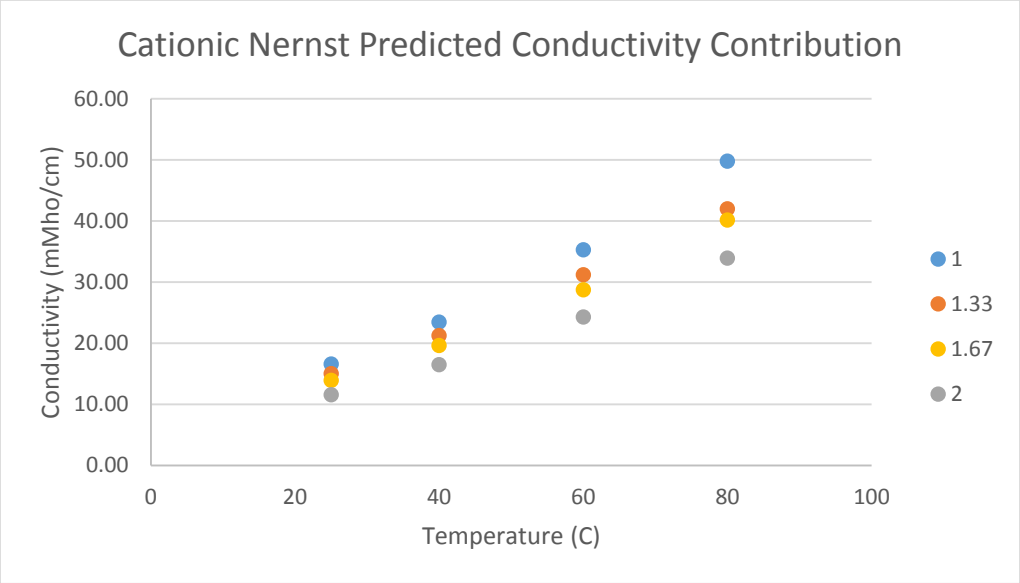

Figure 74: Nernst Predicted Conductivity of the Cationic Species $EMIm^+$

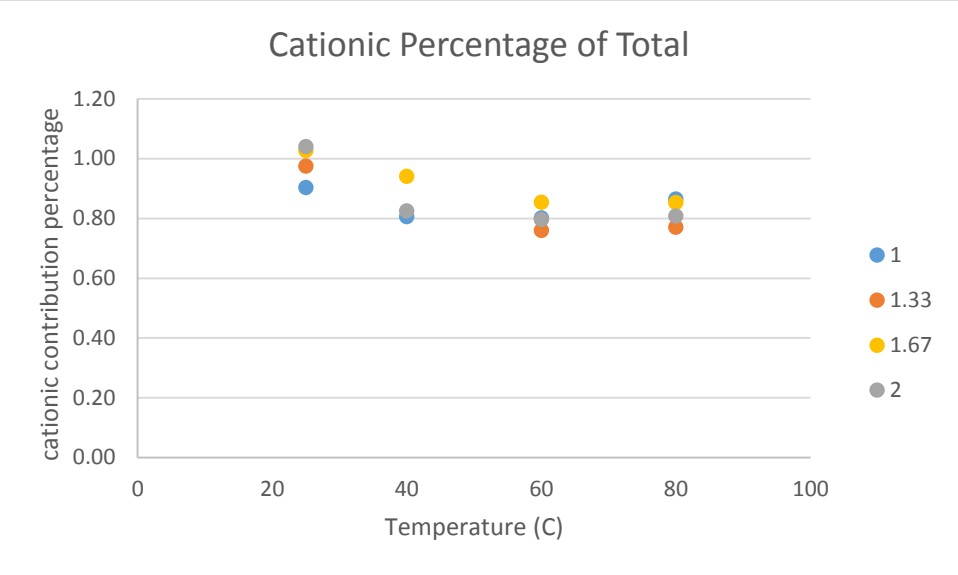

Figure 75: Cationic Species EMIm+ Percentage Contribution to Total Conductivity

At higher temperatures the anionic contribution seems to increase, as only 80-90% the conductivity of the solution is only accounted for by the cationic species. The $Al_2Cl_7^-$ anionic contribution to the conductivity was calculated and is very small, as low as 1% of the contribution of the cationic species, its contribution to the conductivity is shown in Figure 76.

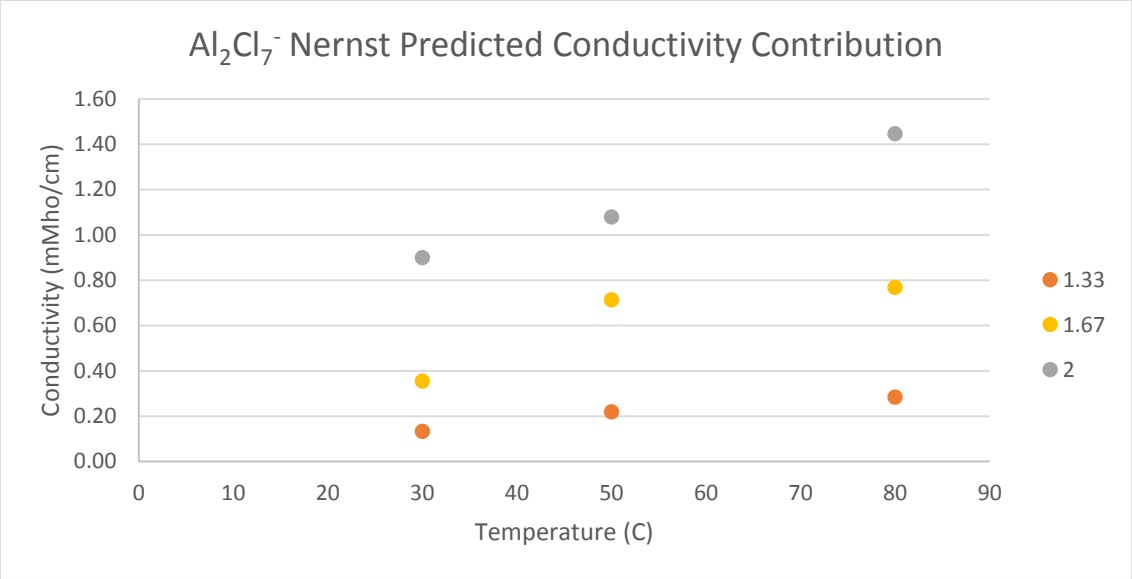

Figure 76:Nernst Predicted Conductivity of the Anionic Species $Al_2Cl_7^-$

If the $AlCl_4^-$ conductivity is assumed to make up only the difference between the Nernst predicted and the total conductivity it is also a relatively small contributor. Once the conductivity contributions of the imidazolium cation and the $Al_2Cl_7^-$ anion are calculated their participation was subtracted from the experimentally measured conductivity of each solution. The unaccounted for conductivity is shown in Figure 77 and is assumed to be from only the remaining $AlCl_4^-$ anionic species.

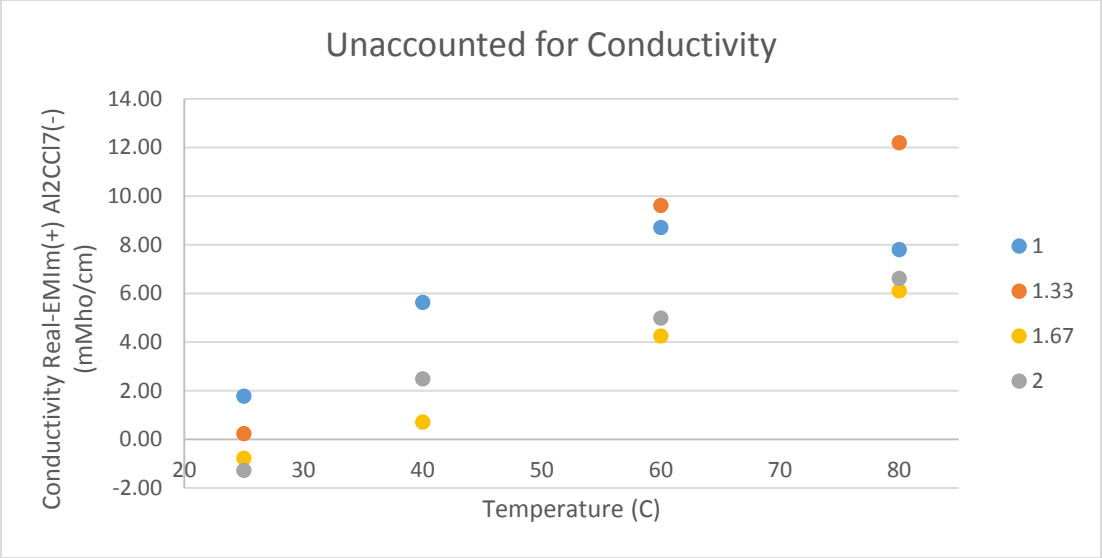

Figure 77: Unaccounted for Conductivity from $EMIm^+$ and $Al_2Cl_7^-$ Conductivity Contributions

There are obvious discrepancies as the 2 to 1 electrolyte at elevated temperatures still has remaining unaccounted for conductivity, even though there is assumed to not be any remaining species that can contribute. While the 1 to 1 and 1.33 to one show the largest unaccounted for conductivity they also have the highest concentration of the $AlCl_4^-$ species. Applying the Nernst Einstein relation in reverse allows conversion the conductivity contribution and the $AlCl_4^-$ concentration to predict the mobility of the remaining $AlCl_4^-$ species, shown in Figure 78.

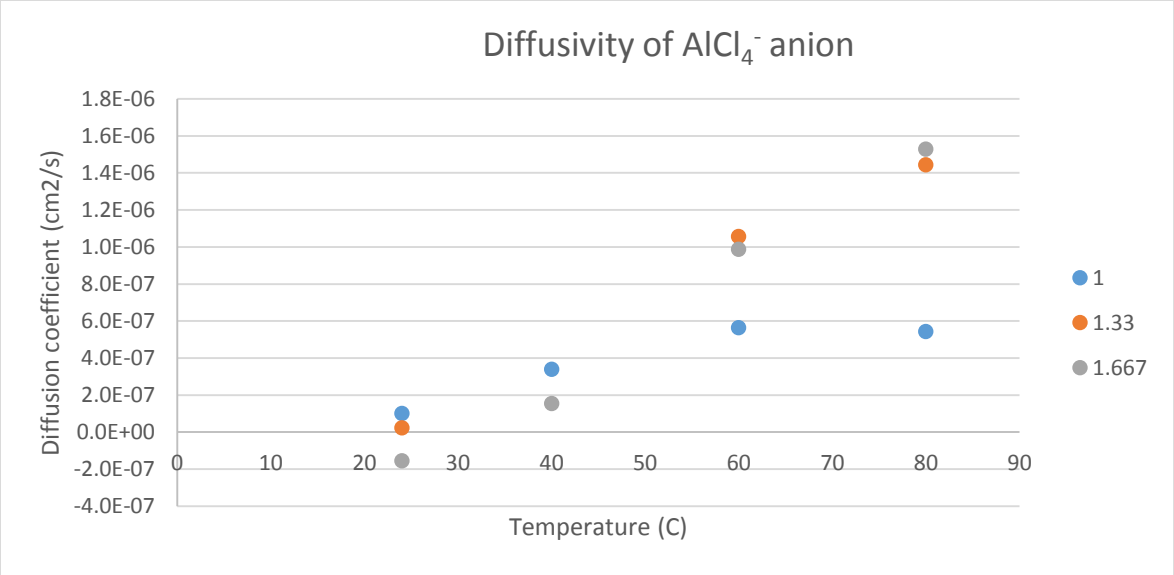

Figure 78: $AlCl_4^-$ Diffusivities

Once the concentration has been corrected for, the 1 to 1 solution actually shows the least contribution from the $AlCl_4^-$ species at higher temperatures. The intermediate concentrations show approximately linear increase in diffusion with temperature and are relatively consistent with each other. $AlCl_4^-$ is not present in the 2 to 1 solution so it cannot participate in the conductivity. These values predict diffusivities that are in between the mobilities of the other two measured species. Since the mobility of the $AlCl_4^-$ solution is higher in the mixed chemistries than in the 1 to 1 solution it indicates that it is not interacting with the $Al_2Cl_7^-$.

Electron structure theory modelling was done to look more closely at the reasoning for such variable diffusivities. Since the total conductivity is not necessarily a direct combination of the mobilities of the ions in solution and their concentration the mobility $AlCl_4^-$ species is difficult to directly determine. Using density functional theory to model the ionic structures it is possible to get size ratios of the components and an approximation of the mobility based on a comparison. This will also allow for

approximations of the theoretical density, which will give indications of the open volume of the solution and information on the hole type transport that is potentially important in these electrolyte systems.

6.5d Ionic Size Comparison and Mobility Differences – Gaussian

Density functional theory was done to determine the size and size ratio of the ionic species in solution. The size ratios are a method to determine the probability of motion, as the $AlCl_4^-$ anionic species mobility is not easily measured, doing a theoretical size comparison gives insight to its mobility. Molecular mechanics of solutions this would require significant effort, but the size analysis alone verifies the size discrepancy between ions and validates the varied mobilities as well as the high contribution of the smaller cationic species to the conductivity of the solution. The predicted optimized low energy configurations are shown in the next Figure 79.

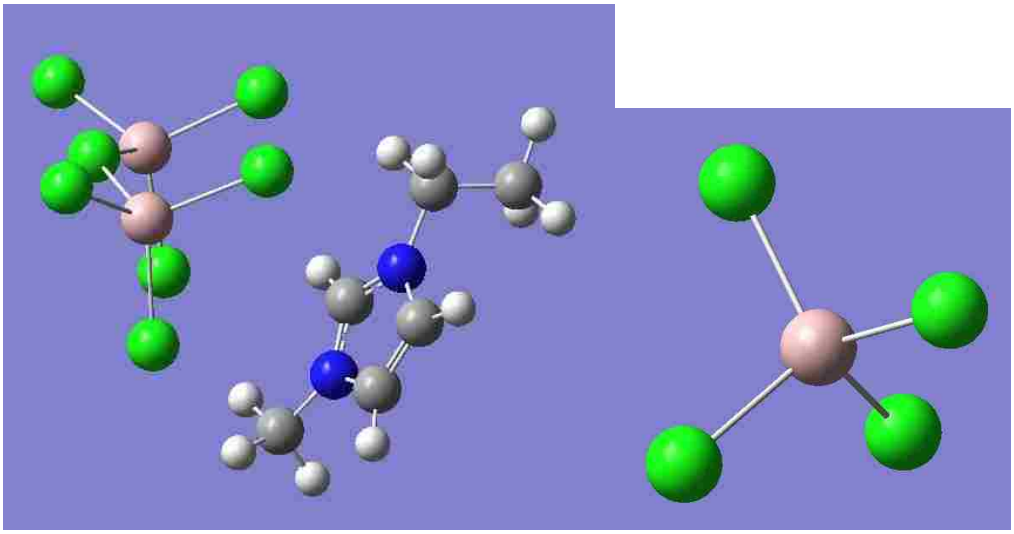

Figure 79: DFT Modelling EMImCl $AlCl_3$ Ionic Components

The actual density divided by theoretical density gives an approximation of the filled space in the solution, and the difference indicates the amount of free space, leading to holes in the solution that allow for hole type transport. Using Gaussian with DFT B3PW91 method and 6-311G basis set with "tight" restrictions to volume calculations the theoretical volume and predicted solvation radii of the cationic and anionic species were determined, these values are shown in Table 2: Ionic Size Calculations. These simulations did not give identical results but the convergence tolerance could not be set to any tighter constraints. To correct for the variation, the simulations were run repeatedly until the resulting data gave a standard deviation of below 5%.

Table 2: Ionic Size Calculations

	$Al_2Cl_7^-$	$AlCl_4^-$	EMIm+
Stokes radius (A)	5.004	4.33	4.14
Volume (cm^3)	2.88E-22	1.76E-22	1.52E-22
Normalized values	$Al_2Cl_7^-$	$AlCl_4^-$	$EMIm^+$
Stokes radius	1	0.87	0.83
Volume	1	0.61	0.53

Simulations of multiple ions together were optimized to minimum energy conditions and the volume was calculated and in call cases the volume was consistent to additions of the individual ionic species volumes in combination, so there were no shown effects of ionic interactions affecting the theoretical density. Using the solution concentrations and the theoretical volume of each ion the theoretical density of the solution was calculated. The theoretical and experimental densities are shown in Figure 80 for comparison.

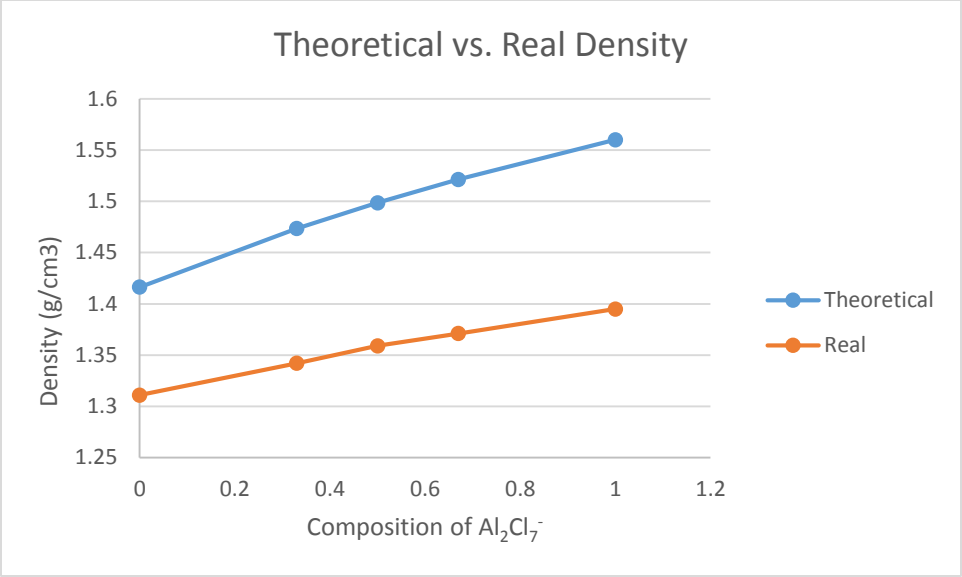

Figure 80: Density Comparison, Theoretical vs. Real

The ratio of theoretical density to experimentally measured density is shown in Figure 81, and this is a representation of the free volume between ions in solution, and is considered a strong indicator of transport properties of the components in solution.

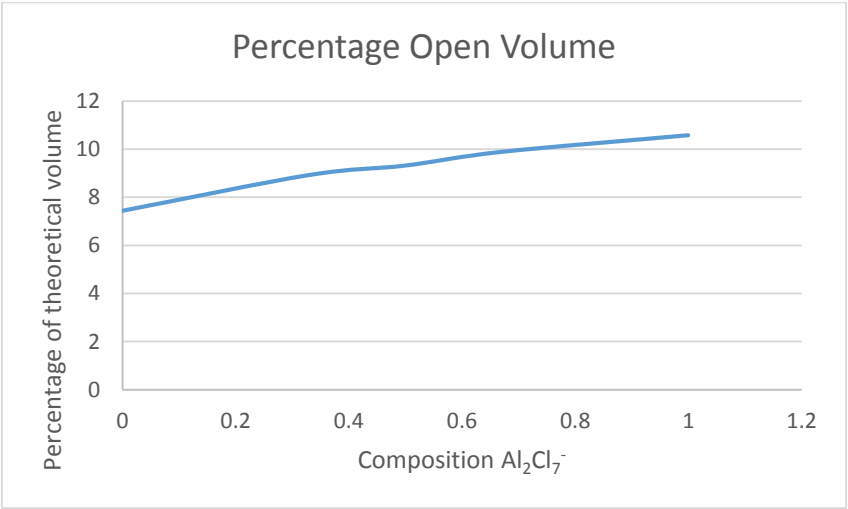

Figure 81: Theoretical Open Volume of EMImCl $AlCl_3$ Ionic Liquids

The percentage open volume increases with increasing $AlCl_3$ concentration, these values are likely underestimated as there is some overestimation of ionic volume built

into the modelling software to be more representative of real systems, but the trend will be consistent. This theoretical density calculation for volume does not relate to the decreasing conductivity with increasing composition, as the trends should be the opposite of observed. Therefore, the hole mobility mechanism does not affect the mobility of the $EMIm^+$ cations. The larger $Al_2Cl_7^-$ species diffusion increases with composition shifts and may be influenced by the increased open volume. The observed decreasing viscosity trend with increasing $AlCl_3$ content may be attributed to increasing hole volume competing with increasing ionic size, and levels back to the 1 to 1 composition viscosity value by the time the 2 to 1 composition is reached. It is evident from the conductivity, viscosity and diffusivity data that there are unequal contributions from the various ions.

6.6 EMImCl $AlCl_3$ IL Electrolytes Summary

It is clear that viscosity is well correlated to the mobility of the $Al_2Cl_7^-$ anion. To investigate the shift in mobility that may be associated with the shear thinning of the electrolyte, the viscosity in the static regime was determined and compared to the reduced viscosity due to shear thinning. The viscosity in the shear regime, as well as the mobilities in the static (Cottrell) and dynamic (Levich) conditions have been calculated. Falling ball measurements were done to find the viscosity in zero shear conditions, and the stokes calculated viscosities from the falling ball experiments were variable between electrolyte compositions but may still be valuable as predictions of low shear viscosity. The spheres interact differently with the solutions depending on the Lewis acidity and this appears to strongly influence the mobility and therefore the viscosity measurement as a whole, this data is shown in Figure 82.

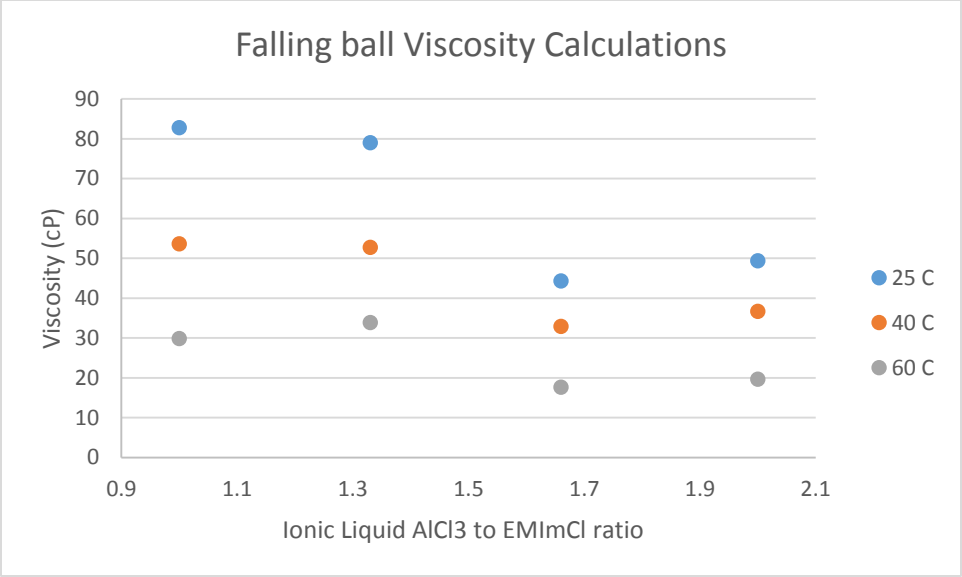

Figure 82: Zero Shear Viscosity Measurements

The more acidic solutions show significantly lower viscosities; this may be accurate but may require more testing to show they are not strongly influenced by particle electrolyte interactions. Measuring the viscosity in a static electrolyte with the falling ball technique showed a significant decrease in viscosity with increasing temperature in all cases. The temperature dependence of the viscosity in each solution is used assuming that the particle-electrolyte interactions are also consistent. The falling ball measurements were made to elucidate the variance in $Al_2Cl_7^-$ mobility between static and dynamic conditions. For this comparison, Figure 83 again shows the ratio of increase in $Al_2Cl_7^-$ mobility from static to dynamic regimes, and Figure 84 shows the ratio of decrease of viscosity from static measurements to dynamic measurements.

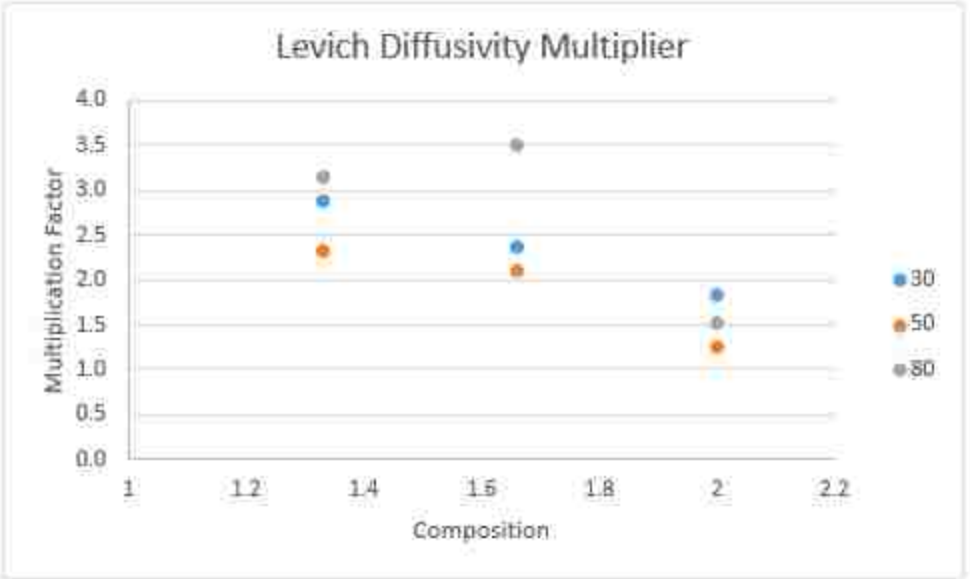

Figure 83: Increase in Diffusion From Static to Dynamic Measurements

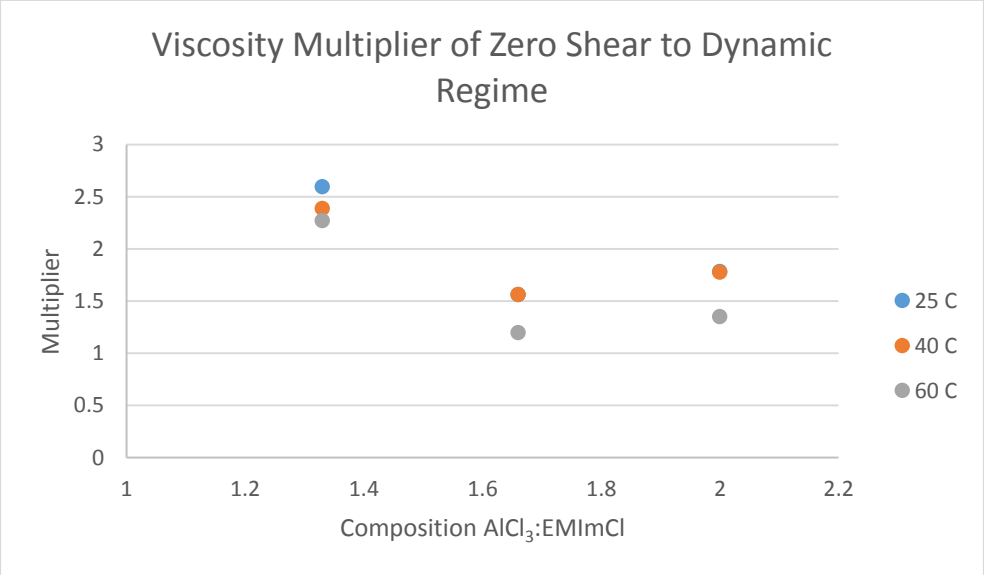

Figure 84: Viscosity Change from Static to Dynamic Conditions

It is evident that the two are closely related as the changing viscosity again correlates to increasing $Al_2Cl_7^-$ mobility.

Comparing the conductivity to viscosity shows discrepancies, the viscosity has a peak at the 4 to 3 ratio electrolyte and then decreases, while the conductivity decreases over the entire composition regime, shown in Figure 85.

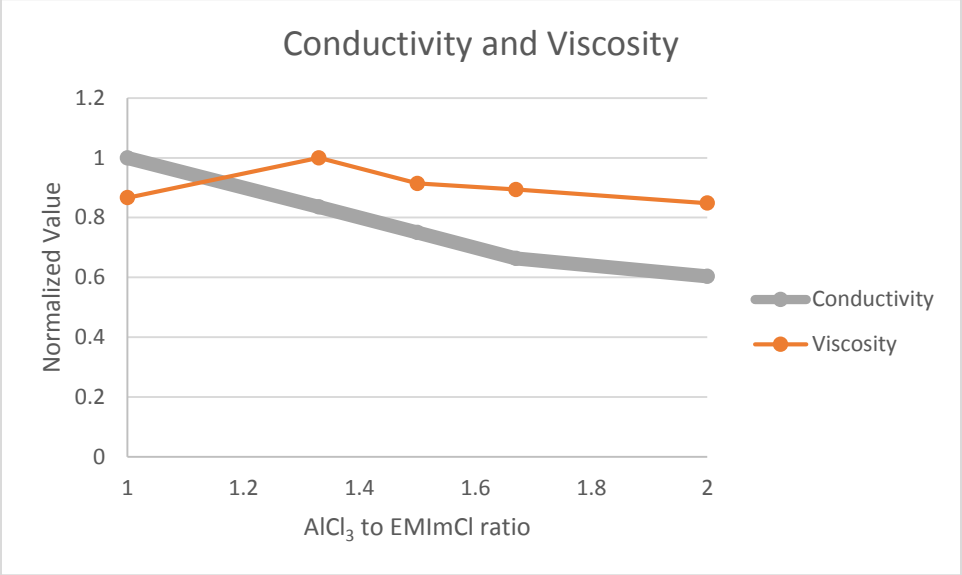

Figure 85: Conductivity and Viscosity Comparison

These two qualities should be inversely correlated and are not, indicating that there are different mechanisms dictating the trends in each. The decreasing viscosity at increasing $AlCl_3$ compositions does not match the mobility trends of the smaller $AlCl_4^-$ and $EMIm^+$ species in solution. It does show a strong correlation to anionic $Al_2Cl_7^-$ motion. This demonstrates that this trend of viscosity is dictated by the $Al_2Cl_7^-$ anion, and separately, the conductivity is determined from the smaller species that are more mobile. The mobility of $Al_2Cl_7^-$ and viscosity are related, and shear forces that decrease the viscosity are expected to increase the $Al_2Cl_7^-$ diffusion.

Chapter 7: Particle Incorporation and Testing – SEM, EDS, DSC

The deposition characteristics of aluminum in different electrolyte compositions was thoroughly explored and codeposition began. Initially codeposition was performed in the optimized low temperature conditions, in the 50% diluted toluene BMImCl chemistry with 50g/L Ni particulates. This was to test the incorporation properties and would allow us to modify the electrolyte to accommodate the codeposition process.

7.1 Incorporation onto Rotating Disk Electrodes

While the aluminum deposition was smooth and compact, there was no particle incorporation under any conditions using the RDE alone. Incorporating NIB magnets behind the electrode enhanced the attraction of particles to the electrode and ultimately led to particle incorporation. The particles incorporated under these conditions were loosely agglomerated and incorporation quantity was lower than the stoichiometric target of 40% nickel by volume. These were expected outcomes because the particles were only weakly attracted to the surface and the target high particle loading is difficult to achieve without significant optimization. The incorporation values that were achieved were enough to test the interface of the particulates in the deposited matrix and also test for calorific output. A EDS map of a FIB cross section of the codeposited film are shown in Figure 86.

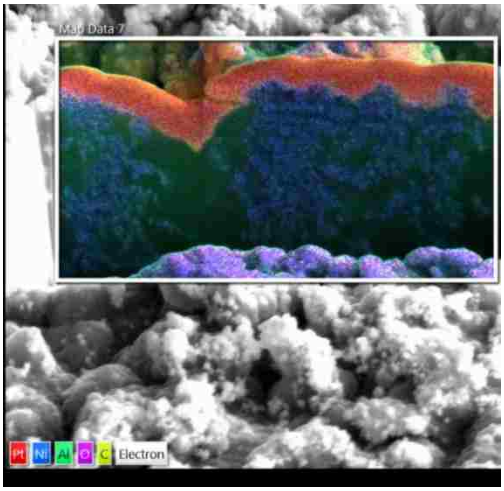

Figure 86: SEM and Elemental Analysis of Codeposited Film

The SEM image with EDS mapping shows particle incorporation in the ~10%. The film was tested for energetic alloying with differential scanning calorimetry. The data indicates that there is indeed aluminum and nickel present in the codeposited films. The DSC plot is shown in Figure 87 and the nanofoil film is shown as an ideal comparison.

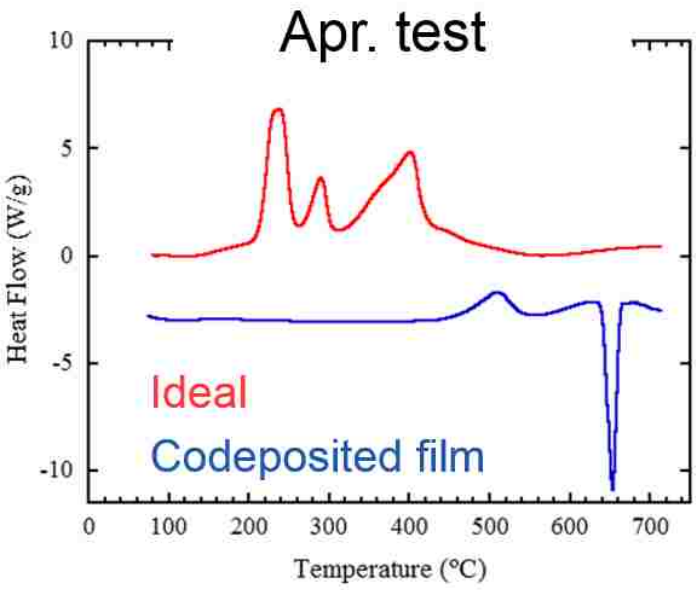

Figure 87: Calorific Output of Initial Codeposited Film

The large endotherm at 660˚ C is the melting point of aluminum and the absorption of aluminum from the large excess remaining of the pure metal. The shift to higher temperatures for the initiation of the exothermic reaction is possibly due to a native oxide on the nickel particles that were incorporated. At this point there was no chemical cleaning done specifically to remove this oxide. It should be attacked by the Lewis acidic electrolyte chemistry. The shift and poor stoichiometry may also be due to larger particle sizes than optimal or agglomeration of the particles in the incorporation. This is in correlation with the limited calorific output, and indicates among other things the non-optimized stoichiometric ratios of reactants. Incorporating particles require significant increase in attractive forces and switching to sedimentary codeposition conditions was utilized to improve incorporation volumes.

7.2 Increase Incorporation with Sedimentary Codeposition

The stoichiometric ratio was improved with a shift to sedimentary codeposition, the reaction vessel is shown in Figure 88.

Figure 88: First Generation Sedimentary Deposition Reaction Vessel

The deposition became much more complicated as particles tend to accumulate on the surface, and the films became porous and low quality as seen in Figure 89.

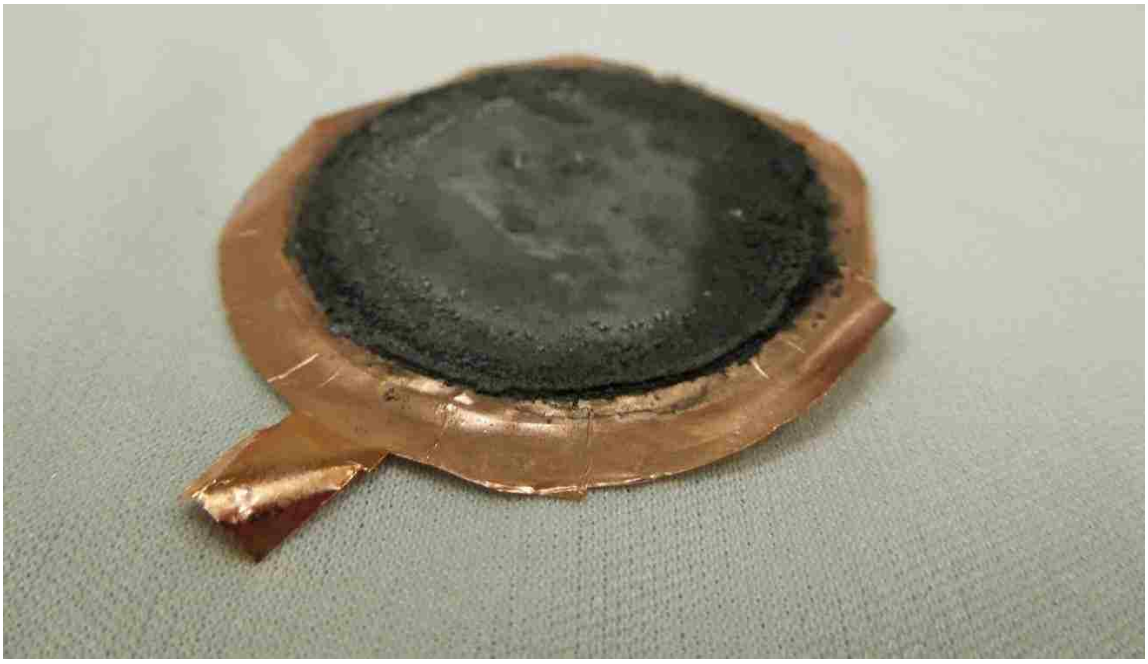

Figure 89: Film Deposited in Sedimentary Reaction Vessel

The DSC test was much improved and was approaching roughly half of the expected energetics, Figure 90.

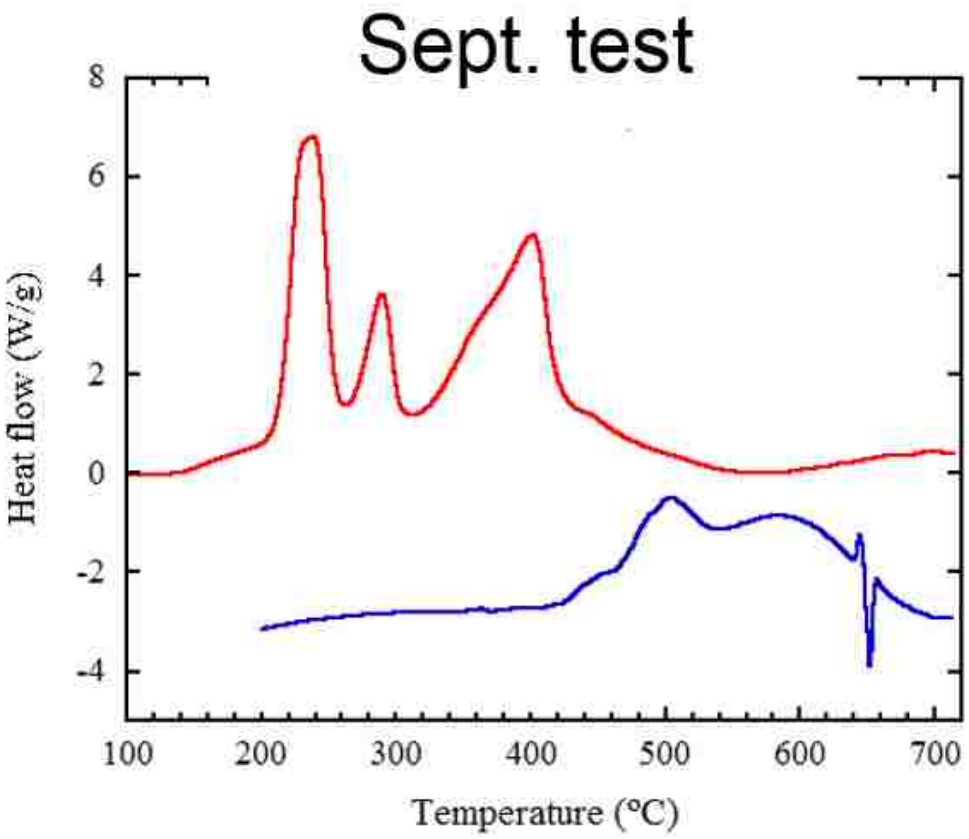

Figure 90: Calorific Output of Sedimentary Codeposited Film

There is still a significant shift toward higher temperatures but not as drastic as the previous test. There is also the remaining aluminum endotherm but this is also diminished when compared to the previous test, indicating better reaction stoichiometry. Improving the aluminum deposition quality was the driving force of further investigation of the electrolyte properties and the development of the new reaction vessel and optimized parameters.

7.3 Decrease Agglomeration with Surfactants

There was a significant problem with particle flocculation in regimes that allowed for sedimentary codeposition. These agglomerrations of particles become quite large, on the order of 100 um as shown in Figure 91.

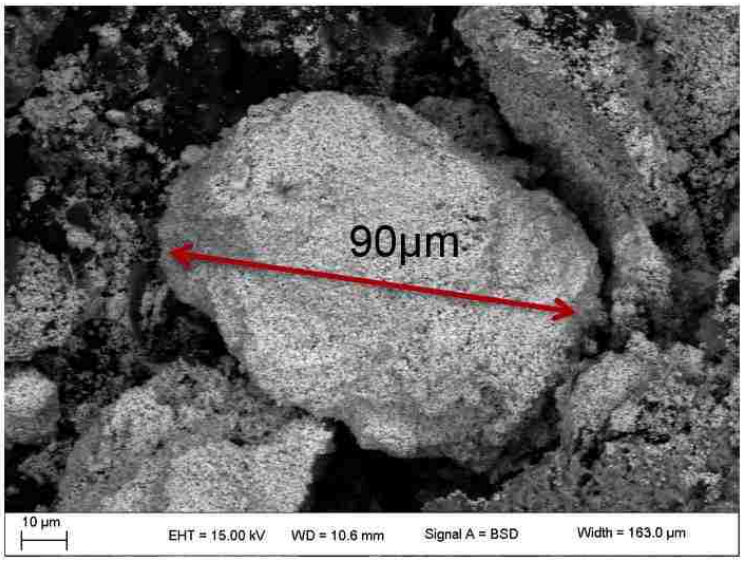

Figure 91: SEM of Agglomerated Particles in Sedimentary Deposition Vessel

A variety of surfactants were looked into to mitigate these agglometrations and improve stable colloidal solutions. These were predominately surfactants that have been used in aqueous solutions and the first step was to test the solubility and chemical compatibility with the ionic liquid. The solubility of tartaric acid diammoinium salt was very low and ethylene diamin tetraacetic acid had no solubility. Sodium dodecyl sulfate, Centronium Bromide, saccharin and sodium saccharin salt all have solubility that meet the criteria as a pass (>2wt%). Oleic acid is liquid and seems to be miscible in the ionic solution as well. Cyclic voltammetrically testing these mixtures in nuetral ionic liquids that are not electrochemically reducible in the window tested will verify if they are electrochemically stable in the needed range, the results are shown in Figure 92.

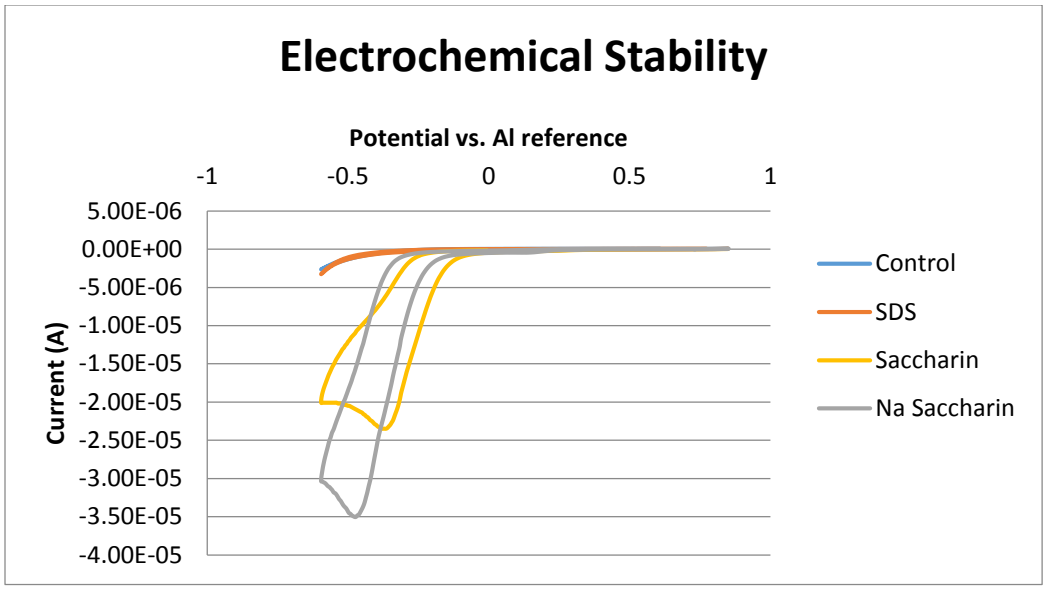

Figure 92: Electrochemical Compatibility Tests of Surfactants in Ionic Liquids

Both saccharrin components failed this test but all other systems matched the control, indicating that they did not add any contribution to the reduction within the range used for depositing aluminum.

The actual surfactant properties were difficult to test, the usual tool for measuring colloidal stability relies on measuring the surface charge of the particles in solution. It is assumed with enough surface charge the particles will repel each other and the resulting solution will be free of particle agglomeration. Some calibration data of an aqueous solution and chitosan particles is shown in Figure 93 as model data.

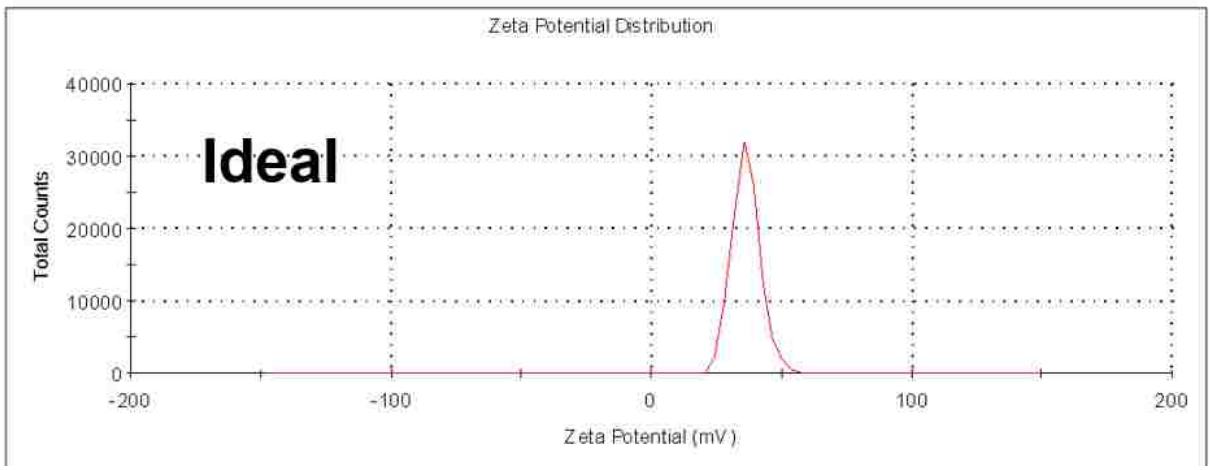

Figure 93: Zeta potential of Chitosan Nanoparticles in Aqueous Solution

It is apparent that the peak is well resolved, with a maximum count of around 30000. These are non-conducting particles in a well understood aqueous medium. In contrast, the data derived from running the same tool on the ionic liquid solution and Nickel particles shows no resolution even at much greater count numbers, Figure 94. This is caused by either the ionic nature of the electrolyte or the conductive properties of the particles. Changing either of these would lead to data that was not relatable to our current system, so implementing a control for correlations was not possible and other options were looked into.

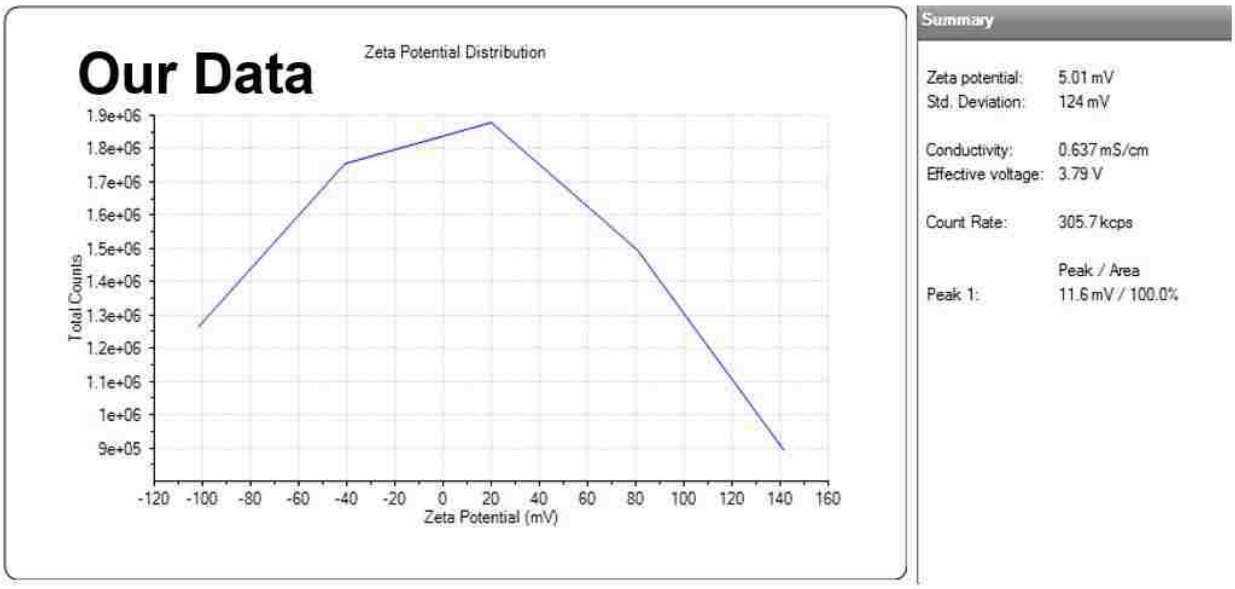

Figure 94: Zeta Potential Measurement of Nickel Particles in Toluene Diluted Ionic Liquid

To test if the solution was stabilized, particles were mixed in uniform ionic liquid solutions each containing different surfactants and compared against a control solution without surfactants. The solutions were checked at regular times to see if the surfactants had any effect on settling rate. It was determined that there was little to no effect with any surfactants, likely they do not contribute to surface charging in a significant way in the strongly ionic medium. Measuring the particle settling was attempted with a quartz crystal microbalance but the frequency shifts of the quartz due to particle settling was very small and undetectable. Since the particles were only settling on the surface and not being incorporated onto it the mass change was negligible and the microbalance was only measuring the change in viscosity in the solution due to particle presence. The continuing increase of particles at the surface with increased settling would likely influence the viscosity further but determining this dependence would take another endeavor into properties that was beyond the scope of this work.

The particles can be separated with physical agitation and are temporarily stable in the ionic liquid, partially due to the relatively high viscosity.

7.4 Improve Plating with Reactor Design – COMSOL

Physical agitation is the best approach to suspending the particles in solution. This is achieved without affecting the plating conditions by implementing a separate reservoir that has a stir bar and the fluid flow into the reaction vessel is basically unperturbed from these conditions. A reaction vessel where the codeposition occurs was designed with an impinging jet fluid flow to replicate conditions of the rotating disk electrode as closely as possible with an increased area allowing for larger films to be produced. The reactor vessel continues to use sedimentary deposition techniques to improve incorporation as gravity assists particle motion to the electrode surface. The reaction vessel and separate reservoir is shown in Figure 95 and Figure 96. The tubing and materials were tested by immersion in the electrolyte and testing both for color changes and details are shown in Appendix B. Viton tubing and Teflon were the materials of choice for chemical and temperature compatibility.

Figure 95: Electrodeposition Reaction Vessel

Figure 96: Two Chamber Reaction Vessel for Controlled Solution Flow and Solution Mixing

7.4a Modelling CFD and Particle Tracing

It is crucial to understand the viscosity and reaction properties in order to optimize the arrival rate of particles as well as optimize the electrochemical reduction of the matrix. These properties can be modelled with multiphysics software, which is utilized to determine computed fluid dynamics and particle motion in the system. Some representative solutions of the system are shown in Figure 97.

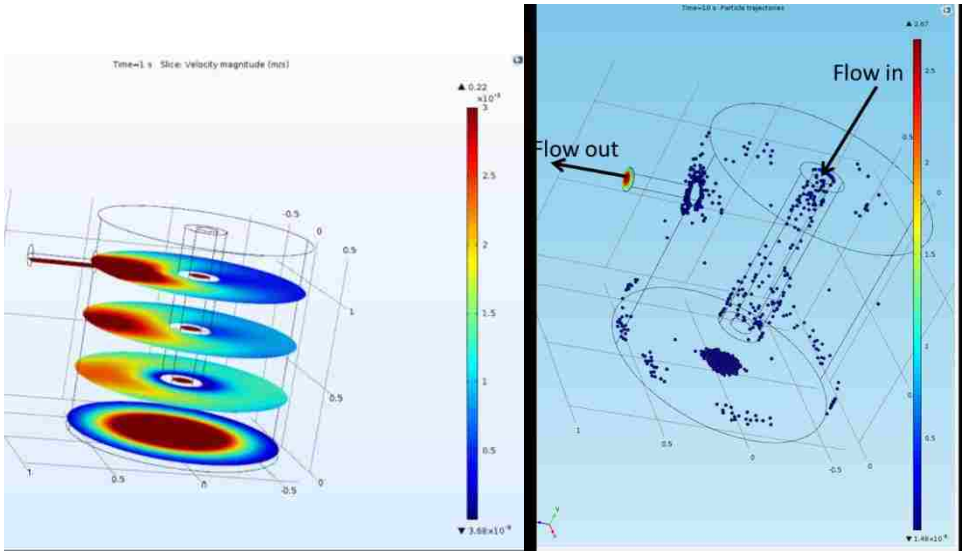

Figure 97: Comsol CFD and Particle Tracing in Reaction Vessel

The fluid flow follows a consistent path in each model tested, with increasing velocities as the flow rate is increased. In all cases the electrolyte enters the reaction vessel and impinges on the electrode surface before spreading out uniformly and making its way towards the outlet. Particle tracing in the system shows that at high flow rates of >100 mL/min roughly half the particles come into direct contact with the electrode center but are swiftly sheared away. The lower flow rates from 3-10 mL/min show particles following the bulk solution flow and no electrode contact, while intermediate conditions show intermediate results, increasing contact quantity with flow rate but also increasing

shear at the surface. Increasing the forces to bring particles to the surface without increasing flow rate will be important, and the assistance due to gravity in sedimentary codeposition may not be enough. Magnetic attraction was under initial investigations and was showed to be promising results.

The only forces that act on the particles that we have control over are the shear due to agitation, gravity and possibly magnetic attraction. Agitation is utilized to bring particles to the electrode but is also the key factor that removes them. It is required to utilize gravity as much as possible by reducing the fluid flow and adjusting the particle loading. This will ensure that the correct number of particles make it to the surface. The optimization is required so that the particle arrival rate matches the matrix growth rate, as the arrival of too many particles will lead to a spongy porous film, and not enough particles will give low loading. The deposition rate is determined by the residence time of particles on the electrode, as the nanoparticles have limited time to be incorporated before being removed by electrolyte flow. The low flow leads to high diffusion distances of the aluminum precursors, and the diffusion rate and replenishment are important to note. The conditions were determined from the RDE data, which details the deposition regime based on fluid flow. Ensuring that the regime is not diffusion limited is paramount to generating a quality film, and the agitation can be calculated to ensure significant overhead and solution replenishment. Comsol modelling was used to determine the probability of particles coming into contact with the electrode, the non-Newtonian fluid flow was simulated at different flow rates with 100 particles initially dispersed at the beginning of the simulation. The number of particles that interacted with the electrode

was strongly dependent on flow rate, with more particles contacting the surface with increased flow rates but also significantly higher shear rates under these conditions.

Chapter 8: Intermetallic Alloying and Passivation – TEM

Comparisons are made between the electrochemically produced film and the commercial PVD film. These are characterized by energy release and interphase size. The high interfacial area of these films is subject to atomic diffusion which can reduce the burn characteristics. TEM analysis of the interfacial layers seems to indicate that the lower temperature process associated with codeposition can reduce this pre-reaction mixing, and is equivalent or better than the sputtered films in our first deposition attempt. Accelerated aging is being performed on film from both fabrication methods and increased temperature heavily influences interatomic mixing. TEM of the nickel particle and aluminum interface are shown in Figure 98 and the Spectrum is shown in Figure 99.

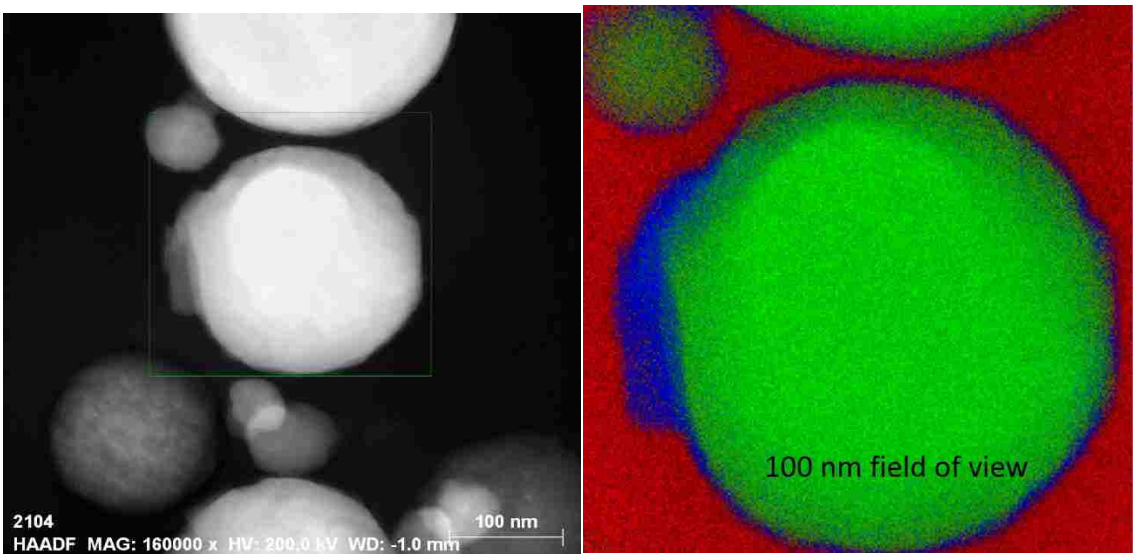

Figure 98: TEM and Elemental Mapping of a Particle Codeposited in Aluminum Film

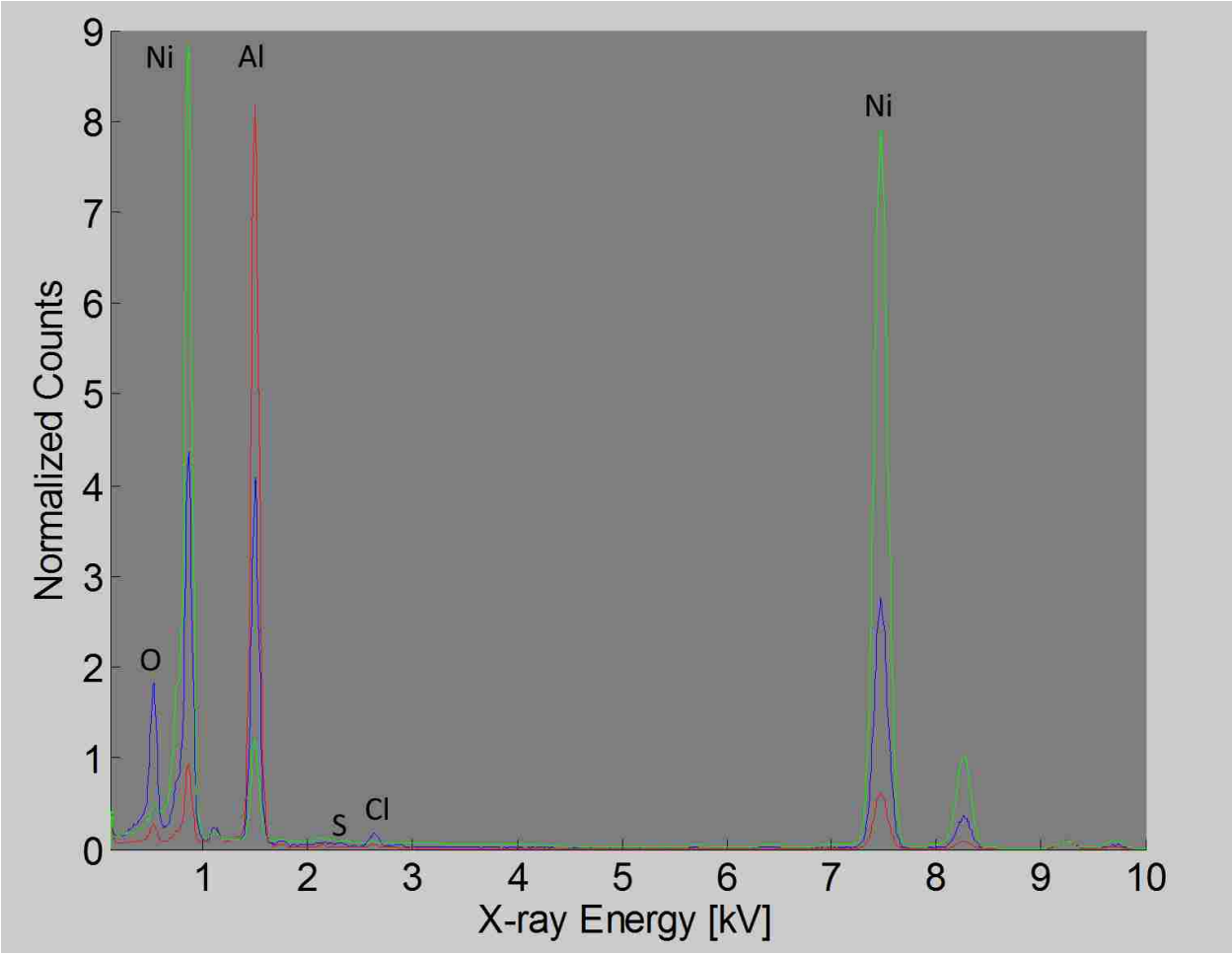

Figure 99: Elemental Spectrum of Codeposited Particle and Interface with Electrodeposited Aluminum

The interface shows slight mixing of the aluminum and nickel at the interface as well as some oxygen impurity which is likely why the energetic output is shifted towards initiating at higher temperatures.

Chapter 9: Conclusions

The aim of this project was to codeposit an energetic thin film, with aluminum matrix and nickel nanoparticle inclusions. The codeposition process is complicated with variables including particles size, particle loading, electrolyte choice, plating parameters and fluid flow. The flow is determined by the electrolyte viscosity and reactor design, where the viscosity depends on composition and temperature. The nanoscale particles in this project have very high shear forces because of their high surface area and low mass, which decreases their residence time on the electrode surface. This necessitates maximizing the forces that bring them into contact with the electrode and minimizing shear forces that quickly remove them before they can become entrapped. The particles are conductive and it is important that they not accumulate on the electrode at more than monolayer thicknesses, as this leads to porous and spongy coatings. This necessitates control over the fluid dynamics and matrix growth. The aluminum deposition is central to the codeposition process, where the growth rate must be high enough to entrap particles but balanced with their arrival rate, to increase the volume percent of the particles. The presence of electroactive species at the electrode must be sufficient to supply whatever growth rate is needed, and the reaction kinetics and diffusion were investigated in full.

Initial solutions tested included aprotic solvents and aromatics. Most aprotic solutions were difficult to work with due to high volatility and reactive components. The aromatics required significant additions of complexing salts such as KBr but gave low rate deposition, although they were easier to work with than the higher volatility THF baths.

A handful of ionic liquid electrolytes were looked at, and the imidazolium chloroaluminates showed the most promise with large electrochemical windows, high aluminum precursor concentration, chemical stability and low vapor pressures. The TFSA electrolytes were more expensive and complicated without benefit. The dicyanimide electrolyte was looked at because of its high conductivity and low viscosity but the complex was reactive with aluminum and was not capable of aluminum deposition.

BMImCl and $AlCl_3$ solutions were tested with dilution agents. The speciation of the aluminum complex was verified with NMR and is solely dependent on composition and independent of temperature. Toluene and dichlorobenzene were used as co-solvents and were found to be suitably chemically inert, while ethylene carbonate influenced the chemistry significantly. Both aromatic co-solvents impart much lower viscosity to the ionic liquid electrolyte vs. the neat solution, and in doing so change the properties dramatically. The solutions were tested at varying overpotentials to examine the deposit morphology and purity. Optimum deposition at room temperature was found at -600 mV vs. Al QRE, increasing the overpotential to -1000 mV resulted in breakdown of the electrolyte and impurity incorporation, specifically chlorine. The deposits from these solutions also became dendritic and dark, especially around the edges. Deposition at -1500 mV continued this trend, and the electrolyte breakdown lead to large quantities of chlorine and carbon in the deposit. Additions of dilution agents improved the deposit quality and smoothness while cutting the electrolyte cost. Increasing the co-solvent also lowers the deposition rate since the precursor concentration decreases.

Once a range of working solutions were found, ionic mobility and conductivity were tested to find the optimal electrolyte for deposition. The diffusivity increases continually with co-solvent addition and the ionic carrier concentration is decreases, resulting in a maximum in the conductivity. This maximum of conductivity was confirmed to be the best plating chemistry, although further dilutions give suitable deposits and a lower cost per unit volume, with decreasing plating rate.

Rotating disk electrode tests at room temperature on the neat $BMIm^+$ $Al_2Cl_7^-$ solution show kinetic limitations at roughly 10 mA/cm^2 and minimal dependence on diffusion limitations. The Tafel behavior of the reaction shows that the charge transfer coefficient was 10^{-8} mA/cm^2, which is quite slow. Even at the low overpotential range, the nucleation properties were found to still be very much instantaneous. At low or no agitation, the diffusion rates are slow and distances are high, potentially explaining the constant instantaneous nucleation result even though most tests in dynamic systems are kinetically limited. The instantaneous results also indicate that the overpotential for continuing deposition on a metal substrate is lower than the carbon electrode. This has significant impact on particle deposition, as the conductive particles are much more likely to be coated when in contact with the electrode than the matrix growth around from a carbon electrode surface.

Increasing the deposition rate can be accomplished by increasing temperature. The static condition diffusion rates were determined with chronoamperommetry and the Cottrell equation and showed trends of increasing diffusion with temperature and $AlCl_3$ composition. Dynamic conditions were investigated with the rotating disc electrode. The EMImCl $AlCl_3$ ionic liquid system was tested at varying compositions and temperatures,

which change the ionic concentration, density and viscosity. The density and rheology of all EMImCl $AlCl_3$ solutions at temperatures from 25-80˚ C was investigated for use in electrochemical measurements. These solutions were found to be shear thinning. The rotating disk electrode was capable of measuring the diffusion and kinetic limitations under most of the conditions. The lower concentration aluminum electrolytes show pure diffusion limitations at low temperatures and low shear rates, while increasing the aluminum concentration as well as increasing rotation rates lead to either mixed kinetic and diffusion limitations or purely kinetic limitations. Increasing the temperature increases both the diffusion rate and reaction kinetics, but it increases the reaction rate more so. The diffusivities calculated from the Levich equation under shear conditions were always higher than the diffusivities calculated in the static conditions in the same electrolyte and at the temperature.

The increased viscosity and low mobility of the $Al_2Cl_7^-$ species was thought to be attributed to an anionic interaction, since it only occurred in the mixed anionic species solutions. The mobility of the $AlCl_4^-$ species would also be retarded in this case, so it was determined through 2 more experiments. The conductivity is based on the Nernst-Einstein equation and is an accumulation of the concentration and mobilities of all ions in solution. The conductivity increases linearly with temperature and decreases with $AlCl_3$ content. This is the opposing trend compared to $Al_2Cl_7^-$ mobility and viscosity. The mobility of the cationic species was directly measured with PGSE over changing temperatures and composition. These results showed increase over the range of 25 to 80˚ C and no trend based on composition, indicating the cation did not coordinate more strongly with either anionic species and the structure was not changing significantly

enough to impact its mobility. The mobility of the cationic species is up to 40 times higher than the $Al_2Cl_7^-$ anion, and contributes much more strongly to the conductivity. The $AlCl_4^-$ anionic species mobility was calculated by subtracting the contributions of the imidazolium and $Al_2Cl_7^-$ determined from PGSE and Cottrell, respectively, from the experimentally determined conductivity. The $AlCl_4^-$ diffusion is the lowest at the pure EMIm and $AlCl_4^-$ solution, which was not expected and indicates it likely does not coordinated strongly with the $Al_2Cl_7^-$. Its mobility was found to be much higher than the $Al_2Cl_7^-$, but is still lower than the cationic species. The viscosity and $Al_2Cl_7^-$ complex is significantly correlated, as the viscosity and $Al_2Cl_7^-$ trend similarly with changes in composition whereas the other components do not match. The mobility of the $Al_2Cl_7^-$ is certainly much lower than the cationic species, clarifying the minimal contribution of the large ion to conductivity, where the $EMIm^+$ and $AlCl_4^-$ contributions dominate.

Gaussian was used for density functional theory molecular optimizations, and based on size comparisons of the ions the stokes size of the $AlCl_4^-$ is 10% larger than the cationic species and only 60% the size of the larger anion, verifying that it's mobility is should be similar to the cation. The theoretical density of the solution was calculated and compared to the experimentally measured density, giving insight into the open volume. This trends toward increasing open volume with increasing $AlCl_3$, and the increase in viscosity in the mixed solutions can be attributed to two competing trends, increasing ionic size as more $Al_2Cl_7^-$ is produced and increasing open volume that allows for more ionic motion. The larger $Al_2Cl_7^-$ species benefits more from the increasing hole volume whereas the smaller ions are free to move in the smaller holes present in the lower

concentration solution. This is the reasoning for consistent mobility of the $EMIm^+$ in all compositions.

The viscosity decreases with shear, and this is likely due to breaking up of electrostatic attractions in solution. The mobility of the $Al_2Cl_7^-$ species increases with the decreasing viscosity, potentially from reduced resistance from ionic attractions or increased probability of interacting with an open volume large enough to traverse. These trends clearly show that the cationic mobility and $AlCl_4^-$ contribute to the conductivity and the $Al_2Cl_7^-$ influences the viscosity, and in turn, is influenced by changes in viscosity.

Particle incorporation using the RDE alone lead to no particle incorporation in pure aluminum films. Utilizing magnetic attraction allowed for increased particle residence time and incorporation around 12% by volume. Sedimentary codeposition was used to increase the residence time, but led to poor quality deposits due to particles settling and accumulating on the electrode. The films with low agitation were porous and rough but had much higher nickel content, near 20% by volume. It was apparent the particles tended to flocculate under relatively static conditions and it was also apparent that the particles would require significant optimization of the flow parameters on the electrode to balance their arrival rate and residence time.

To stabilize the colloidal solutions, many surfactants were tested for solubility and electrochemical stability and it was determined that the surfactants that passed preliminary chemical compatibility testing still had no measurable effect in the ionic liquid system. The chosen method to keep particles suspended in solution was to have sufficient agitation to separate the particles from each other. To allow for the physical agitation required to keep the particles separated and also the control of the flow over the

electrode the reactor vessel was broken up into two components, one to stir the solution and keep it well mixed and one to deliver the electrolyte and particles in a controlled manner onto the electrode.

The second chamber was designed to bring particles directly to the cathode surface and spread them uniformly so they could be incorporated in the growing aluminum film. This is a complex system as the faster flow rates bring more particles to the surface while also decreasing their residence time and removing them from the surface. The balance of particle arrival and the electrodeposition parameters is vital, and the flow parameters were modelled with Comsol CFD simulations to determine particle motion. The particle tracing module shows that at high flow rates of >100 mL/min in our system roughly half the particles come into direct contact with the electrode center but are swiftly sheared away. The lower flow rates, from 3-10 mL/min show particles following the bulk solution flow and minimal electrode contact. Increasing the forces to bring particles to the surface without increasing flow rate will be important, and the assistance due to gravity in sedimentary codeposition may not be enough. Magnetic attraction was under initial investigations and was shown to be promising.

Optimization of the flow and electrolyte system could easily be done with the information found in this project, further testing that needs to be accomplished would be more tests in the reaction vessel to determine Langmuir absorption constants and better approximations of the particle critical residence time. Higher temperature solutions with dilution agents can be implemented, as well as magnetic forces to increase the particle residence time and attraction to the electrode surface. Based on the kinetics of the tested

EMImCl chemistry at 80˚ C the codeposited film growth rate could reach as high as 150 µm/hour.

Differential scanning calorific output of the codeposited films showed exothermic properties, with low roughly half the heat of the ideal film due to lower than desired nickel content. The temperature of activation is shifted towards higher temperatures as most likely due to a native nickel oxide on the particles, decreasing the interfacial interaction. Testing the particles that were incorporated with TEM showed they have similar interaction distance between the different metals when compared the PVD films, which is deemed acceptable and methods are under review for decreasing or remove the oxide formation.

Appendices

Appendix A: Nucleation and Growth Mode Testing

It has been reported that the nucleation model in ILs is instantaneous [86, 93], likely due to the low diffusion rates and possible effects of the aluminum precursor being negatively charged. The nucleation was studied as described in chapter 2, and the instantaneous growth mode was present under all circumstances tested involving a 2:1 IL composition at different dilutions with toluene and dichlorobenzene dilution agents. This growth mode may shift to progressive at lower $AlCl_3$ ratios (below 1.5:1) or with high additions of LiCl (<10%) [102]. The tests in the literature are generally at several hundred mV of overpotential [136], so testing lower values was performed, as the decreased kinetic rate may have shifted the regime toward more progressive modes. This was not the case. A selected set of results are shown below (Figure 100) compared to the theoretical models of progressive and instant nucleation, they are clearly instantaneous [136].

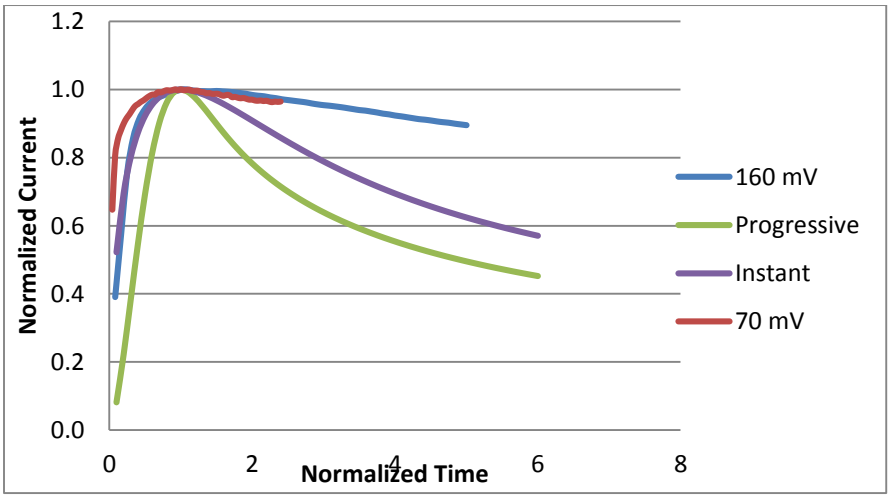

Figure 100: Nucleation Testing at Low Overpotentials

Under these static conditions, the diffusion rates were slow and diffusion distances were high, potentially explaining the constant instantaneous nucleation results seen here, even though most tests in dynamic systems were kinetically limited.

Appendix B: Material Compatibility

The fluid in the reactor vessel is pumped with a Cole-Parmer Masterflex peristaltic system. The tubing must be temperature capable and chemically compatible with the ionic liquids up to 100 C. Most of the chemically resistant tubings are only suitable to moderate temperatures, probably due to the fact they have to be malleable to compress and flow fluids. Chem-Durance has the great chemical resistance but is only suitable up to 74˚ C and Tygon only up to 57˚ C. These were ruled out and Viton (suitable to 205˚ C) and Norprene (135˚ C) were tested for chemical compatibility. They were tested by immersion in the ionic liquid. The ionic liquid before and after exposure is shown in Figure 101.

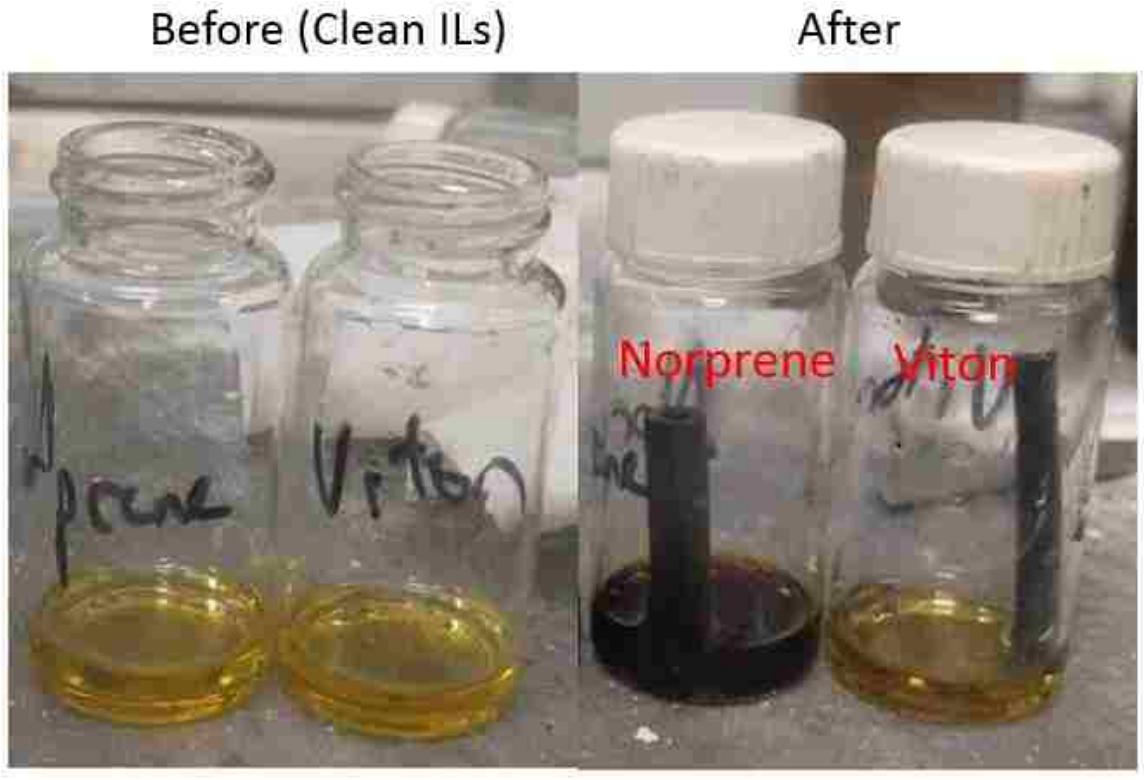

Figure 101: Norprene and Viton Compatibility Testing with Chloroaluminate ILs

It is apparent from this test that the Norprene resulted in strong color change in the ionic liquid and failed with regards to chemical compatibility. The Viton in solution showed no change to either the solution or the tubing, and was used for all further applications (reaction vessel and falling ball apparatus).

Appendix C: BMImCl ILs and Dilutions, Images/SEMs

Films deposited in neat and diluted systems were prepared and investigated with SEM and EDS, the results are shown in the proceeding section. Utilizing a more dilute, 3:2:1 Toluene:BMImCl: $AlCl_3$ solution at -600mV produced a white, dull and compact deposit with the highest plating rates measured, shown in Figure 102.

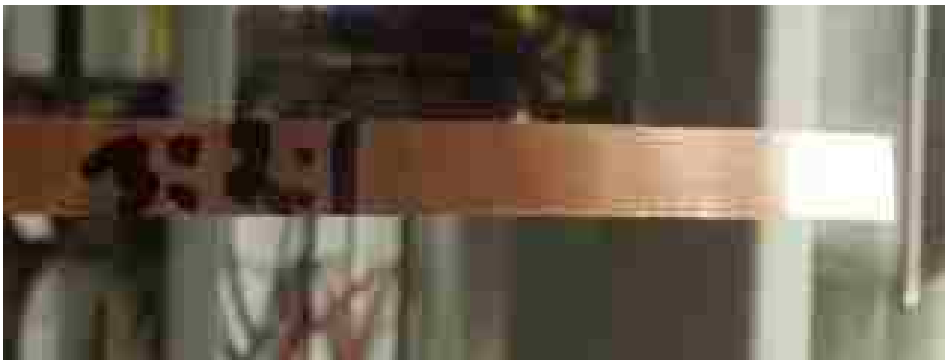

Figure 102: Aluminum Deposited on Cu in a 3:2:1 Toluene:$AlCl_3$:BMImCl Electrolyte at -600 mV vs. Al QRE

The SEM shows the relative smoothness of the deposition as well as the minor surface roughness that prevents the film from being shiny, shown in Figure 103.

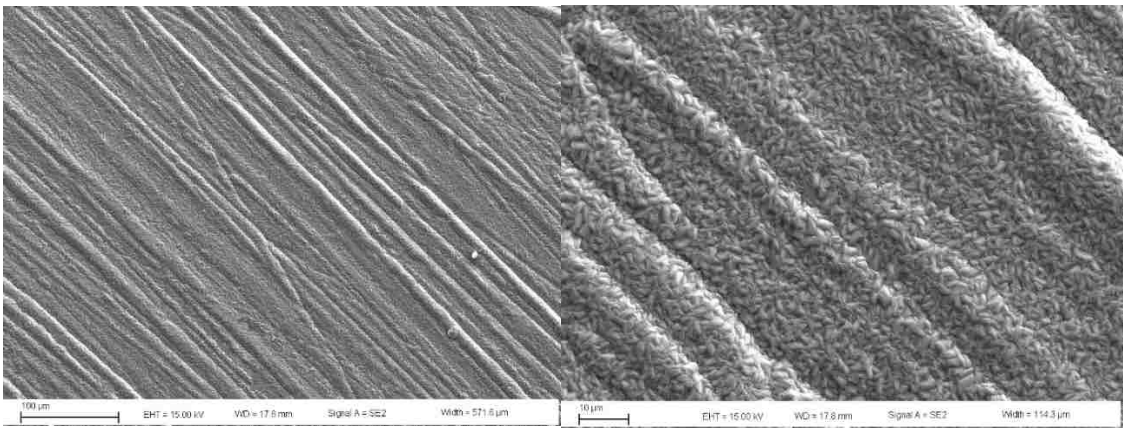

Figure 103: SEM of 3:2:1 Toluene:$AlCl_3$:BMImCl Electrolyte at -600 mV vs. Al QRE Deposition

At higher magnification and focusing on the edge there are evident edge effects from increased current density in this region, Figure 104.

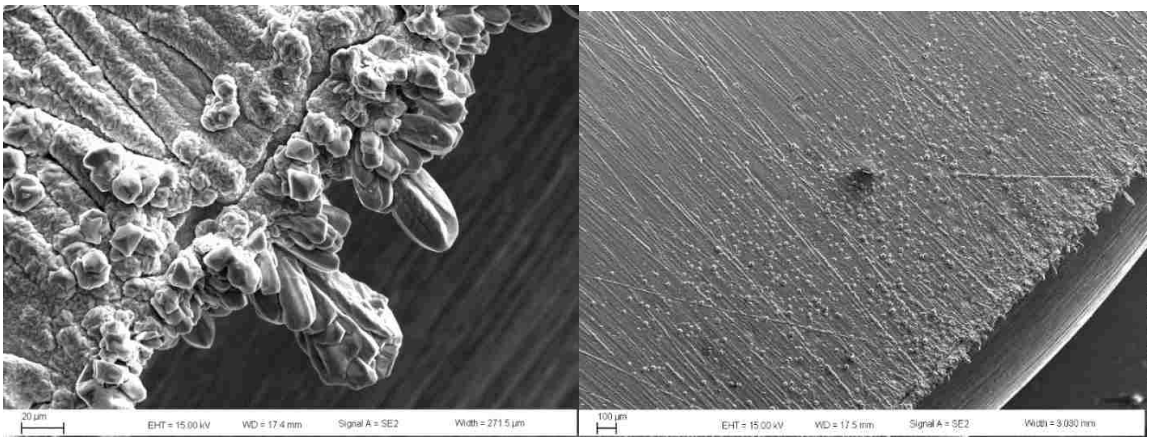

Figure 104: Edge Effects in Toluene Diluted Electrolytes

The edge of the film shows interesting nodule formation, possibly due to higher polarization in this region changing the deposition characteristics, but is very pure aluminum, as verified by the EDS shown in Figure 105.

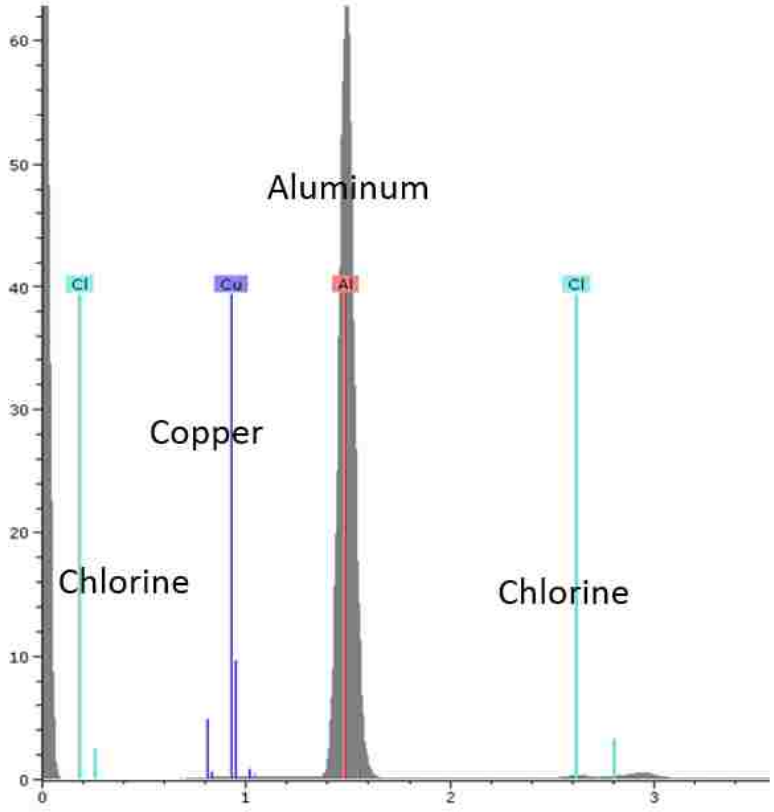

Figure 105: EDS of Aluminum Deposited in Toluene Diluted Systems at -600 mV vs. Al QRE

The EDS measurement in this film shows significant reduction in impurities and a nearly pure aluminum deposit. Moving to the maximum dilution solution of 6.8:2:1 Toluene:BMIC: $AlCl_3$ and depositing at -500mV decreases edge effects, either due to the slightly reduced overpotential or increased dilution, or both, which independently reduce the deposition rate (Figure 106).

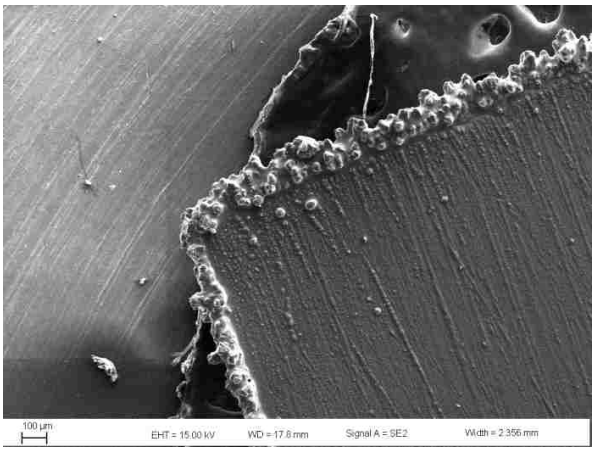

Figure 106: SEM of 6.8:2:1 Toluene:$AlCl_3$:BMImCl Electrolyte edge effects at -500 mV vs. Al QRE Deposition

These films are again very smooth but the plating rate is lower than the 3:2:1 system at -600 mV. The platelike growth is seen in as with the other depositions in this overpotential range, Figure 107.

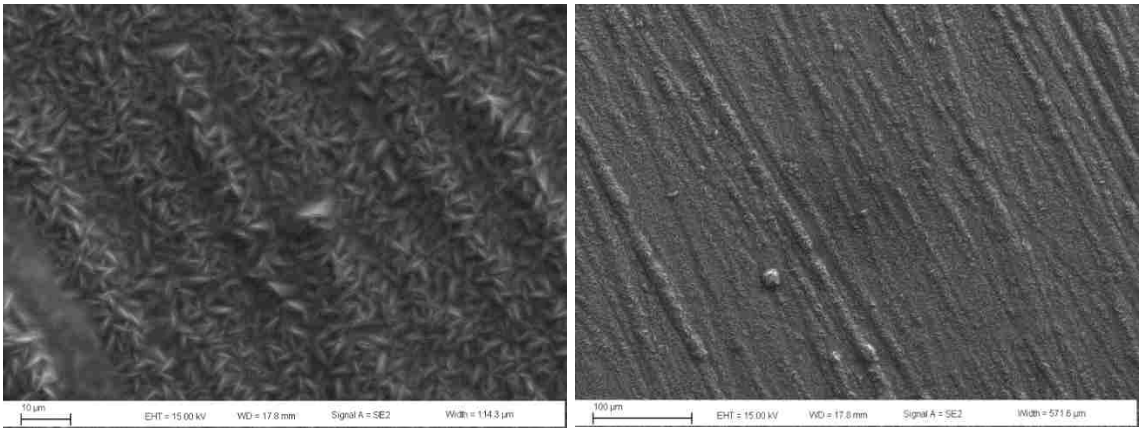

Figure 107: SEM of 6.8:2:1 Toluene:$AlCl_3$:BMImCl Electrolyte at -500 mV vs. Al QRE Deposition

EDS was also done on this sample, shown in Figure 108 .

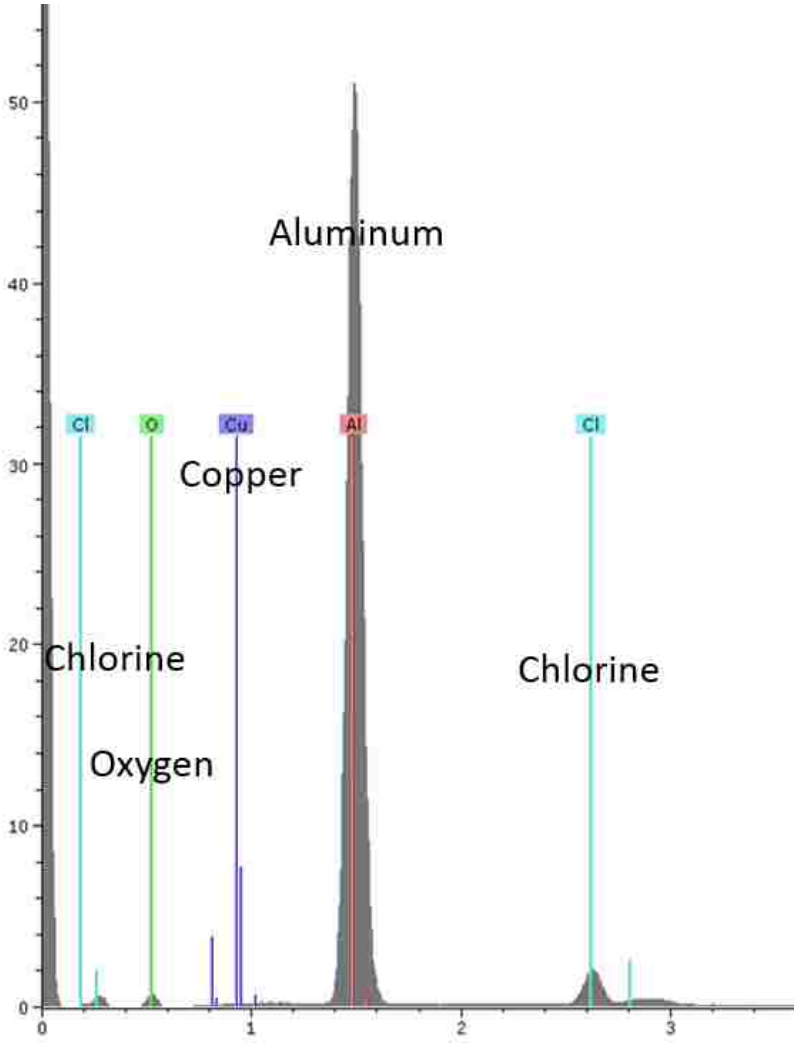

Figure 108: EDS of Aluminum Deposited in High Toluene Diluted Systems at -500 mV vs. Al QRE

Increasing the dilution to the maximum amount led to slightly more chlorine incorporation. Continuing to use the 6.8:2:1 Toluene:BMIC:$AlCl_3$ electrolyte but increasing the overpotential to -1000 mV shows a change in growth mode, leading to a much darker, grey and rough deposit, shown in Figure 109.

Figure 109: Aluminum Deposited on Cu in a 6.8:2:1 Toluene:$AlCl_3$:BMImCl Electrolyte at -1000 mV vs. Al QRE

The SEM images show more nodule formation as well as signs of electrolyte breakdown, .

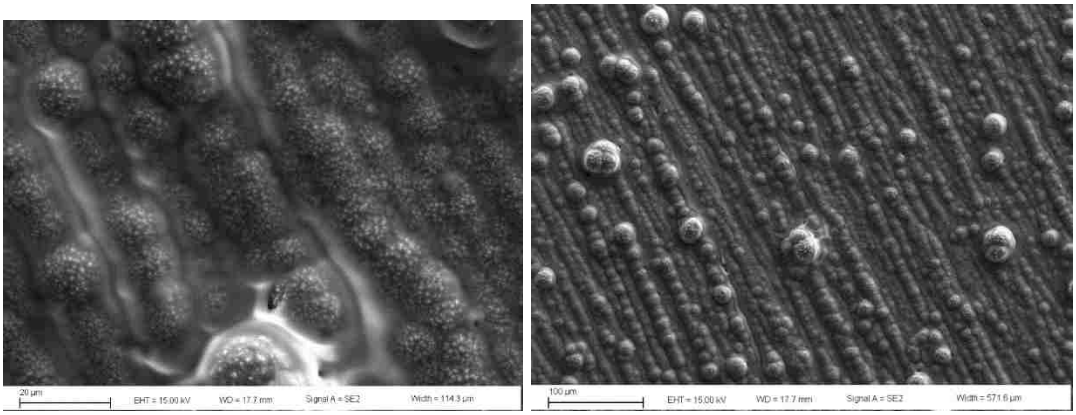

Figure 110: SEM of 6.8:2:1 Toluene:AlCl3:BMImCl Electrolyte at -1000 mV vs. Al QRE Deposition

The edge effects are more pronounced as the overpotential is increased, indicating the increased polarization and current are indeed influencing them. The module growth is also more pronounced, as seen in .

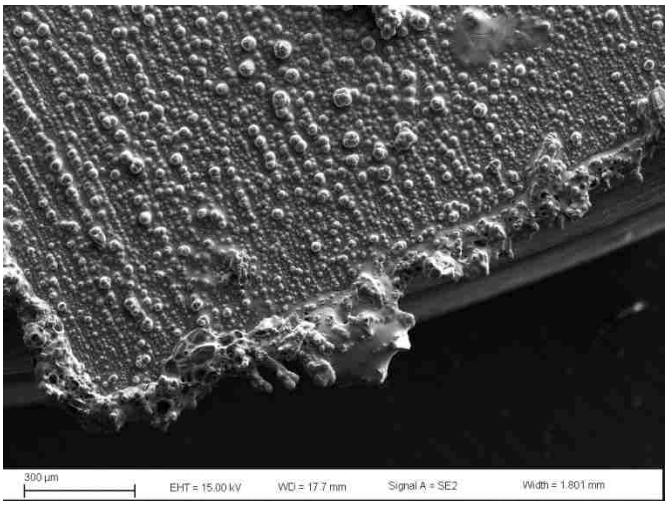

Figure 111: SEM of 6.8:2:1 Toluene:AlCl3:BMImCl Electrolyte edge effects at -1000 mV vs. Al QRE Deposition

Deposition at -1000 mV starts to incorporate more carbon and chlorine impurities, shown in .

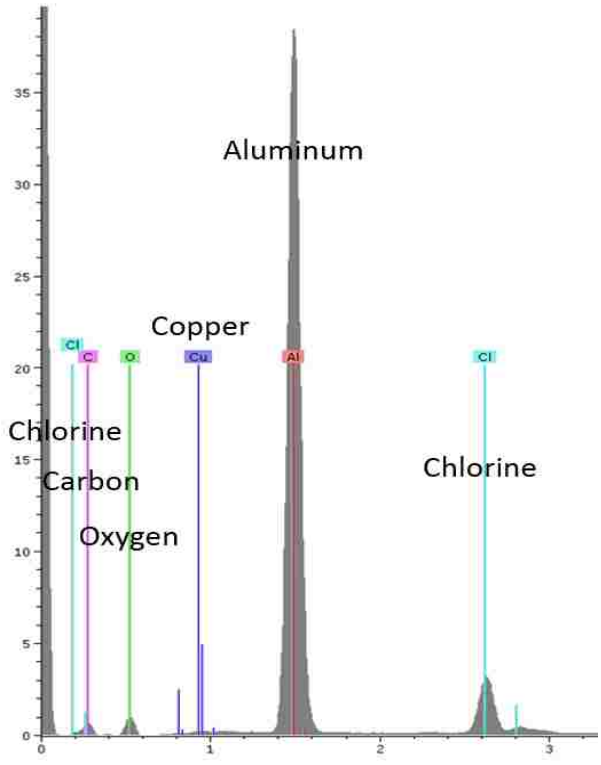

Figure 112: EDS of Aluminum Deposited in High Toluene Diluted Systems at -1000 mV vs. Al QRE

Further increasing the deposition overpotential of the 6.8:2:1 Toluene:BMIC: $AlCl_3$ electrolyte to -1500mV leads to poor morphology and severe electrolyte breackdown. The macroscopic quality is black and rough, shown in .

Figure 113: Aluminum Deposited on Cu in a 6.8:2:1 Toluene:AlCl3:BMImCl Electrolyte at -1500 mV vs. Al QRE

A very different growth is seen in the SEM images, shown in Figure 114.

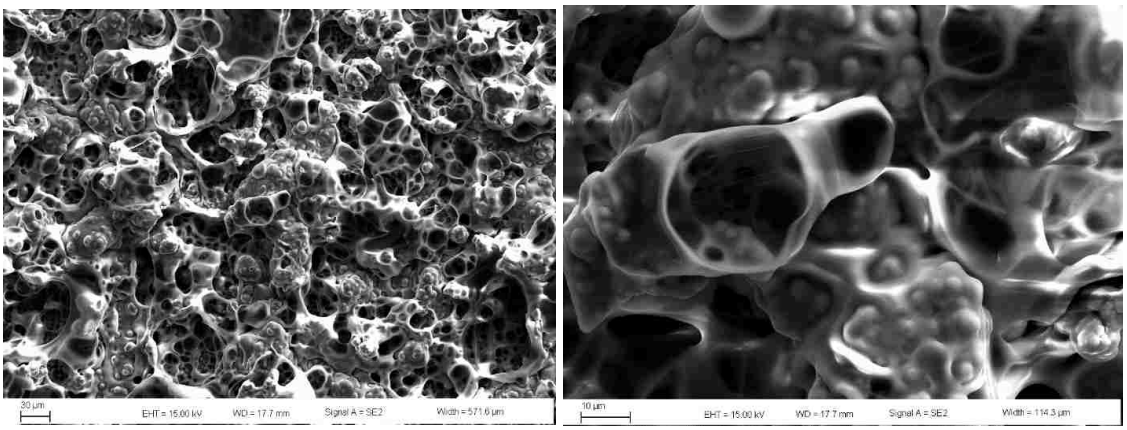

Figure 114: SEM of 6.8:2:1 Toluene:AlCl3:BMImCl Electrolyte at -1500 mV vs. Al QRE Deposition

This strange growth was investigated with EDS mapping, Figure 115.

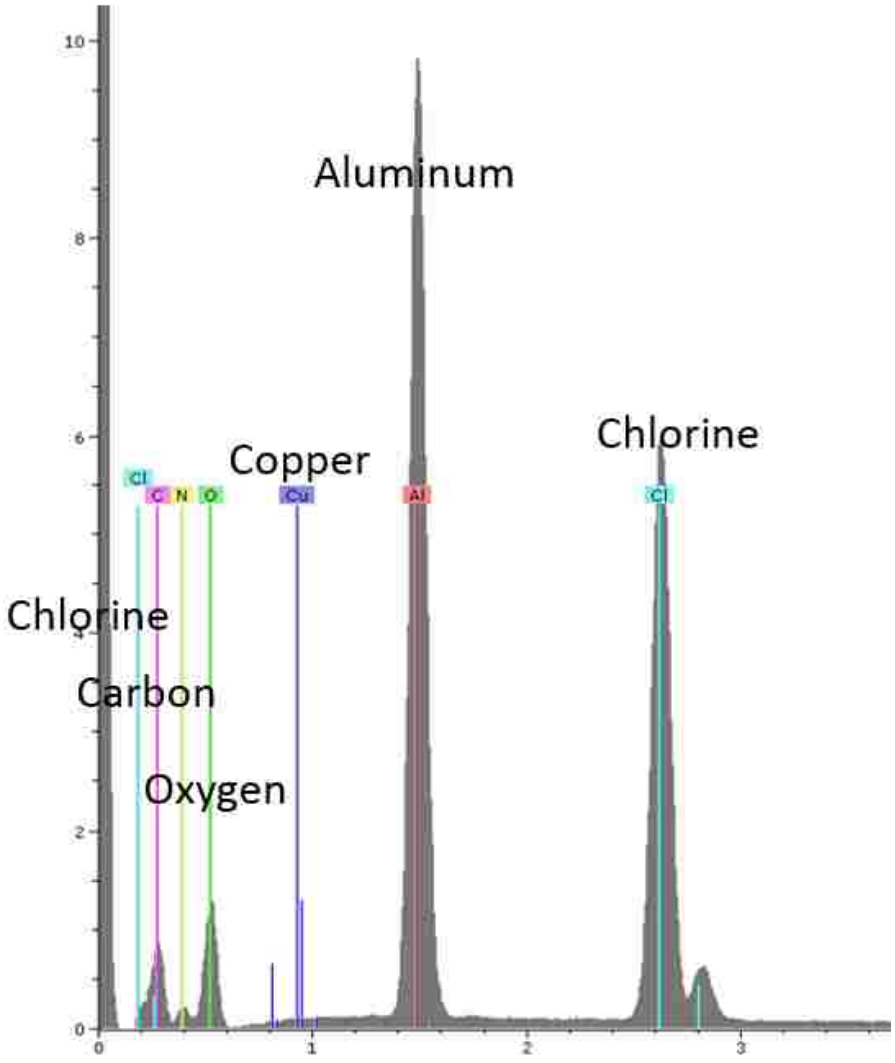

Figure 115: EDS of Aluminum Deposited in High Toluene Diluted Systems at -1500 mV vs. Al QRE

The EDS spectrum shown a lot of chlorine, carbon, nitrogen and oxygen impurities. The carbon, oxygen, and chlorine are localized in the surrounding film while the aluminum stays relatively pure and forms nodules in the open spaces, seen in Figure 116.

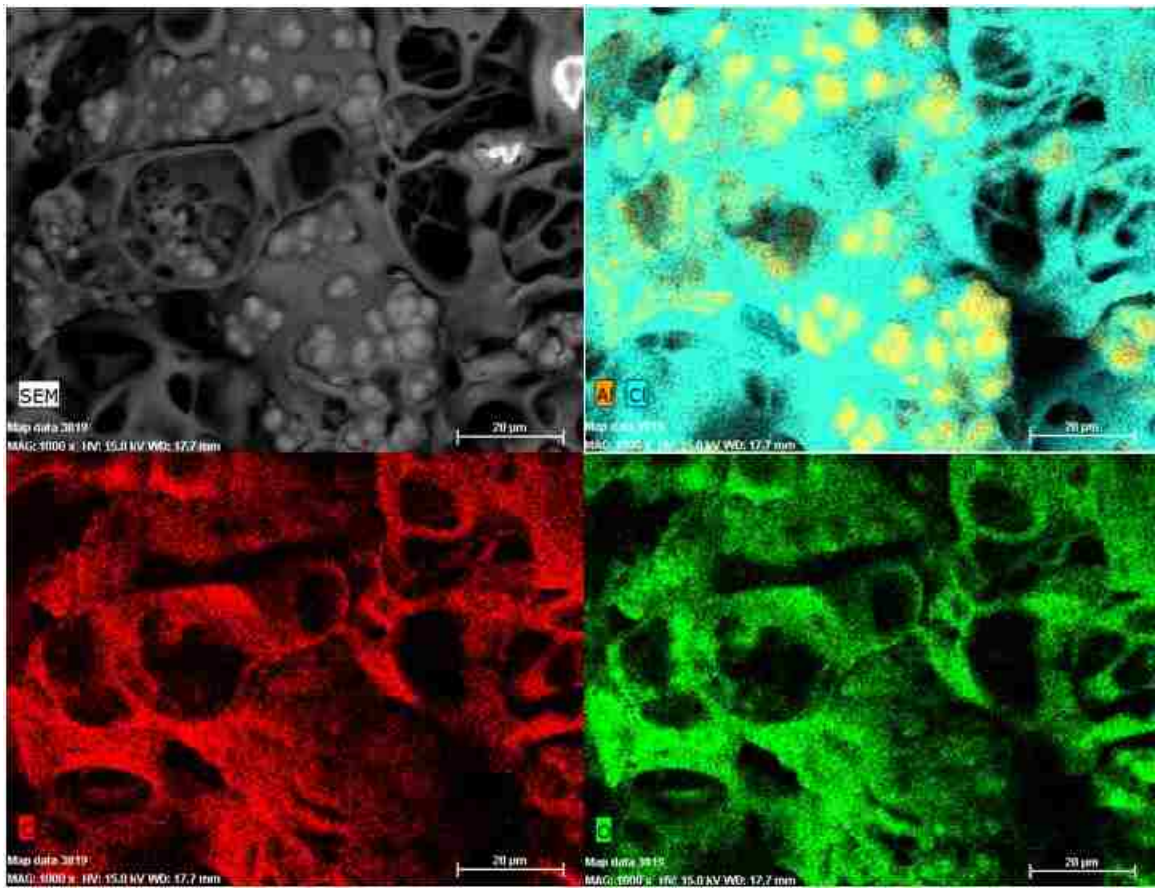

Figure 116: Mapped EDS of Aluminum Deposited in High Toluene Diluted Systems at -1500 mV vs. Al QRE

Moving to higher dilutions requires a more polar cosolvent and the DCB was tested at 11:2:1 oDCB:BMIC: $AlCl_3$ ratios. The film deposited at -600mV provides high quality coatings like the 3:2:1 toluene chemistry with a slight decrease in plating rate, Figure 117.

Figure 117: Aluminum Deposited on Cu in a 11:2:1 DCB:AlCl3:BMImCl Electrolyte at -600 mV vs. Al QRE

The SEM images show very minor surface roughness, Figure 118.

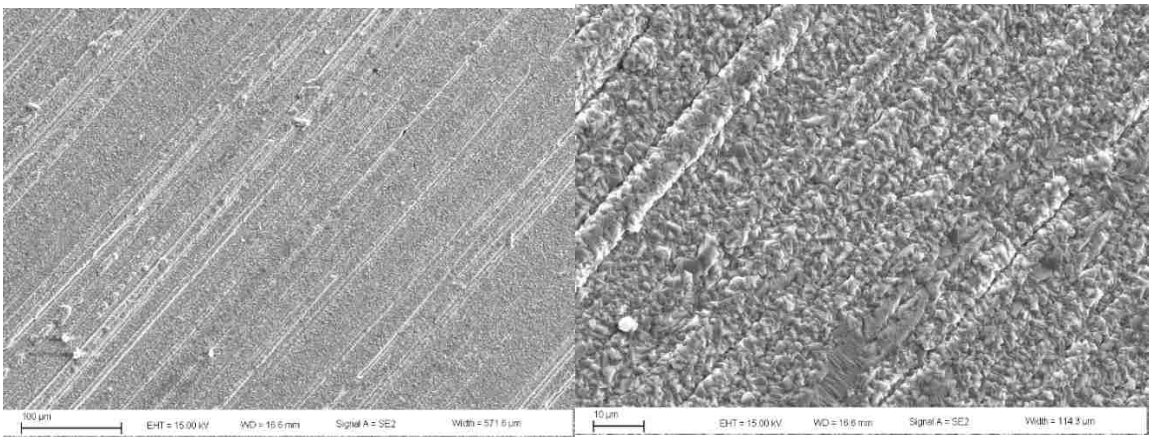

Figure 118: SEM of 11:2:1 DCB:AlCl3:BMImCl Electrolyte at -600 mV vs. Al QRE Deposition

DCB dilutions at this ratio decreases edge effects seen in other depositons, this is caused by plating rate reduction and higher permittivity. The edges of the deposits in these solutions are very consistent with the bulk deposition characteristics. Even further dilution to 16:2:1 DCB:BMIC: $AlCl_3$ and -600mV depositions result in severe decreases in deposition rate due to low concentrations of the reducing aluminum complex. The macroscopic quality is visably satisfactory, but the deposition rates are slower than the more concentrated chemistries, Figure 119.

Figure 119: Aluminum Deposited on Cu in a 16:2:1 DCB:AlCl3:BMImCl Electrolyte at -600 mV vs. Al QRE

At -600 mV in higher dilutions the deposit results in poor coverage after 30 minutes as seen in the SEM images, seen in Figure 120 . This is again due to the low concentration forcing low plating rates. If the concentration is to be use the low plating rates must be accounted for.

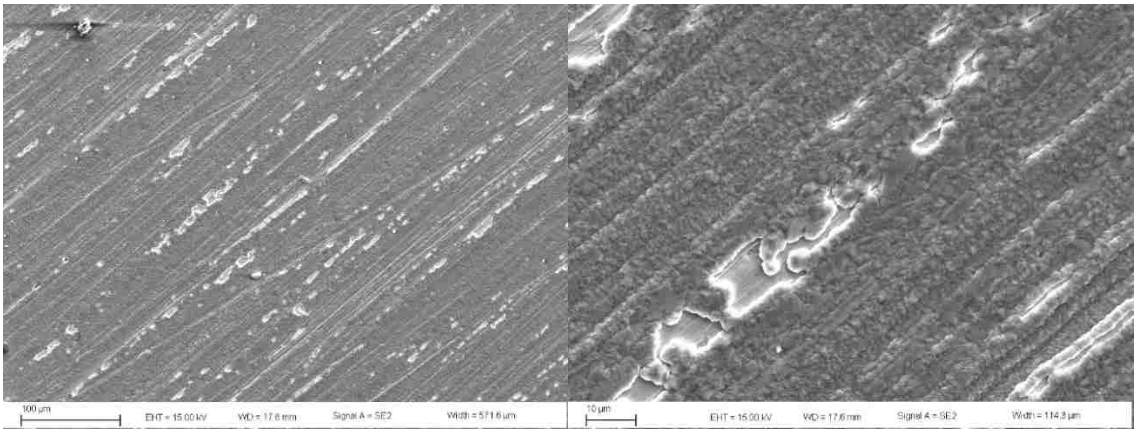

Figure 120: SEM of 16:2:1 DCB:AlCl3:BMImCl Electrolyte at -600 mV vs. Al QRE Deposition

EDS of the heavily diluted solutions show very pure aluminum with no sign of electrolyte breakdown, shown in Figure 121.

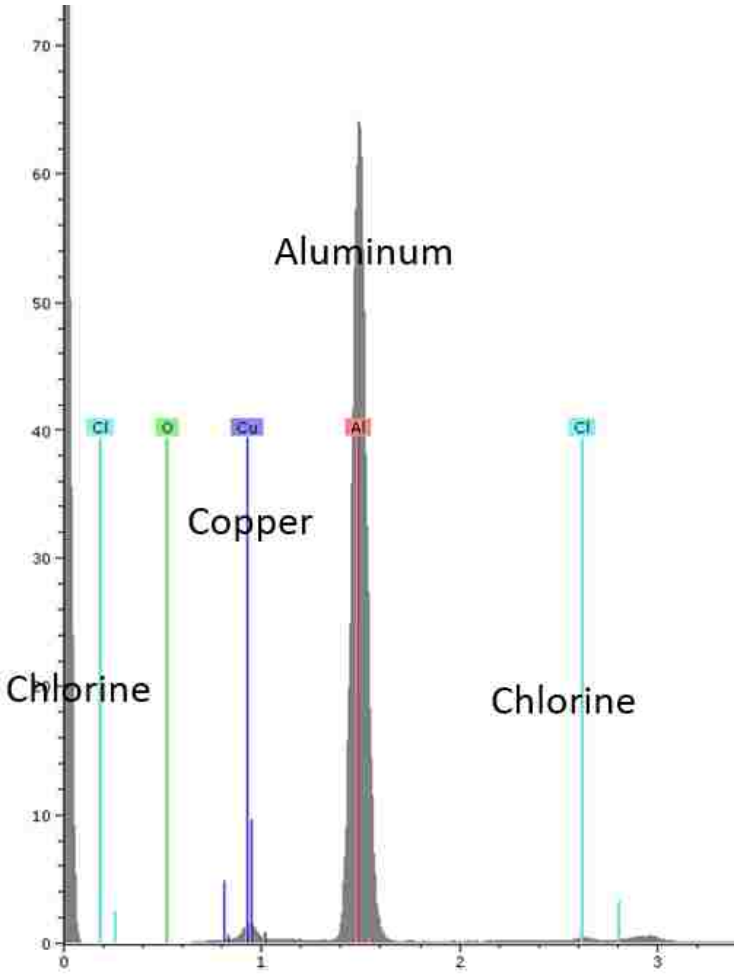

Figure 121: EDS of Aluminum Deposited in High DCB Diluted Systems at -600 mV vs. Al QRE

The deposit is still pure aluminum with no electrolyte breakdown or incorporation but the copper substrate is observed in the EDS spectrum due to incomplete surface coverage.

Appendix D: Viscosity Data

The viscosity is shear thinning and decreases significantly with temperature. The shear equation constants decrease with a logarithmic decay with temperature, and this best fit curve was used to interpolate data points at temperatures in between those measured. The viscosities calculated and used for Levich equations are shown in tables following the rheological data of each system (Figures 122 through 145).

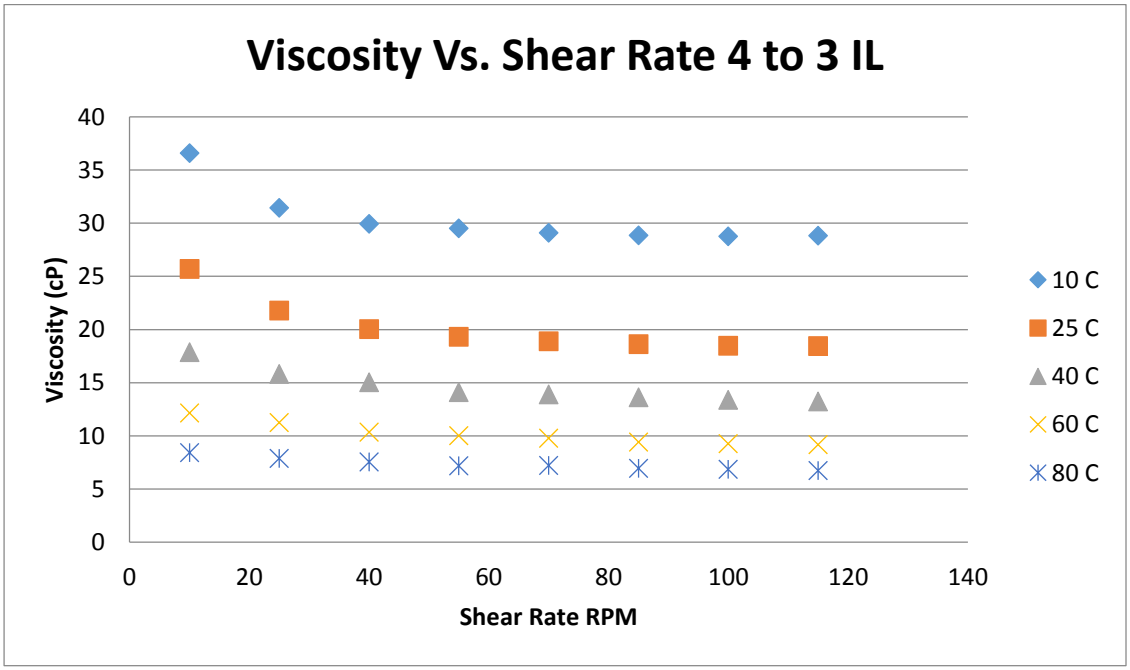

Figure 122: Viscosity vs. Shear Rate in 4 to 3 IL

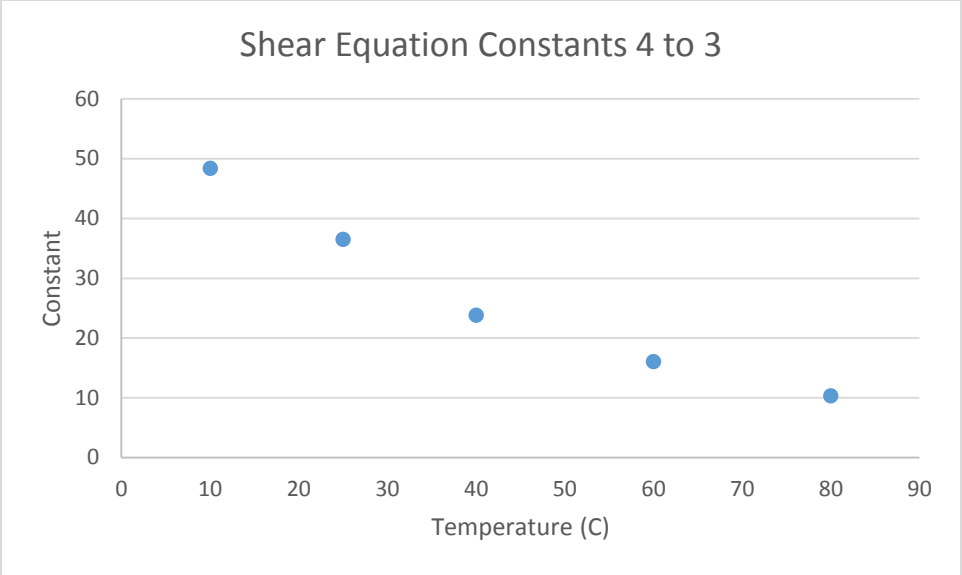

Figure 123: Shear Equation Constants in 4 to 3 IL

The shear thinning exponential shows a minimum in the intermediate temperature range of the values tested, although none of them vary significantly. Since they are fairly consistent, no analysis was done on why the trend exhibited a minimum.

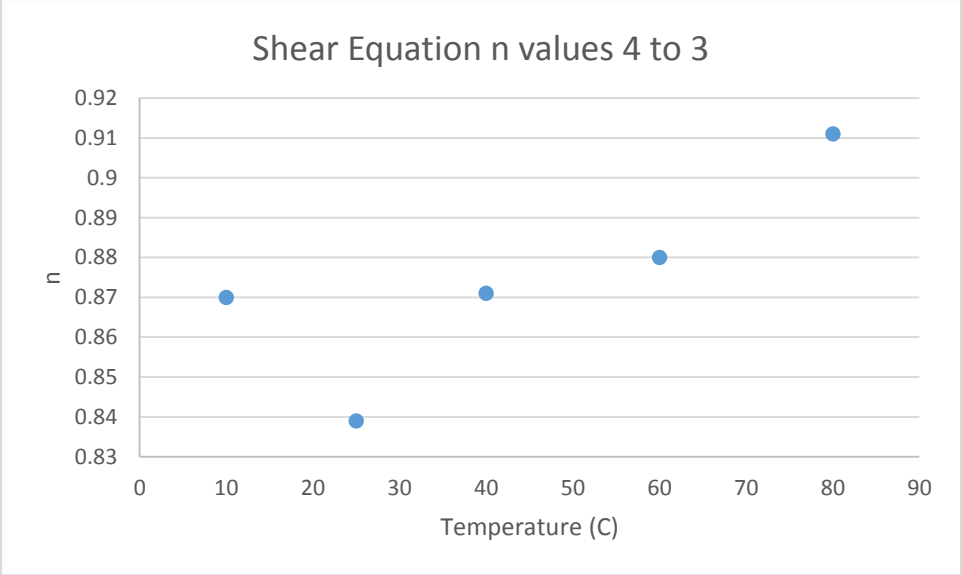

Figure 124: Shear Equation Power Law Values in 4 to 3 IL

The shear equation exponentials show a minimum, which appears in many of the electrolyte systems tested. In this case the minimum is at 25˚ C but other solutions show this minimum shifted to slightly higher temperatures. The values were used with direct interpolation to predict the values of temperatures in between the experimentally measured values, although there is little variation at any point.

4 to 3	Electrolyte	Viscosity (cP)		
		30˚ C	50˚ C	80˚ C
	50 RPM	27.07	18.31	9.70
	100 RPM	24.91	16.85	9.12
	500 RPM	20.54	13.89	7.90
	1000 RPM	18.90	12.78	7.43

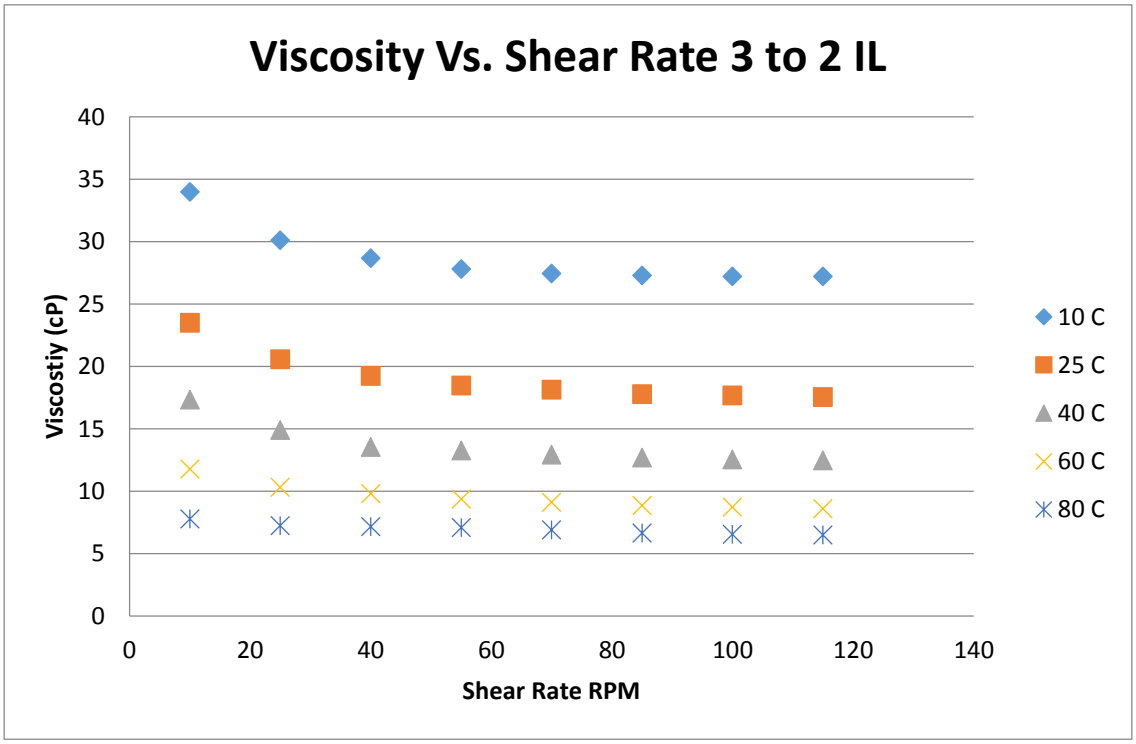

Figure 125: Viscosity vs. Shear Rate in 3 to 2 IL

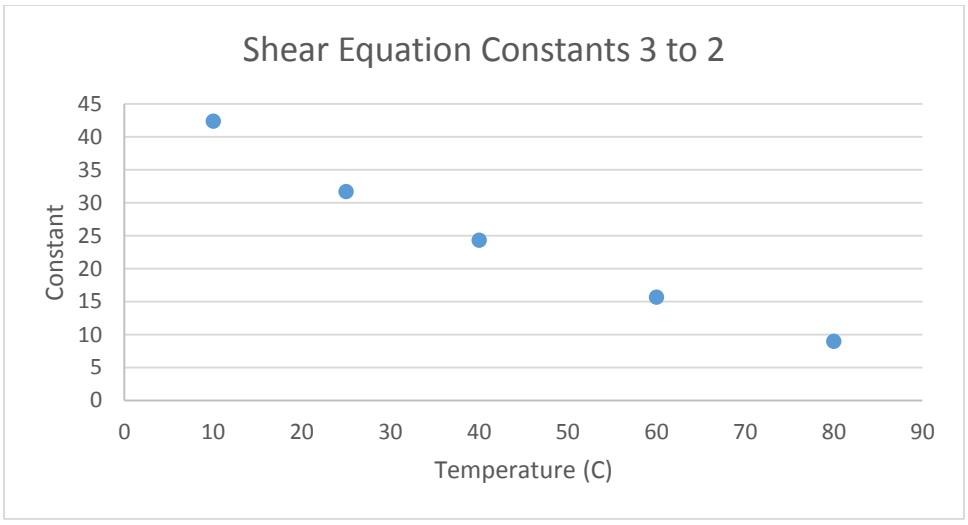

Figure 126: Shear Equation Constants in 3 to 2 IL

The shear equation shows a linear decrease in shear constants in the 3 to 2 chemistry, while it exhibits a minimum of n value at the 40˚ C condition.

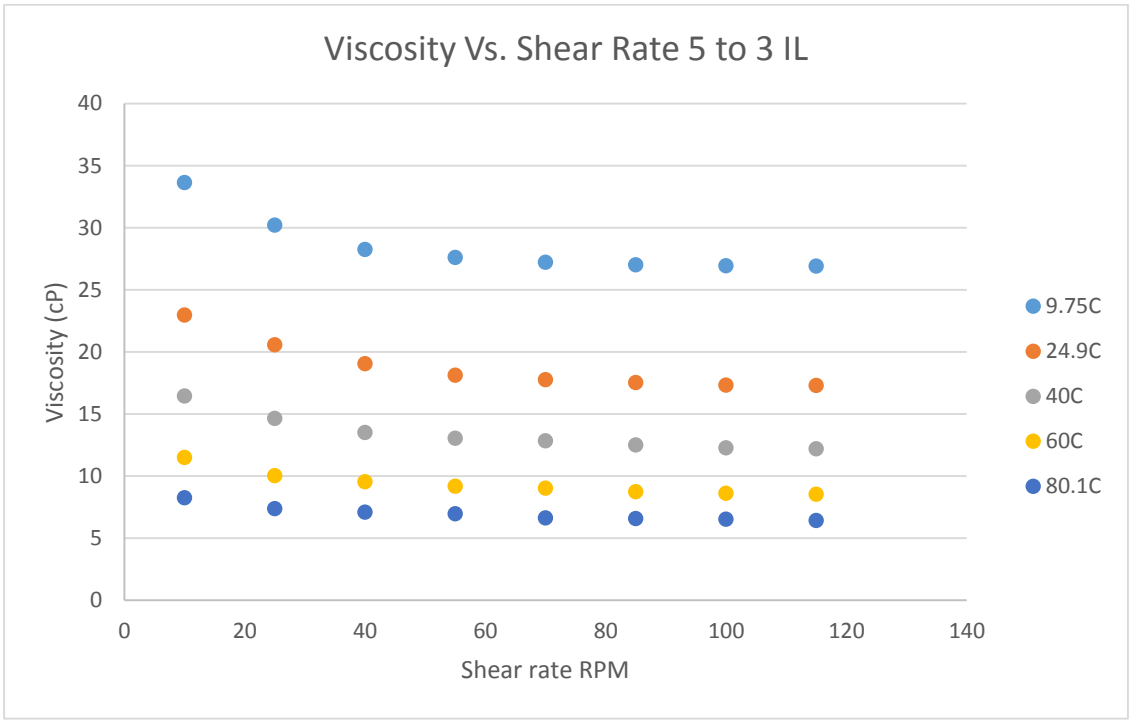

Figure 127: Viscosity vs. Shear Rate in 5 to 3 IL

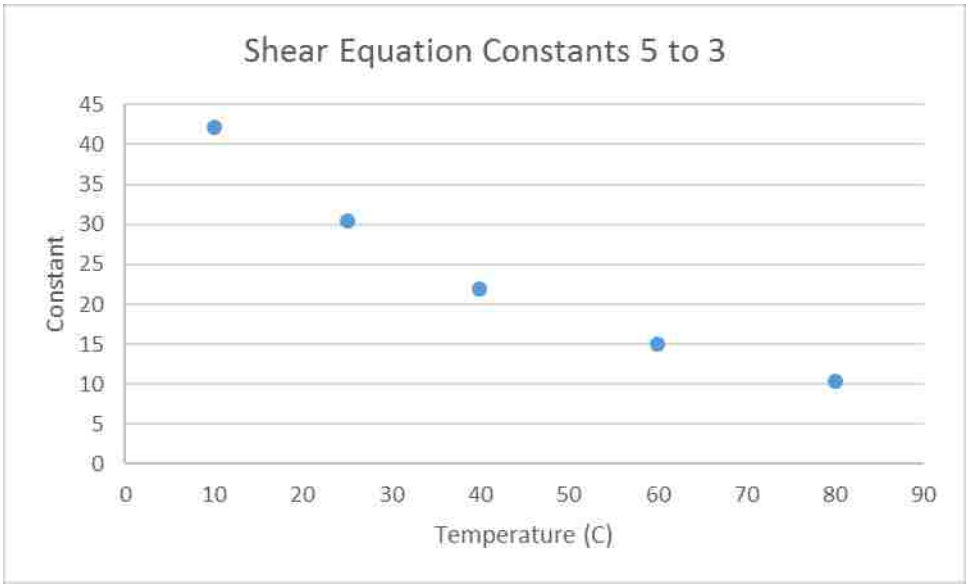

Figure 128: Shear Equation Constants in 5 to 3 IL

5 to 3 Electrolyte	Viscosity (cP)		
	30˚ C	50˚ C	80˚ C
50 RPM	25.41	17.73	10.20
100 RPM	23.39	16.31	9.59
500 RPM	19.28	13.45	8.31
1000 RPM	17.74	12.37	7.81

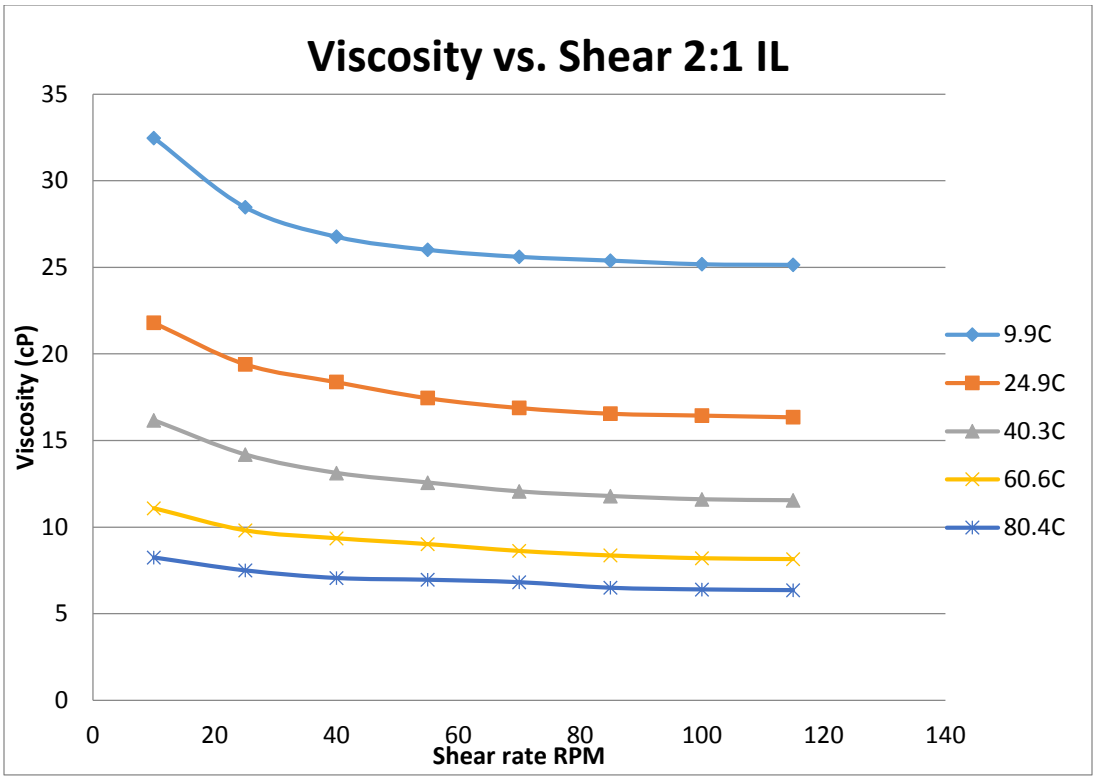

Figure 129: Viscosity vs. Shear Rate in 2 to 1 IL

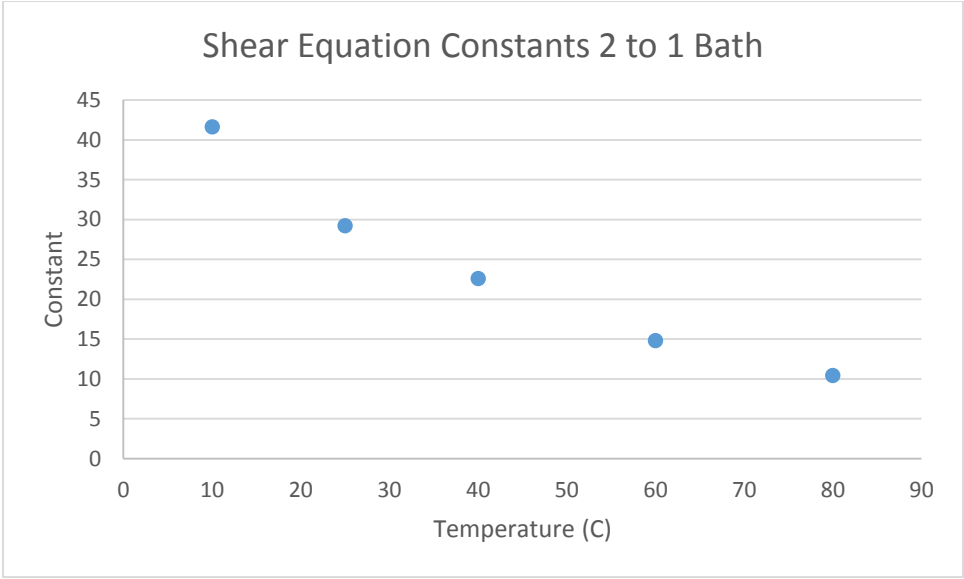

Figure 130: Shear Equation Constants in 2 to 1 IL

2 to 1 Electrolyte	Viscosity (cP)		
	30˚ C	50˚ C	80˚ C
50 RPM	24.85	17.36	10.18
100 RPM	22.86	15.97	9.47
500 RPM	18.85	13.17	8.00
1000 RPM	17.34	12.12	7.43

References

1. David Linden, T.B.R., *Handbook of Batteries*. Third Edition ed. 2001: McGraw-Hill.

2. Linden, D.R., Thomas B., *Handbook of Batteries*. 2002: McGraw-Hill Handbooks.

3. Reed, J.W., et al. *Burn-rate studies with iron/potassium perchlorate heat pellets*. in *Power Sources Symposium, 1992., IEEE 35th International*. 1992.

4. Zhang, K., et al., *Development of a nano-Al/CuO based energetic material on silicon substrate.* Applied Physics Letters, 2007. **91**(11).

5. Gavens, A.J., et al., *Effect of intermixing on self-propagating exothermic reactions in Al/Ni nanolaminate foils.* Journal of Applied Physics, 2000. **87**(3): p. 1255-1263.

6. Martirosyan, K.S. and S.E. Lyshevski, *MEMS Technology Microthrusters and Nanoenergetic Materials For Micropropulsion Systems.* 2012 2nd International Conference Methods and Systems of Navigation and Motion Control (Msnmc), 2012: p. 133-136.

7. Mann, A.B., et al., *Modeling and characterizing the propagation velocity of exothermic reactions in multilayer foils.* Journal of Applied Physics, 1997. **82**(3): p. 1178-1188.

8. Rossi, C., et al., *Nanoenergetic materials for MEMS: A review*. Journal of Microelectromechanical Systems, 2007. **16**(4): p. 919-931.

9. Simões, S., F. Viana, and M. Vieira, *Reactive Commercial Ni/Al Nanolayers for Joining Lightweight Alloys.* Journal of Materials Engineering and Performance, 2014. **23**(5): p. 1536-1543.

10. Duckham, A., et al., *Reactive nanostructured foil used as a heat source for joining titanium.* Journal of Applied Physics, 2004. **96**(4): p. 2336-2342.

11. Eakins, D. and N.N. Thadhani, *Shock-induced reaction in a flake nickel plus spherical aluminum powder mixture.* Journal of Applied Physics, 2006. **100**(11).

12. T. Acchione, J.H., *Measuring the Performance of Low- Melting Metallic Sputtering Targets Bonded at Room Temperature (Ambient).* SVC - 53rd Annual Technical Conference Proceedings. Society of Vacuum Coaters., 2010.

13. Henderson, A.L. and J. Gryko, *CHED 1166-Enthalpy of nickel-aluminum reaction.* Abstracts of Papers of the American Chemical Society, 2008. **235**.

14. Kovalev, O.B. and V.A. Neronov, *Metallochemical analysis of the reaction in a mixture of nickel and aluminum powders.* Combustion Explosion and Shock Waves, 2004. **40**(2): p. 172-179.

15. Morsi, K., *Review: reaction synthesis processing of Ni-Al intermetallic materials (vol A299, pg 1, 2000).* Materials Science and Engineering a-Structural Materials Properties Microstructure and Processing, 2001. **308**(1-2): p. 296-296.

16. Dreizin, E.L., *Metal-based reactive nanomaterials.* Progress in Energy and Combustion Science, 2009. **35**(2): p. 141-167.

17. Gunduz, I.E., et al., *Modeling of the self-propagating reactions of nickel and aluminum multilayered foils.* Journal of Applied Physics, 2009. **105**(7): p. 074903.

18. Milan Paunovic, M.S., *Fundamentals of Electrochemical Deposition*. 2nd ed. 2006: Wiley. 373.

19. Hovestad, A. and L.J.J. Janssen, *ELECTROCHEMICAL CODEPOSITION OF INERT PARTICLES IN A METALLIC MATRIX.* Journal of Applied Electrochemistry, 1995. **25**(6): p. 519-527.

20. Muller, B. and H. Ferkel, *Al2O3-nanoparticle distribution in plated nickel composite films.* Nanostructured Materials, 1998. **10**(8): p. 1285-1288.

21. Wang, S.C. and W.C.J. Wei, *Characterization of electroplated Ni/SiC and Ni/Al2O3 composite coatings bearing nanoparticles.* Journal of Materials Research, 2003. **18**(7): p. 1566-1574.

22. Lee, H.K., H.Y. Lee, and J.M. Jeon, *Codeposition of micro- and nano-sized SiC particles in the nickel matrix composite coatings obtained by electroplating.* Surface & Coatings Technology, 2007. **201**(8): p. 4711-4717.

23. Karbasi, M., N. Yazdian, and A. Vahidian, *Development of electro-co-deposited Ni-TiC nano-particle reinforced nanocomposite coatings.* Surface & Coatings Technology, 2012. **207**: p. 587-593.

24. Kuo, S.L., *Effect of nickel ion concentration on Ni/Al2O3 composite coatings.* Journal of the Chinese Institute of Engineers, 2005. **28**(1): p. 1-8.

25. Corni, I., et al., *Electro co-deposition of Ni-Al2O3 composite coatings.* Journal of Materials Science, 2012. **47**(14): p. 5361-5373.

26. Ger, M.D., *Electrochemical deposition of nickel/SiC composites in the presence of surfactants.* Materials Chemistry and Physics, 2004. **87**(1): p. 67-74.

27. Cui, X., et al., *Electrochemical study of codeposition of Al particle—Nanocrystalline Ni/Cu composite coatings.* Electrochimica Acta, 2008. **54**(2): p. 415-420.

28. Talbot, J.B., *Electrocodeposition of nanocomposite films.* Plating and Surface Finishing, 2004. **91**(10): p. 60-65.

29. Liu, H. and W. Chen, *Electrodeposited Ni–Al composite coatings with high Al content by sediment co-deposition.* Surface and Coatings Technology, 2005. **191**(2–3): p. 341-350.

30. Low, C.T.J., R.G.A. Wills, and F.C. Walsh, *Electrodeposition of composite coatings containing nanoparticles in a metal deposit.* Surface & Coatings Technology, 2006. **201**(1-2): p. 371-383.

31. Gyftou, P., et al., *Electrodeposition of Ni/SiC composites by pulse electrolysis.* Transactions of the Institute of Metal Finishing, 2002. **80**: p. 88-91.

32. Singh, V.B. and P. Pandey, *Electrodeposition of nickel composites from water-diethanolamine bath.* Surface & Coatings Technology, 2006. **200**(14-15): p. 4511-4514.

33. Arghavanian, R. and N.P. Ahmadi, *Electrodeposition of Ni-ZrO2 composite coatings and evaluation of particle distribution and corrosion resistance.* Surface Engineering, 2011. **27**(9): p. 649-654.

34. Zheng, H.Y. and M.Z. An, *Electrodeposition of Zn-Ni-Al2O3 nanocomposite coatings under ultrasound conditions.* Journal of Alloys and Compounds, 2008. **459**(1-2): p. 548-552.

35. Webb, P.R. and N.L. Robertson, *ELECTROLYTIC CODEPOSITION OF NI-GAMMA-AL2O3 THIN-FILMS.* Journal of the Electrochemical Society, 1994. **141**(3): p. 669-673.

36. Pavlatou, E.A., et al., *Hardening effect induced by incorporation of SiC particles in nickel electrodeposits.* Journal of Applied Electrochemistry, 2006. **36**(4): p. 385-394.

37. Thiemig, D. and A. Bund, *Influence of ethanol on the electrocodeposition of Ni/Al2O3 nanocomposite films.* Applied Surface Science, 2009. **255**(7): p. 4164-4170.

38. Thiemig, D., A. Bund, and J.B. Talbot, *Influence of hydrodynamics and pulse plating parameters on the electrocodeposition of nickel-alumina nanocomposite films.* Electrochimica Acta, 2009. **54**(9): p. 2491-2498.

39. Tuaweri, T.J. and G.D. Wilcox, *Influence of SiO2 particles on zinc-nickel electrodeposition.* Transactions of the Institute of Metal Finishing, 2007. **85**(5): p. 245-253.

40. Lee, D., et al., *Influence of ultrasonic irradiation on the microstructure of Cu/Al2O3, CeO2 nanocomposite thin films during electrocodeposition.* Materials Science and Engineering a-Structural Materials Properties Microstructure and Processing, 2007. **447**(1-2): p. 209-216.

41. Shao, I., et al., *Kinetics of particle codeposition of nanocomposites.* Journal of the Electrochemical Society, 2002. **149**(11): p. C610-C614.

42. Asadi, A., et al., *New procedure for electrochemical production of Ni-TiC composite powder.* Powder Metallurgy, 2010. **53**(1): p. 47-50.

43. Shrestha, N.K. and T. Saji, *Non-aqueous composite plating of Ni-ceramic particles using ethanol bath and anti-wear performance of the coatings.* Surface & Coatings Technology, 2004. **186**(3): p. 444-449.

44. Feng, Q.Y., T.J. Li, and J.Z. Jin, *Research on the mechanism of composite electroplating and its latest progress.* Rare Metal Materials and Engineering, 2007. **36**(3): p. 559-564.

45. Yang, X., X. Peng, and F. Wang, *Size effect of Al particles on the structure and oxidation of Ni/Ni3Al composites transformed from electrodeposited Ni–Al films.* Scripta Materialia, 2007. **56**(6): p. 509-512.

46. Kim, J.S., et al., *STUDY ON NANO-OXIDE POWDER DISPERSED Ni-ELECTROPLATED COMPOSITES FOR COMPONENTS MATERIALS OF NPPs*. Icone 17: Proceedings of the 17th International Conference on Nuclear Engineering, Vol 1. 2009, New York: Amer Soc Mechanical Engineers. 687-692.

47. Shao, I., et al., *Synthesis and characterization of particle-reinforced Ni/Al2O3 nanoconiposites.* Journal of Materials Research, 2002. **17**(6): p. 1412-1418.

48. Sen, R., S. Das, and K. Das, *Synthesis and Properties of Pulse Electrodeposited Ni-CeO2 Nanocomposite.* Metallurgical and Materials Transactions a-Physical Metallurgy and Materials Science, 2012. **43A**(10): p. 3809-3823.

49. Narasimman, P., M. Pushpavanam, and V.M. Periasamy, *Synthesis, characterization and comparison of sediment electro-codeposited nickel-micro and nano SiC composites.* Applied Surface Science, 2011. **258**(1): p. 590-598.

50. Narasimman, P., M. Pushpavanam, and V.M. Periasamy, *Wear and scratch resistance characteristics of electrodeposited nickel-nano and micro SiC composites.* Wear, 2012. **292**: p. 197-206.

51. Musiani, M., *Electrodeposition of composites: arm expanding subject in electrochemical materials science.* Electrochimica Acta, 2000. **45**(20): p. 3397-3402.

52. Plieth, W., *Electrochemistry for Materials Science*. 2008: Elsevier. 410.

53. Dong, S.S., et al., *Synthesis of intermetallic NiAl by SHS reaction using coarse-grained nickel and ultrafine-grained aluminum produced by wire electrical explosion.* Intermetallics, 2002. **10**(3): p. 217-223.

54. Liu, H.F. and W.X. Chen, *Electrodeposited Ni-Al composite coatings with high Al content by sediment co-deposition.* Surface & Coatings Technology, 2005. **191**(2-3): p. 341-350.

55. John Duffy, A.H. *Suspension stability: Why particle size, zeta potential and rheology are important*. 2011 [cited 2016.

56. Ian Rose, C.W., *Nickel Plating Handbook*. 2013.

57. Haarberg, M.G.-E.G.M., *Molten Salts Chemistry and Technology*. 2014: Wiley.

58. VanderNoot*, Y.Z.a.T.J., *Review: Electrodeposition of aluminium from nonaqueous organic electrolytic systems and room temperature molten salts.* Electrochimica Acre,, 1997. **42**(1): p. 3-13.

59. Garai, T., *ELECTRODEPOSITION OF ALUMINUM IN NON-AQUEOUS SOLVENTS.* Materials Chemistry and Physics, 1983. **8**(5): p. 399-434.

60. Galova, M. and D. Kladekova, *Basic Parameters of the Electrode Process of Aluminum Deposition from Tetrahydrofuran Solutions .1. Exchange Current-Density.* Surface Technology, 1980. **11**(5): p. 371-376.

61. Eckert, J. and M. Galova, *Electrode-Kinetics of the Aluminum Deposition from Tetrahydrofuran Electrolytes.* Electrochimica Acta, 1981. **26**(8): p. 1169-1175.

62. Galova, M., D. Kladekova, and L. Lux, *Basic Parameters of the Electrode Process in Aluminum Deposition from Tetrahydrofuran Solutions .2. Mechanism of the Electrode-Reaction.* Surface Technology, 1981. **13**(4): p. 315-324.

63. Howarth, J.N. and D. Pletcher, *The Study of Aluminum Deposition from Tetrahydrofuran Solutions of Alcl3-Lialh4 Using Microelectrodes .2. The Influence of Solution Composition.* Journal of the Chemical Society-Faraday Transactions I, 1987. **83**: p. 2795-2802.

64. Howarth, J.N. and D. Pletcher, *The Study of Aluminum Deposition from Tetrahydrofuran Solutions of Alcl3-Lialh4 Using Microelectrodes .1. 1-1 Alcl3-Lialh4.* Journal of the Chemical Society-Faraday Transactions I, 1987. **83**: p. 2787-2794.

65. Biallozor, S., V. Mazin, and M. Lieder, *The Electrodeposition of Aluminum from Xylene and Ether-Hydride Electrolytes.* Journal of Applied Electrochemistry, 1993. **23**(3): p. 253-256.

66. Simanavicius, L., et al., *Electrodeposition of Aluminum from Xylene and Toluene Electrolytes by Pulsed Current.* Protection of Metals, 1995. **31**(5): p. 467-470.

67. Shavkunov, S.P. and T.L. Strugova, *Electrode processes during aluminum electrodeposition in aromatic solvents.* Russian Journal of Electrochemistry, 2003. **39**(6): p. 642-649.

68. Legrand, L., A. Tranchant, and R. Messina, *Behavior of Aluminum as Anode in Dimethylsulfone-Based Electrolytes.* Electrochimica Acta, 1994. **39**(10): p. 1427-1431.

69. Legrand, L., et al., *Raman study of aluminum chloride dimethylsulfone solutions.* Inorganic Chemistry, 1996. **35**(5): p. 1310-1312.

70. Jiang, T., et al., *Studies on the AlCl3/dimethylsulfone (DMSO2) electrolytes for the aluminum deposition processes.* Surface & Coatings Technology, 2007. **201**(14): p. 6309-6317.

71. Matsui, I., et al., *Fabrication of bulk nanocrystalline Al electrodeposited from a dimethylsulfone bath.* Materials Science and Engineering a-Structural Materials Properties Microstructure and Processing, 2012. **550**: p. 363-366.

72. Legrand, L., et al., *RDE and impedance study of anodic dissolution of aluminium in organic AlCl3/dimethylsulfone electrolytes.* Electrochimica Acta, 1998. **43**(21-22): p. 3109-3115.

73. Hirato, T., J. Fransaer, and J.P. Celis, *Electrolytic codeposition of silica particles with aluminum from AlCl3-dimethylsulfone electrolytes.* Journal of the Electrochemical Society, 2001. **148**(4): p. C280-C283.

74. Fransaer, J., et al., *Aluminium composite coatings containing micrometre and nanometre-sized particles electroplated from a non-aqueous electrolyte.* Journal of Applied Electrochemistry, 2002. **32**(2): p. 123-128.

75. Stewart, G. and C.L. Hussey, *Electrodeposition of transition metal aluminum alloys from molten AlCl3-NaCl.* Proceedings of the Eleventh International Symposium on Molten Salts Xi, 1998. **98**(11): p. 21-33.

76. Jafarian, M., et al., *Electrodeposition of aluminum from molten AlCl3-NaCl-KCl mixture.* Journal of Applied Electrochemistry, 2006. **36**(10): p. 1169-1173.

77. Okoturo, O.O. and T.J. VanderNoot, *Temperature dependence of viscosity for room temperature ionic liquids.* Journal of Electroanalytical Chemistry, 2004. **568**(0): p. 167-181.

78. Freemantle, M., *An Introduction to Ionic Liquids*. 2010: RSC Publishing.

79. Ohno, H., *Electrochemical Aspects of Ionic Liquids*. 2011: Wiley.

80. Hayyan, M., et al., *Investigating the electrochemical windows of ionic liquids.* Journal of Industrial and Engineering Chemistry, 2013. **19**(1): p. 106-112.

81. Franzen, G., et al., *THE ANIONIC STRUCTURE OF ROOM-TEMPERATURE ORGANIC CHLOROALUMINATE MELTS FROM SECONDARY ION MASS-SPECTROMETRY*. Organic Mass Spectrometry, 1986. **21**(7): p. 443-444.

82. Karpinski, Z.J. and R.A. Osteryoung, *DETERMINATION OF EQUILIBRIUM-CONSTANTS FOR THE TETRACHLOROALUMINATE ION DISSOCIATION IN AMBIENT-TEMPERATURE IONIC LIQUIDS.* Inorganic Chemistry, 1984. **23**(10): p. 1491-1494.

83. Heerman, L. and W. Dolieslager, *POTENTIOMETRIC STUDY OF THE SOLVENT EQUILIBRIA IN ALCL3-N-N-BUTYLPYRIDINIUM CHLORIDE MELTS.* Inorganic Chemistry, 1985. **24**(26): p. 4704-4707.

84. Chryssoulakis, Y., J.C. Poignet, and G. Manoli, *ELECTROCHEMICAL STUDY OF ALUMINUM ION REDUCTION IN ACIDIC ALCL3-NORMAL-BUTYL-PYRIDINIUM CHLORIDE MELTS.* Journal of Applied Electrochemistry, 1987. **17**(4): p. 857-867.

85. Moy, R. and F.P. Emmenegger, *Cosolvents for Chloroaluminate Electrolytes.* Electrochimica Acta, 1992. **37**(6): p. 1061-1068.

86. Jiang, T., et al., *Electrodeposition of aluminium from ionic liquids: Part II - studies on the electrodeposition of aluminum from aluminum chloride (AICl(3)) - trimethylphenylammonium chloride (TMPAC) ionic liquids.* Surface & Coatings Technology, 2006. **201**(1-2): p. 10-18.

87. Abbott, A.P., et al., *Double layer, diluent and anode effects upon the electrodeposition of aluminium from chloroaluminate based ionic liquids.* Physical Chemistry Chemical Physics, 2010. **12**(8): p. 1862-1872.

88. Liao, Q. and C.L. Hussey, *Densities, viscosities, and conductivities of mixtures of benzene with the Lewis acidic aluminum chloride plus 1-methyl-3-ethylimidazolium chloride molten salt.* Journal of Chemical and Engineering Data, 1996. **41**(5): p. 1126-1130.

89. Pitner, W.R., C.L. Hussey, and G.R. Stafford, *Electrodeposition of Nickel-Aluminum Alloys from the Aluminum Chloride-1-methyl-3-ethylimidazolium Chloride Room Temperature Molten Salt.* Journal of The Electrochemical Society, 1996. **143**(1): p. 130-138.

90. Pitner, W.R., C.L. Hussey, and G.R. Stafford, *Electrodeposition of nickel-aluminum alloys from the aluminum chloride-1-methyl-3-ethylimidazolium chloride room temperature molten salt.* Journal of the Electrochemical Society, 1996. **143**(1): p. 130-138.

91. Trulove, P.C., et al., *Electrodeposition and pitting corrosion of aluminum-manganese alloys from room temperature chloroaluminate molten salts.* Molten Salts Xii, Proceedings, 2000. **99**(41): p. 517-526.

92. Zhu, Q. and C.L. Hussey, *Electrodeposition of silver-aluminum alloys from room-temperature chloroaluminate molten salts.* Molten Salts Xii, Proceedings, 2000. **99**(41): p. 494-504.

93. Jiang, T., et al., *Electrodeposition of aluminium from ionic liquids: Part I - electrodeposition and surface morphology of aluminium from aluminium chloride (AlCl3)-l-ethyl-3-methylimidazolium chloride ([EMIm]Cl) ionic liquids.* Surface & Coatings Technology, 2006. **201**(1-2): p. 1-9.

94. Chang, J.K., et al., *Electrodeposition of aluminum on magnesium alloy in aluminum chloride (AlCl(3))-1-ethyl-3-methylimidazolium chloride (EMIC) ionic liquid and its corrosion behavior.* Electrochemistry Communications, 2007. **9**(7): p. 1602-1606.

95. Chang, J.K., et al., *Electrodeposition of Al on Magnesium Alloy from Aluminum Chloride/1-ethyl-3-methylimidazolium Chloride Ionic Liquids.* Electrochemistry, 2009. **77**(8): p. 585-587.

96. Yue, G.K., et al., *A Promising Method for Electrodeposition of Aluminium on Stainless Steel in Ionic Liquid.* Aiche Journal, 2009. **55**(3): p. 783-796.

97. Liu, Q.X., S.Z. El Abedin, and F. Endres, *Electrodeposition of nanocrystalline aluminum: Breakdown of imidazolium cations modifies the crystal size.* Journal of the Electrochemical Society, 2008. **155**(5): p. D357-D362.

98. El Abedin, S.Z., et al., *Electrodeposition of nanocrystalline aluminium from a chloroaluminate ionic liquid.* Electrochemistry Communications, 2010. **12**(8): p. 1084-1086.

99. Zhang, L.P., et al., *Electrodeposition of aluminum on magnesium from ionic liquid (EMIM)Br-AlCl3.* Transactions of Nonferrous Metals Society of China, 2010. **20**: p. S245-S248.

100. Tang, J.W. and K. Azumi, *Optimization of pulsed electrodeposition of aluminum from AlCl3-1-ethyl-3-methylimidazolium chloride ionic liquid.* Electrochimica Acta, 2011. **56**(3): p. 1130-1137.

101. Giridhar, P., S.Z. El Abedin, and F. Endres, *Electrodeposition of aluminium from 1-butyl-1-methylpyrrolidinium chloride/AlCl3 and mixtures with 1-ethyl-3-methylimidazolium chloride/AlCl3.* Electrochimica Acta, 2012. **70**: p. 210-214.

102. Pradhan, D. and R.G. Reddy, *Dendrite-Free Aluminum Electrodeposition from AlCl3-1-Ethyl-3-Methyl-Imidazolium Chloride Ionic Liquid Electrolytes.* Metallurgical and Materials Transactions B-Process Metallurgy and Materials Processing Science, 2012. **43**(3): p. 519-531.

103. Vaughan, J. and D. Dreisinger, *Electrodeposition of aluminum from aluminum chloride-trihexyl(tetradecyl) phosphonium chloride.* Journal of the Electrochemical Society, 2008. **155**(1): p. D68-D72.

104. Fitchett, B.D., T.N. Knepp, and J.C. Conboy, *1-Alkyl-3-methylimidazolium bis(perfluoroalkylsulfonyl)imide water-immiscible ionic liquids - The effect of water on electrochemical and physical properties.* Journal of the Electrochemical Society, 2004. **151**(7): p. E219-E225.

105. Burrell, A.K., et al., *The large scale synthesis of pure imidazolium and pyrrolidinium ionic liquids.* Green Chemistry, 2007. **9**(5): p. 449-454.

106. Welton, P.W.T., *Ionic Liquids in Synthesis*. 2nd ed. 2008: Wiley.

107. Yokota, Y., T. Harada, and K.I. Fukui, *Direct observation of layered structures at ionic liquid/solid interfaces by using frequency-modulation atomic force microscopy.* Chemical Communications, 2010. **46**(45): p. 8627-8629.

108. Abbott, A.P., et al., *Double layer effects on metal nucleation in deep eutectic solvents.* Physical Chemistry Chemical Physics, 2011. **13**(21): p. 10224-10231.

109. Kirchner, K., et al., *Electrical double layer in ionic liquids: Structural transitions from multilayer to monolayer structure at the interface.* Electrochimica Acta, 2013. **110**: p. 762-771.

110. Merlet, C., et al., *Computer simulations of ionic liquids at electrochemical interfaces.* Physical Chemistry Chemical Physics, 2013. **15**(38): p. 15781-15792.

111. Uysal, A., et al., *Structural Origins of Potential Dependent Hysteresis at the Electrified Graphene/Ionic Liquid Interface.* Journal of Physical Chemistry C, 2014. **118**(1): p. 569-574.

112. Ivanistsev, V., et al., *Restructuring of the electrical double layer in ionic liquids upon charging.* Journal of Physics-Condensed Matter, 2015. **27**(10).

113. Abbott, A.P., G. Capper, and S. Gray, *Design of Improved Deep Eutectic Solvents Using Hole Theory.* ChemPhysChem, 2006. **7**(4): p. 803-806.

114. Alhaji, A., *Electrodeposition of Alloys from Deep Eutectic Solvents*. 2012.

115. Tokuda, H., et al., *Physicochemical properties and structures of room temperature ionic liquids. 1. Variation of anionic species.* Journal of Physical Chemistry B, 2004. **108**(42): p. 16593-16600.

116. Tokuda, H., et al., *Physicochemical properties and structures of room temperature ionic liquids. 2. Variation of alkyl chain length in imidazolium cation.* Journal of Physical Chemistry B, 2005. **109**(13): p. 6103-6110.

117. Tokuda, H., et al., *Physicochemical properties and structures of room-temperature ionic liquids. 3. Variation of cationic structures 10.1021/jpO53396f.* Journal of Physical Chemistry B, 2006. **110**(6): p. 2833-2839.

118. Tokuda, H. and M. Watanabe, *Ionicity of room temperature ionic liquids: A parameter controlling the physicochemical properties.* Abstracts of Papers of the American Chemical Society, 2006. **231**.

119. Watanabe, M. and H. Tokuda, *PHYS 53-How ionic are ionic liquids? An indicator of the physicochemical properties.* Abstracts of Papers of the American Chemical Society, 2006. **232**.

120. Moschovi, A.M., V. Dracopoulos, and V. Nikolakis, *Inter- and Intramolecular Interactions in Imidazolium Protic Ionic Liquids.* The Journal of Physical Chemistry B, 2014. **118**(29): p. 8673-8683.

121. Ueno, K., H. Tokuda, and M. Watanabe, *Ionicity in ionic liquids: correlation with ionic structure and physicochemical properties.* Physical Chemistry Chemical Physics, 2010. **12**(8): p. 1649-1658.

122. Fredlake, C.P., et al., *Thermophysical properties of imidazolium-based ionic liquids.* Journal of Chemical and Engineering Data, 2004. **49**(4): p. 954-964.

123. Tsuzuki, S., et al., *Magnitude and directionality of interaction in ion pairs of ionic liquids: Relationship with ionic conductivity.* Journal of Physical Chemistry B, 2005. **109**(34): p. 16474-16481.

124. Spohr, H.V. and G.N. Patey, *Structural and dynamical properties of ionic liquids: The influence of ion size disparity.* Journal of Chemical Physics, 2008. **129**(6).

125. Spohr, H.V. and G.N. Patey, *Structural and dynamical properties of ionic liquids: The influence of charge location.* Journal of Chemical Physics, 2009. **130**(10).

126. Spohr, H.V. and G.N. Patey, *Structural and dynamical properties of ionic liquids: Competing influences of molecular properties.* Journal of Chemical Physics, 2010. **132**(15).

127. Kulkarni, P.S., et al., *Comparison of physicochemical properties of new ionic liquids based on imidazolium, quaternary ammonium, and guanidinium cations.* Chemistry-a European Journal, 2007. **13**(30): p. 8478-8488.

128. Burrell, G.L., N.F. Dunlop, and F. Separovic, *Non-Newtonian viscous shear thinning in ionic liquids.* Soft Matter, 2010. **6**(9): p. 2080-2086.

129. Yu, G.R., et al., *Viscosity of ionic liquids: Database, observation, and quantitative structure-property relationship analysis.* Aiche Journal, 2012. **58**(9): p. 2885-2899.

130. Pogodina, N.V., et al., *Molecular dynamics of ionic liquids as probed by rheology*. Journal of Rheology, 2011. **55**(2): p. 241-256.

131. Noda, A., K. Hayamizu, and M. Watanabe, *Pulsed-Gradient Spin−Echo 1H and 19F NMR Ionic Diffusion Coefficient, Viscosity, and Ionic Conductivity of Non-Chloroaluminate Room-Temperature Ionic Liquids.* The Journal of Physical Chemistry B, 2001. **105**(20): p. 4603-4610.

132. Zhang, M., V. Kamavarum, and R.G. Reddy, *New electrolytes for aluminum production: Ionic liquids.* JOM, 2003. **55**(11): p. 54-57.

133. Jiang, T., et al., *Studies on the AlCl3/dimethylsulfone (DMSO2) electrolytes for the aluminum deposition processes.* Surface and Coatings Technology, 2007. **201**(14): p. 6309-6317.

134. Zhao, Y.G. and T.J. VanderNoot, *Electrodeposition of aluminium from nonaqueous organic electrolytic systems and room temperature molten salts.* Electrochimica Acta, 1997. **42**(1): p. 3-13.

135. Okoturo, O.O. and T.J. VanderNoot, *Temperature dependence of viscosity for room temperature ionic liquids.* Journal of Electroanalytical Chemistry, 2004. **568**(1-2): p. 167-181.

136. Pradhan, D. and R.G. Reddy, *Mechanistic study of Al electrodeposition from EMIC–AlCl3 and BMIC–AlCl3 electrolytes at low temperature.* Materials Chemistry and Physics, 2014. **143**(2): p. 564-569.